

**NONLINEAR ULTRAFAST-LASER SPECTROSCOPY OF GAS-PHASE
SPECIES AND TEMPERATURE IN HIGH-PRESSURE REACTING
FLOWS**

by

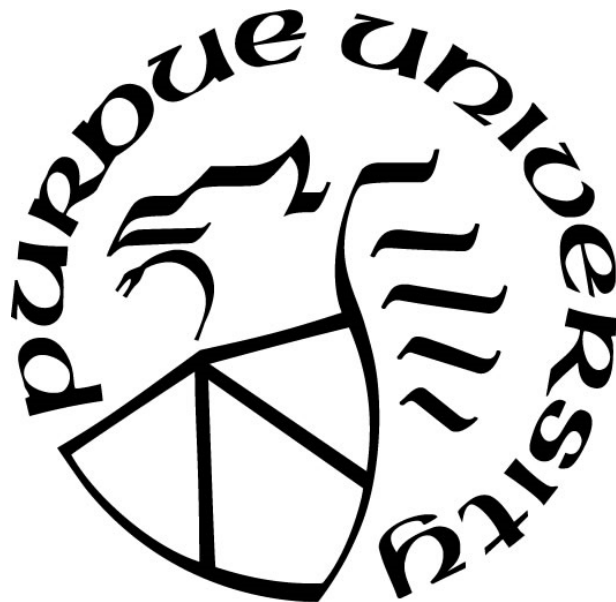
Kazi Arafat Rahman

A Dissertation

Submitted to the Faculty of Purdue University

In Partial Fulfillment of the Requirements for the degree of

Doctor of Philosophy



School of Mechanical Engineering

West Lafayette, Indiana

December 2019

THE PURDUE UNIVERSITY GRADUATE SCHOOL
STATEMENT OF COMMITTEE APPROVAL

Dr. Terrence R. Meyer, Co-Chair

School of Mechanical Engineering

Dr. Mikhail N. Slipchenko, Co-Chair

School of Mechanical Engineering

Dr. Steven F. Son

School of Mechanical Engineering

Dr. Timothée L. Pourpoint

School of Aeronautics and Astronautics

Approved by:

Dr. Nicole L. Key

My wife Shahereen – for being the symphony of my life
My daughter Zwena – you are the most precious gift of my life
My mom Selina – for being the best mother and a great human being

ACKNOWLEDGMENTS

It has been a great journey to start in a lab with two empty rooms and on the verge of finishing, leaving twenty-five graduate students pursuing their dreams across the entire Maurice J. Zucrow laboratory. I am so grateful for the opportunity to work with some of the great minds in the field of laser-diagnostics. Special gratitude goes to my co-supervisor Dr. Terrence Meyer for his untiring patience, unheard-of work ethics and out-of-the-box thinking, that helped shape my cognitive skills to be a more competent researcher. Over the last four years, even during the most stressed moments, I have never seen Dr. Meyer to be even a little annoyed on any of his graduate students—which had baffled me sometimes (because we really deserved to be yelled at sometimes!). Regardless of the time in the day and definitely anytime at night, he was available to talk, discuss and further extend those crazy ideas.

My other co-supervisor Dr. Mikhail Slipchenko is probably the reason I continued pursuing my PhD research works after the very stressful initial few months—being alienated in a new country and a lab with no labmates. He shaped a person who started without any experience on optics to someone who loves lasers and its interaction with matter. Dr. Slipchenko's hands on guidance helped me grow a passion for lasers. Moreover, he is also the source of one of the unsolved problems that I have encountered during my time here in Purdue. Numerous times, experiments and electronic devices that were dead for days—started working normally—just by his sheer presence in the lab!

I would also like to extend my gratitude to Dr. Steven Son and Dr. Timothée Pourpoint for their valuable time while serving as the committee members. Additionally, I am grateful to have the chance to work with Dr. Suresh Roy, Dr. Hans Stauffer, Dr. Yue Wu, Dr. Zhili Zhang, Dr. Alexey Shashurin, and Dr. Chloe Dedic. Each of them has spent time discussing challenging questions and generating new ideas toward my research objectives.

I have had the chance to work with so many intelligent and bright people in the Zucrow lab including Alber Douglawi, Mike Smyser, Venkat Athmanathan, Animesh Sharma, Daniel Lauriola, Naveed Rahman, Karna Patel, Erik Braun, and Jordan Fisher. At some point of my research work, each of them contributed to accomplish my goals. Particularly, I want to point out countless hours I have spent discussing on numerous topics with Mike Smyser, and Venkat Athmanathan (the plumbing god!) and being the nicest person and having the “always-ready-to-help” attitude.

TABLE OF CONTENTS

LIST OF TABLES.....	8
LIST OF FIGURES	9
LIST OF ABBREVIATIONS.....	13
ABSTRACT.....	14
1. INTRODUCTION	15
1.1 Ultrafast Laser Characteristics.....	16
1.1.1 Intensity and phase in time- and frequency-domain.....	16
1.1.2 Time-Bandwidth Product (TBP).....	18
1.2 Two-Photon Laser Induced Fluorescence (TP-LIF)	20
1.3 Coherent Anti-Stokes Raman Scattering	21
1.4 Hybrid fs/ps CARS Model.....	26
1.4.1 Third-order molecular response function	29
Raman transition strength.....	30
Raman cross-sections	31
Collisional dephasing rates and Raman linewidths.....	32
1.4.2 Hybrid fs/ps CARS model implementation and data fitting procedure.....	34
Generation of temperature and pressure dependent spectral library	34
Experimental data fitting procedure	37
1.5 Dissertation Summary.....	37
2. FEMTOSECOND, TWO-PHOTON, LASER-INDUCED FLUORESCENCE (TP-LIF)	
MEASUREMENT OF CO IN HIGH-PRESSURE FLAMES	39
2.1 Introduction.....	39
2.2 Experimental Apparatus and Conditions	41
2.3 Results and Discussion	43
2.3.1 Effects of excitation wavelength and energy.....	43
2.3.2 TP-LIF images of the flame profile at high pressure.....	45
2.3.3 Effects of flame luminosity and detection system.....	46
2.3.4 Potential sources of de-excitation at elevated pressure	47
2.3.5 Quantitative CO TP-LIF measurement at different pressures	50

2.4	Conclusions.....	50
3.	PRESSURE-SCALING CHARACTERISTICS OF FEMTOSECOND, TWO- PHOTON LASER-INDUCED FLUORESCENCE OF CARBON MONOXIDE	53
3.1	Motivation.....	53
3.2	Experimental Setup.....	55
3.3	Results and Discussion	57
3.3.1	Irradiance limitation at the window.....	57
3.3.2	Pressure scaling of CO fs TP-LIF.....	58
3.3.3	Effects of quenching.....	58
3.3.4	Forward lasing	60
3.3.5	Absorption of the excitation laser beam	61
3.3.6	Photoionization	62
3.3.7	Interference-minimized pressure scaling.....	65
3.4	Conclusions.....	67
4.	QUANTITATIVE FEMTOSECOND, TWO-PHOTON LASER-INDUCED FLUORESCENCE OF ATOMIC OXYGEN IN HIGH-PRESSURE FLAMES.....	69
4.1	Introduction.....	69
4.2	Experimental Apparatus.....	71
4.3	Results and Discussion	73
4.3.1	Effects of excitation wavelength	73
4.3.2	Dependence of o fs TP-LIF signal on laser irradiance	74
4.3.3	Interferences from O ₂	75
4.3.4	Quantitative O-atom fs TP-LIF measurement	76
4.3.5	O fs TP-LIF images at high pressure.....	78
4.3.6	Pressure scaling of O fs TP-LIF signal.....	79
4.4	Conclusions.....	81
5.	HYBRID fs/ps VIBRATIONAL CARS THERMOMETRY IN HIGH-PRESSURE FLAMES	82
5.1	Introduction.....	82
5.2	Experimental set-up for hybrid fs/ps VCARS	83
5.3	Considerations for CARS data fitting.....	84

5.4	Limits of collisional independence	87
5.5	Temperature accuracy and precision	87
5.6	Conclusion	91
6.	FLEXIBLE CHIRP-FREE PROBE PULSE AMPLIFICATION FOR kHz fs-ps ROTATIONAL COHERENT ANTI-STOKES RAMAN SCATTERING.....	92
6.1	Motivation.....	92
6.2	Design of the ps-probe amplifier	92
6.3	Amplifier output pulse characteristics	93
6.4	Two-beam rotational CARS at flame temperature	98
6.5	Summary	100
7.	CONCLUSIONS AND FUTURE WORK.....	101
7.1	Summary	101
7.2	Directions for future work	104
	APPENDIX A. MOLECULAR CONSTANTS AND FITTING PARAMETERS FOR N ₂ CARS MODEL	106
	REFERENCES	107
	PUBLICATIONS.....	122

LIST OF TABLES

Table 1.1 Time-Bandwidth Products for TL pulse shapes.	20
Table 1.2 Excitation and detection wavelengths for two-photon transitions of different species.	22
Table 1.3 Raman selection rules.	30
Table 1.4 Generation of temperature and pressure dependent spectral library for hybrid fs/ps vibrational and rotational CARS.....	35

LIST OF FIGURES

Figure 1.1 Qualitative representation of time-domain characteristics of a 30-fs Gaussian pulse with (a) $\phi(t) = 0$. (b) Second-order phase, $\phi_2 = -0.092 \text{ rad fs}^2$	19
Figure 1.2 Wave-mixing energy level diagram. Frequency-domain diagram: (a) Vibrational CARS; (b) Rotational CARS; (c) Time-domain picture depicting the relative position of different pulses for hybrid fs/ps CARS. Dashed line represents virtual energy state.....	27
Figure 2.1 Experimental setup of the fs laser, imaging, and spectrally resolved detection system for CO fs TP-LIF.	42
Figure 2.2 (a) CO TP-LIF signal dependence on the laser excitation wavelength at 1 and 5 atm showing experimental data (symbols) with a Gaussian fit (line) and (b) CO TP-LIF signal dependence on the excitation laser energy at 1 and 5 atm. $10 \mu\text{J/pulse}$ corresponds to an irradiance of $\sim 1.7 \times 10^{10} \text{ W/cm}^2$. Error bars represent $\pm\sigma$	44
Figure 2.3 Averaged (upper row) and single-shot (lower row) CO fs TP-LIF signals at 1, 4, 8, 12 atm (left to right). Camera: ICCD (PI-Max4-SB). The main flow exit of the Hencken burner was $25 \times 25 \text{ mm}$. Laser sheet was approximately 8 mm above the burner surface.	45
Figure 2.4 CO TP-LIF and flame background signals using an intensifier (IRO) and CMOS camera combination versus an ICCD camera with a shorter time gate for 1–5 atm CH_4 -air Hencken burner flames at $\phi = 1.3$	47
Figure 2.5 (a) CO fs TP-LIF emission spectra measured in a $\phi = 1.3 \text{ CH}_4$ -air flame. Laser irradiance was $2.3 \times 10^{10} \text{ W/cm}^2$ ($13 \mu\text{J/pulse}$). Both the 1 and 5 atm spectra were normalized by the peak signal at 1 atm near 483 nm. (b) Simplified energy level diagram indicating the (0-0) and (1-1) transitions in the $B^1\Sigma^+ \leftarrow X^1\Sigma^+$ system excited at 230.1 nm in this work.	49
Figure 2.6 Comparison of CO mole fractions from equilibrium theory and experimental CO fs TP-LIF signals at various equivalence ratios for pressures of (a) 1 atm and (b) 5 atm. ICCD gate width is 15 ns. Error bars represent $\pm\sigma$	51
Figure 2.7 Theoretical quenching rates as a function of equivalence ratio assuming equilibrium concentrations of quenching species for the products of CH_4 -air combustion.	51
Figure 3.1 a) Simplified energy level diagram for CO fs TP-LIF showing the excitation at 230.1 nm. The dashed line represents the ionization potential, b) schematic diagram of the experimental set-up for CO fs TP-LIF in a mixing chamber.....	56
Figure 3.2 Trends showing the effects of multiphoton absorption and degradation of the UV excitation beam for different window transmission configurations.	57
Figure 3.3 CO fs TP-LIF signal as a function of pressure in (a) $\Phi = 1.3 \text{ CH}_4$ -Air flame stabilized in a Hencken burner. (b) mixtures of CO and N_2 . Laser irradiance was $\sim 1.7 \times 10^{10} \text{ W/cm}^2$ measured at 1 atm. Error bar represents $\pm\sigma$	59
Figure 3.4 CO fs TP-LIF signal as a function of pressure in a mixing chamber for CO with different collision partners at a laser irradiance of $\sim 1.7 \times 10^{10} \text{ W/cm}^2$ at 1 atm. Quenching corrected data for	

the case of CO (6%), CO₂ (5%), N₂ (65%), and He (24%) use the same scale on the left as for the case of CO (6%) and He (94%). The uncorrected data use the scale on the right. Error bars represent $\pm\sigma$ 60

Figure 3.5 CO fs TP-LIF signal at varying pressure from two different point of imaging. In the presence of forward lasing, signal along the beam path is expected to be much higher than the signal transverse to the beam path. Total signal accumulated on the camera is plotted. Laser irradiance was $\sim 1.7 \times 10^{10}$ W/cm² at 1 atm. 61

Figure 3.6 Attenuation of the UV laser in the mixing chamber at different pressures. (a) Spectra of the transmitted unfocused 230.1 nm beam from the mixing chamber filled with CO (6%) and N₂ (94%). (b) Normalized area under the curve. Almost 20% of the input energy is lost in the chamber as the pressure rises to 20 atm. For pressure scaling of CO fs TP-LIF signal, a correction factor was introduced from this experiment. 63

Figure 3.7 Spectra of transmitted 230.1 nm beam after two-photon absorption in the mixing chamber containing CO and N₂ at different conditions: (a) At atmospheric conditions approximately ideal two-photon absorption can be seen from the unfocused beam without two-photon absorption (red) and focused beam with two-photon absorption (grey). Laser irradiance of the focused beam was $\sim 1.7 \times 10^{10}$ W/cm² at 1 atm. (b) Varying pressure, fixed CO mole fraction of 6%. As the pressure increases certain absorption features can be seen in the spectrum. (c) Fixed N_{CO} , and varying pressure. The intensity of the features is independent of pressure. (d) Varying laser irradiance at 20 atm. Intensity of the feature increases with laser irradiance. (e) Detuning the laser off two-photon resonance eliminates this feature at any pressure (shown for 20 atm). (f) Transmitted focused beam at 2% CO, with perturbing absorption features nearly eliminated. Arrows indicate absorption features from a 2+1 photoionization process. 64

Figure 3.8 Spectra of transmitted 230.1 nm focused beam after two-photon absorption in the mixing chamber containing CO (6%) and N₂ (94%) measured at the upper limit atmospheric pressure laser irradiance of 6×10^9 W/cm². The 2+1 photoionization absorption feature is absent over the pressure range of 1–20 atm at this irradiance. 66

Figure 3.9 CO fs TP-LIF signal at various pressures and (a) varying CO mole fractions. (b) CO fs TP-LIF signal corrected for the actual irradiance available at the probe volume for a mixture of CO (6%) and N₂ (94%) as estimated from measurements of the transmitted laser energy. Laser irradiance at the probe volume was $\sim 6 \times 10^9$ W/cm² at atmospheric pressure. 67

Figure 4.1 Energy level diagram of the $3p^3P_{J'=0,1,2} \leftarrow 2p^3P_{J''=0,1,2}$ atomic oxygen transition excited at 226 nm. Inset shows multiple in-phase photon-pairs in the broadband fs excitation pulse contributing to the resonant transition. 70

Figure 4.2 Experimental setup of the fs laser, spectrometer, and imaging system for atomic O fs TP-LIF. 72

Figure 4.3 Atomic oxygen TP-LIF signal dependence on the laser excitation wavelength at 1 and 5 atm showing normalized experimental data (symbols) with a Gaussian fit (line) at 1 and 5 atm. Laser energy was 5 μ J/pulse. Error bars represent $\pm\sigma$ 74

Figure 4.4 Atomic oxygen TP-LIF signal dependence on the excitation laser energy at 1 and 5 atm. 5 μ J/pulse corresponds to an irradiance of $\sim 10^{11}$ W/cm². Error bars represent $\pm\sigma$ 75

Figure 4.5 O-atom fs TP-LIF signal originating from 100% O ₂ at room temperature. Based on signal levels for 1% O ₂ mole fractions in Figure 4.4. laser generated O atoms from O ₂ account for much less than 1% of the TP-LIF signal in a $\phi = 0.95$ flame.....	76
Figure 4.6 Comparison of O mole fractions from equilibrium theory and experimental O-atom fs TP-LIF signals at various equivalence ratios for pressures of (a) 1 atm and (b) 5 atm in H ₂ /Air Hencken burner flame products. Laser energy was 5 μ J/pulse in probe volume. Error bars represent $\pm\sigma$. (c) Theoretical quenching rates as a function of equivalence ratio assuming equilibrium concentrations of major quenching species of the products of H ₂ /Air combustion.....	77
Figure 4.7 Accumulation of 700 shots (upper row) and single-shot (lower row) O-atom fs TP-LIF signals at various pressures. The main flow exit of the Hencken burner was 25.4 \times 25.4 mm. Laser beam was approximately 10 mm above the burner surface. Two different scales have been used to represent accumulated and single-shot images because of significant variation in respective signal levels.	79
Figure 4.8 Fs TP-LIF signal of atomic oxygen and normalized N_o/Q_2+A_2 at different pressures in a $\phi = 0.85$ H ₂ /Air Hencken burner flame. Both curves are normalized to the corresponding atmospheric pressure value. Laser energy of 5 μ J/pulse. Error bar presents $\pm\sigma$	80
Figure 5.1 Schematic of experimental setup, including three-pulse CARS optical configuration and high-pressure vessel with Hencken burner flame.	85
Figure 5.2 Time-dependent magnitudes of simulated (a) molecular response functions, $R_4(t)$, of N ₂ at $T = 1700$ K and $P = 1.0$ and 6.6 bar and (b) probe electric fields at two delays ($\tau_{23} = 233$ fs and 32.1 ps).....	86
Figure 5.3 Normalized averaged (1500 laser shots) experimental CARS spectra at several P and τ_{23} . Panels (a), (c), and (e): spectra from H ₂ –air flames at fuel:air equivalence ratio, $\phi = 0.36$ and $P = 1, 4.5,$ and 10 bar. Panels (b), (d), and (f): spectra from CH ₄ –air flames at $\phi = 0.8$ and $P = 1, 3.3,$ and 6.6 bar. Probe-pulse delays include 233 fs [panels (a) and (b)], 32.1 ps [panels (c) and (d)], and 100 ps [panels (e) and (f)]. Dashed vertical lines: positions of ($2 \leftarrow 1$) and ($1 \leftarrow 0$) vibrational bandheads.....	88
Figure 5.4 Pressure-dependent single-laser-shot results for $\tau_{23} = 233$ fs for CH ₄ –air flame, $\phi = 0.8$. Panels (a)–(c): example single-shot spectra at three pressures (1, 3.3, and 6.6 bar, respectively) and corresponding best-fit simulations at denoted temperature. Inset histograms depict probability densities for 1500 laser shots. Panel (d): statistical average of best-fit T (1500 single-shot spectra) at $\tau_{23} = 233$ fs and several values of ϕ for these three pressures. Error bars ($1-\sigma$) are included for $\phi = 1.25$; comparable relative magnitudes are observed at all ϕ (excluded for clarity). Calculated T_{ad} denoted by vertical dashed curves.	89
Figure 6.1 Experimental set-up. (a) Two-beam RCARS setup. (b) Layout of the narrowband spectral amplifier; VBG: volume Bragg grating, HWP: half wave plate, PH: pinhole, OI: optical isolator, PBS: polarizing beamsplitting cube, TFP: thin film polarizer, FR: Faraday rotator. (c) Small-signal-gain of the diode-pumped Nd:YAG amplifier modules; D: Diameter, L: Lenth, Solid line: Single exponential fit.	94

Figure 6.2 Amplifier output characteristics at 1064.4 nm. (a) Input vs. output energy for both VBGs; Error bars: $\pm\sigma$, Solid lines: linear fit. (b) Pulse-to-pulse stability of input and amplified output. (c) Beam quality, M^2 . (d) Near-field beam profile. (e) Far-field beam profile. 96

Figure 6.3 Frequency and time-domain characteristics of amplified beam after SHG. (a) Measured spectrum of 532.2 nm beam; $\Delta\nu$: bandwidth. (b) Time-domain cross-correlation of the same. .. 97

Figure 6.4 Measured RCARS spectra. 1000 shots averaged at $\Phi = 2.5$ and 1.2 (left column) and 1000 single-laser-shot temperature histograms (right column). 1.9 cm^{-1} ; 10-ps probe. Probe delay 19.5 ps. 99

Figure 6.5 Example single-shot spectra at $\Phi = 2.5$ (top) and 1.2 (bottom) and the corresponding best-fit simulations at the noted temperatures. 100

LIST OF ABBREVIATIONS

CARS	Coherent Anti-Stokes Raman Scattering
CMOS	Complementary Metal–Oxide–Semiconductor
CSRS	Coherent Stokes Raman Scattering
ECS	Energy-Corrected Sudden
EMCCD	Electron Multiplied Charged Couple Device
fs	Femtosecond
FT	Fourier Transform
FWHM	Full Width at Half Maximum
ICCD	Intensified Charged Couple Device
IFT	Inverse Fourier Transform
MEG	Modified Exponential Gap
Nd:YAG	Neodymium-doped Yttrium Aluminum Garnet
NR	Non-Resonant
ns	Nanosecond
OPA	Optical Parametric Amplifier
ps	Picosecond
RCARS	Rotational Coherent Anti-Stokes Raman Scattering
RDC	Rotating Detonation Combustor
REMPI	Resonance-Enhanced Multiphoton Ionization
RET	Rotational Energy Transfer
SFG	Sum Frequency Generation
SHBC	Second Harmonic Bandwidth Compressor
SHG	Second harmonic Generation
SNR	Signal to Noise Ratio
SSG	Small Signal gain
SSSF	Small Scale Self Focusing
TBP	Time-Bandwidth Product
TL	Transform-Limited
TP-LIF	Two-Photon Laser-Induced Fluorescence
VBG	Volume Bragg Grating
VCARS	Vibrational Coherent Anti-Stokes Raman Scattering
VUV	Vacuum Ultraviolet Wavelength
WBSF	Whole Beam Self Focusing

ABSTRACT

Ultrafast laser-based diagnostic techniques are powerful tools for the detailed understanding of highly dynamic combustion chemistry and physics. The ultrashort pulses provide unprecedented temporal resolution along with high peak power for broad spectral range—ideal for nonlinear signal generation at high repetition rate—with applications including next-generation combustors for gas turbines, plasma-assisted combustion, hypersonic flows and rotating detonation engines. The current work focuses on advancing (i) femtosecond (fs) two-photon laser-induced fluorescence, and (ii) hybrid femtosecond/picosecond vibrational and rotational coherent anti-Stokes Raman scattering (fs/ps RCARS and VCARS) to higher pressures for the first time.

Quantitative single-laser-shot kHz-rate concentration measurements of key atomic (O-atom) and molecular (CO) species is presented using femtosecond two-photon laser-induced fluorescence (TP-LIF) for a range of equivalence ratios and pressures in diffusion flames. A multitude of signal-interfering sources and loss mechanisms—relevant to high-pressure fs TP-LIF applications—are also quantified up to 20 atm to ensure high accuracy. The pressure scaling of interferences take into account degradation, attenuation and wave-front distortion of the excitation laser pulse; collisional quenching and pressure dependent transition line-broadening and shifting; photolytic interferences; multi-photon ionization; stimulated emission; and radiation trapping.

Hybrid fs/ps VCARS of N₂ is reported for interference-free temperature measurement at 1300–2300 K in high-pressure, laminar diffusion flames up to 10 atm. A time asymmetric probe pulse allowed for detection of spectrally resolved CARS signals at probe delays as early as ~200–300 fs while being independent of collisions for the full range of pressures and temperatures. Limits of collisional independence, accuracy and precision of the measurement is explored at various probe-pulse delays, pressures and temperatures.

Additionally, a novel all diode-pumped Nd:YAG amplifier design is presented for generation of time-synchronized ps-probe pulses for hybrid fs/ps RCARS of N₂. High-energy, nearly transform-limited, single-mode, chirp-free ps probe-pulses are generated at variable pulsewidths. The detailed architecture and characterization of the laser is presented. kHz-rate RCARS thermometry is presented up to 2400 K. Excellent spatial, spectral, and temporal beam quality allowed for fitting the theoretical spectra with a simple Gaussian model for the probe pulse with temperature accuracies of 1–2%.

1. INTRODUCTION

Design of propulsion-systems with improved performance while simultaneously reducing pollutant emission requires complete understanding of fundamental fuel combustion that proceeds through multi-scale kinetic reactions and complex flows at elevated pressures. Combustion involves multitude of elementary reaction steps with varying time and length scales ranging from atomic excitation to turbulent transport [1]. Since most technologies of interest to actual propulsion applications operate at Reynolds numbers that are inaccessible to direct numerical simulation (DNS) [2], even with petascale computational power, the kinetic and transport models of combustion remain critical. However, many models are not well validated and have large discrepancies due to incomplete and inaccurate reaction mechanisms. Many reaction rates are estimated using scaling laws that are not experimentally validated under realistic turbulence and high-pressure conditions.

Elementary reactions, $\text{H} + \text{O}_2 \rightarrow \text{OH} + \text{O}$, $\text{H} + \text{O}_2 + \text{M} \rightarrow \text{HO}_2 + \text{M}$, and $\text{CO} + \text{OH} \rightarrow \text{CO}_2 + \text{H}$, for example, play dominant roles in chemical kinetics of hydrocarbon or hydrogen combustion [3, 4]. $\text{CO} + \text{OH} \rightarrow \text{CO}_2 + \text{H}$ is the dominant pathway for CO oxidation, while the extended Zeldovich mechanism of NO formation consists of chain reactions, $\text{O} + \text{N}_2 \rightarrow \text{NO} + \text{N}$ and $\text{O}_2 + \text{N} \rightarrow \text{NO} + \text{O}$ [5, 6]. Key chain carriers in fuel oxidation such as H, O and OH play critical roles in turbulence/chemical interactions. From an experimental point of view, most atomic, molecular and radical intermediate species (e.g., O, H, CO, OH, N, CH) are transient, highly temperature dependent, and persist at low concentrations in the flame. These conditions pose significant challenges for quantitative optical measurement techniques. Although there has been significant progress in the development of kinetic and transport models, experimental data on local temperatures and key rate-controlling (atomic, radical, and intermediate) species measured in laminar and turbulent flames at pressures relevant to practical applications are rare and qualitative, leading to large uncertainties in the models. Measurements that may be quantitative at atmospheric pressures may fail to provide quantitative data at elevated pressures because of interferences from a range of incoherent and laser-dependent processes.

Many advanced laser-diagnostics techniques have been explored for the past few decades and successfully applied for characterization of combustions flows employing Q-switched Nd:YAG lasers, excimer lasers, and associated dye lasers [7]. These nanosecond (ns-) lasers offer high pulse

energies for applications in planar linear and nonlinear techniques, and narrow spectral bandwidths for spectroscopic studies of gas-phase combustion species. However, revolutionary advances in the field of ultrafast lasers over the last three decades have opened the door for new measurement technologies, especially in the field of nonlinear spectroscopy [8, 9]. Myriad advantages of ultrafast lasers are realized in terms of high peak irradiance while maintain low average energies, which is required for many interference-free nonlinear diagnostics techniques; unprecedented temporal resolution, which has been exploited to study chemical kinetics and energy-transfer processes; high repetition rates, which has facilitated capturing dynamic phenomena; and broad spectral bandwidths, which is required for efficient nonlinear excitation.

This dissertation aims at extending two nonlinear ultrafast laser-diagnostics techniques—fs TP-LIF and hybrid fs/ps CARS—to high-pressure reacting flows for spatio-temporally resolved species and temperature measurements, respectively. The following sections present a brief overview of the characteristics of ultrashort pulses and a general literature review on TP-LIF and CARS specifically aimed at gas-phase applications. The chapter ends with a phenomenological model to be used for hybrid fs/ps CARS thermometry. Additional literature reviews related to the context of different measurements and applications will be presented in the respective chapters.

1.1 Ultrafast Laser Characteristics

The term “ultrafast” quite simply refers to lasers with a very short burst of electro-magnetic energy with temporal bandwidth on the order of a few picoseconds to a few femtoseconds. These short duration pulses provide high peak powers, broad spectral bandwidth within a single pulse, and high temporal resolution. Thus, these lasers are ideal candidates for nonlinear spectroscopic techniques [10]. Overviews of mode-locked oscillators for generation of ultrafast pulses and their regenerative amplification process can be found in literature [11-15] and will not be discussed here. Rather a brief characterization of such pulses relevant to nonlinear spectroscopy is presented in the following discussion.

1.1.1 Intensity and phase in time- and frequency-domain

Treating the electric field of the pulse as linearly polarized and ignoring the spatial portion of the field, the temporal dependence of the pulse electric field can be written as

$$\varepsilon(t) = \frac{1}{2} \sqrt{I(t)} \exp\{i[\omega_0 t - \phi(t)]\} + c.c. \quad 1.1$$

where t is the time in the reference frame of pulse, ω_0 is the angular frequency of the carrier wave, the time-dependent intensity and phase of the pulse are $I(t)$ and $\phi(t)$, respectively, and both vary slowly with respect to the carrier wave. This assumption is true when the pulses are a few cycles long within the envelope, as is the case for ultrashort pulses used in this dissertation (~ 100 fs). $c.c.$ is the complex conjugate required to make the pulse field real.

The complex amplitude of this wave can be written as

$$E(t) = \sqrt{I(t)} \exp[-i\phi(t)] \quad 1.2$$

Given the field, solving for intensity

$$I(t) = |E(t)|^2 \quad 1.3$$

The pulse electric field in the frequency domain is the Fourier transform of Eq. 1.1

$$\tilde{\varepsilon}(\omega) = \sqrt{S(\omega)} \exp[-i\phi(\omega)] \quad 1.4$$

where $S(\omega)$ and $\phi(\omega)$ are the spectrum and spectral phase and are analogous to their time-domain counterparts (e.g., intensity and temporal phase, respectively).

The temporal phase, $\phi(t)$, holds the frequency vs. time information, and the instantaneous frequency of the pulse can be expressed as

$$\nu_{ins}(t) = \nu_0 - \frac{1}{2\pi} \left[\frac{d\phi}{dt} \right] \quad 1.5$$

Different orders of temporal phase, $\phi(t)$, can be expressed by Taylor series expansion about $t = 0$

$$\phi(t) = \phi_0 + \phi_1 t + \frac{\phi_2}{2} t^2 + \dots \quad 1.6$$

where ϕ_0 , ϕ_1 and ϕ_2 are the zeroth-, first- and second-order temporal phase respectively. A similar expression can be derived for spectral phase, $\phi(\omega)$, which contains the time vs. frequency information

$$\phi(\omega) = \phi_0 + \phi_1(\omega - \omega_0) + \frac{\phi_2}{2}(\omega - \omega_0)^2 + \dots \quad 1.7$$

where φ_0 , φ_1 and φ_2 are zeroth-, first- and second-order spectral phases respectively.

Several important implications of both temporal and spectral phase are summarized below [10, 16, 17]:

1. The zeroth-order phase is identical in both the time and frequency domain, and merely the relative phase of the carrier wave with respect to the envelope. For pulses that are many carrier-wave cycles long, the zeroth-order phase can be viewed as a slight shift of carrier-wave from the peak of the envelope, which has no significant effect on the pulse field.
2. The first-order phase is the linear term in $\phi(t)$ or $\varphi(\omega)$ (Eqs. 1.6 and 1.7 respectively). From the Fourier shift theorem, it can be inferred that a linear phase in time simply corresponds to shift in center frequency, whereas a linear term in the spectral phase corresponds to a shift in time.
3. A pulse is called linearly chirped if it has a nonzero value for second-order phase. A quadratic term in $\phi(t)$ corresponds to a quadratic variation in $\varphi(\omega)$, and vice versa. In the time domain, second-order phase represents linear variation in the instantaneous frequency (see Figure 1.1), whereas, in the frequency domain it corresponds to linear variation in $t_{group}(\omega) = d\varphi/d\omega$. The presence of linear chirp within an optical pulse can significantly decrease the excitation efficiency in a nonlinear spectroscopic technique and should be carefully incorporated in any spectroscopic model using ultrafast lasers.
4. Third or higher-order phases can introduce even more phase distortions in materials having higher-order dispersion, but it is safe to ignore their contribution for experimental situations described in this dissertation. Also, in Eq. 1.1 we ignored the spatial extent of the electric field, which is actually a function of space and time. Situations e.g. pulse shaper or compressors can introduce angular dispersions into the pulse, which would result in spatial chirp [18].

1.1.2 Time-Bandwidth Product (TBP)

A good measure of the degree of chirp in a pulse is the $TBP = \Delta\tau_{FWHM}\Delta\nu_{FWHM}$, where $\Delta\tau_{FWHM}$ and $\Delta\nu_{FWHM}$ are the FWHM duration and bandwidth of intensity, $I(t)$ and spectrum, $S(\omega)$, respectively. The ability of an ultrafast laser pulse to probe molecules on a short-time scale is

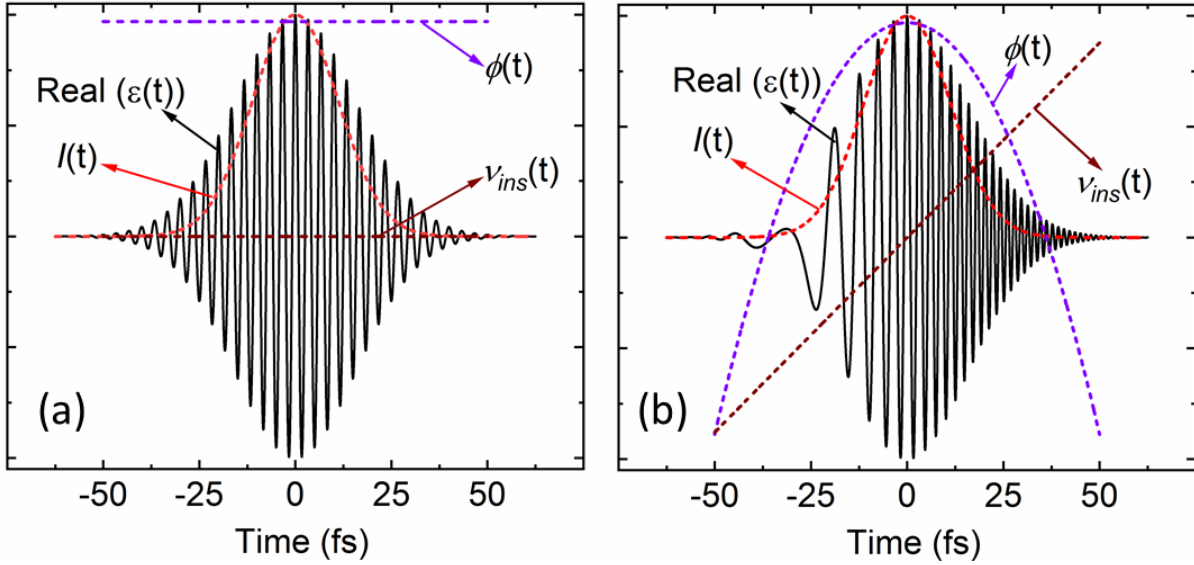


Figure 1.1 Qualitative representation of time-domain characteristics of a 30-fs Gaussian pulse with (a) $\phi(t) = 0$. (b) Second-order phase, $\phi_2 = -0.092 \text{ rad fs}^2$.

linked fundamentally through the Heisenberg uncertainty principle to its inherent broadband nature, facilitating simultaneous excitation of molecular transitions. Again, using Eq. 1.1 for a pulse with a Gaussian envelope function, the time-domain electric field can be expressed as

$$\varepsilon(t) = \exp\left\{-4 \ln 2 \left(\frac{t}{t_{FWHM}}\right)^2\right\} \times \exp\{i[\omega_0 t - \phi(t)]\} \quad 1.8$$

where t_{FWHM} is the temporal bandwidth of the envelop wave. For a flat temporal phase, $\phi(t) = \phi_{const.}$, and the Fourier transform of Eq. 1.8 gives the electric field in the frequency domain

$$\tilde{\varepsilon}(\omega) = A_0 \exp(-i\phi_{const.}) \exp\left\{-\left[\frac{\omega - \omega_0}{\Delta\omega_0}\right]^2\right\} \quad 1.9$$

where A_0 is a constant and $\Delta\omega_0 = 4\sqrt{\ln 2}/t_{FWHM}$. Therefore, the TBP for a Gaussian pulse

$$\Delta\tau_{FWHM} \Delta\nu_{FWHM} = \frac{t_{FWHM}}{\sqrt{2}} \frac{\Delta\omega_0}{2\pi} \sqrt{2 \ln 2} = \frac{4 \ln 2}{2\pi} = 0.441 \quad 1.10$$

This is the smallest TBP that can be attained for a Gaussian pulse. A Gaussian pulse having a TBP of 0.441 is called transform-limited (TL) pulse, and photon pairs within this optical pulse are said to be “in-phase”. Similar analyses can be carried out for different pulse shapes and their corresponding TBPs are summarized in Table 1.1.

Table 1.1 Time-Bandwidth Products for TL pulse shapes.

Pulse shape	TBP
Gaussian	0.441
Sech ²	0.315
Lorentzian	0.142

1.2 Two-Photon Laser Induced Fluorescence (TP-LIF)

Laser-Induced fluorescence (LIF) spectroscopy enables *in-situ* detection of flame radicals and pollutant species and has, therefore, been used for species-selective measurements in reacting flows for several decades and been extended to two-dimensional (2D) imaging via planar LIF in many situations [19-23]. Excellent spatial resolution, species-selective excitation and emission, and high sensitivity of LIF makes this technique a suitable candidate for detection of flame radicals and intermediate species. However, for many of the species of interest, in practical reacting flows, the electronic transitions lie in the vacuum ultraviolet wavelength (VUV) range, where most combustion systems are optically opaque and not accessible via single-photon excitation. Alternatively, two-photon (TP) excitation schemes have been suggested and successfully applied for excitation in the ultraviolet range and detection of flame species at red-shifted wavelengths. Hence, TP-LIF enables access to a variety of atomic and molecular species that are critical for understanding chemical kinetics in reacting systems.

Traditionally, ns-duration lasers were used for TP-LIF measurements of atomic and molecular species of interest. Challenges associated with ns-duration lasers, however, include perturbation of flame chemistry by the relatively high fluence of ns-pulses required to overcome the relatively small two-photon absorption cross section, and estimation of temperature- and pressure- dependent quenching rates. Moreover, complex spectral overlap corrections would be required for ns-TP-LIF measurement at high-pressure due to pressure-dependent atomic and molecular line broadening and shifting [24-29]. Alternatively, since the TP-LIF signal depends strongly on the laser irradiance (quadratically), ultrashort picosecond (ps) and femtosecond (fs) pulses can be used to provide higher laser irradiance with relatively modest laser energies for stronger TP-LIF signals with reduced or eliminated photolytic perturbation. Femtosecond TP-LIF

has been demonstrated for atmospheric pressure flames, plasmas, or gas mixture for the detection of H [30], O [31, 32], CO [33], N [34], OH [35], NH₃ [36], etc.

The major advantages of fs TP-LIF for measurement of flame species are: (i) higher fluorescence signal yield by virtue of high peak irradiance, (ii) minimal or no effect from photolytic interferences because of the low average energies are required, (iii) the broadband TL fs-pulses provide a multiplexed source of two-photon excitation since all frequencies within the TL-optical pulse contribute simultaneously to the excitation transition, (iv) the broadband nature of the fs pulses has the potential to alleviate the effects of pressure dependent line-broadening and line-shifting—an important feature to be considered for application at elevated pressures, (v) the ability to measure excited-state quenching rate directly—which are detector-bandwidth limited rather than the laser-pulse-width limited. However, the high irradiance fs-pulses can obfuscate the TP-LIF measurement, especially at elevated pressure, by introducing unwanted nonlinear effects into the measurements: (i) 2+1 photoionization of the excited states can lead to loss of TP-LIF signal, (ii) multiphoton absorption and degradation of the UV radiation at the optical windows, (iii) attenuation of the excitation laser beam with pressure, (iv) trapping of fluorescence signals, etc. This dissertation reports on a thorough evaluation of the excitation and detection conditions needed to avoid/assess these perturbing effects and achieve quantitative two-photon laser-induced fluorescence measurements of CO and O-atom in high-pressure flames. Different schemes for fs TP-LIF for several important species in combustion applications are listed in Table 1.2.

1.3 Coherent Anti-Stokes Raman Scattering

Coherent anti-Stokes Raman scattering (CARS) is a nonlinear four-wave-mixing technique that targets molecular transitions between either vibrational or rotational energy states of a polarizable medium using the frequency difference between two electric fields (pump; ω_p and Stokes; ω_s), and subsequent probing of the Raman resonance that exists near the pump/Stokes difference frequencies by a third electric field (probe; ω_{pr})—resulting in a laser-like signal (CARS; ω_{CARS}) with information about the thermodynamic state of the species being probed. CARS has been a powerful measurement technique for gas-phase species and temperature due to its high spatio-temporal resolution and ability to probe harsh reacting environments [37, 38]. Traditionally, CARS measurement was performed with few-Hz nanosecond (ns-) lasers for both thermometry

Table 1.2 Excitation and detection wavelengths for two-photon transitions of different species.

Species	Excitation		Detection		Ref.
	Wavelength (nm)	Transition	Wavelength (nm)	Transition	
CO	230.1	$B^1\Sigma^+ \leftarrow \leftarrow X^1\Sigma^+$	400-700	$B^1\Sigma^+ \rightarrow \rightarrow A^1\Pi$	[29, 39]
	217.5	$C^1\Sigma^+ \leftarrow \leftarrow X^1\Sigma^+$	360-600	$C^1\Sigma^+ \rightarrow \rightarrow A^1\Pi$	[39]
	230.1	$B^1\Sigma^+ \leftarrow \leftarrow X^1\Sigma^+$	280-380	$b^3\Sigma^+ \rightarrow \rightarrow a^3\Pi$	[40]
H	205.1	$3d\ ^2D \leftarrow \leftarrow 1s\ ^2S$	656	$3d\ ^2D \rightarrow \rightarrow 2p\ ^2P$	[27, 32]
O	225.6	$3p\ ^3P \leftarrow \leftarrow 2p\ ^3P$	845	$3p\ ^3P \rightarrow \rightarrow 3s\ ^3S$	[24]
	225.6	$3p\ ^3P \leftarrow \leftarrow 2p\ ^3P$	777	$3p\ ^5P \rightarrow \rightarrow 3s\ ^5S$	[23]
N	206.7	$3p\ ^4S \leftarrow \leftarrow 2p\ ^3^4S$	742-747	$3p\ ^4S \rightarrow \rightarrow 3s\ ^4P$	[41]
OH	620	$A^2\Sigma^+ \leftarrow \leftarrow X^2\Pi$	~310	$A^2\Sigma^+ \rightarrow \rightarrow X^2\Pi$	[35]
NH ₃	305	$C' \leftarrow \leftarrow X$	565	$C' \rightarrow \rightarrow A$	[36]

and species concentration measurements. High accuracy measurements were possible using ns-CARS as multiple transitions could be compared to simulated spectra to extract species concentration or temperature [42]. Initially, ns-CARS was performed by scanning the pump wavelength to measure different molecular transitions directly. The early ns-CARS measurements were demonstrated in realistic combustors, including thermometry in an automotive engine [43], liquid-fueled combustor [38], high pressure environments—incorporating Raman linewidths and line-mixing effects [43-47]—for N₂ and H₂ thermometry up to 40 atm [48]. Simultaneous, multiple species single-shot measurement was made possible by dual-broadband CARS using two broadband dye lasers [49] and applied for thermometry in a combined vibrational and dual-broadband CARS technique [50]. Another variant, dual-pump CARS, was implemented using two narrowband pump beams tuned to different molecule pairs [51] and demonstrated for measurement

in a supersonic combustion tunnel [52-54] and for combined pure rotational and ro-vibrational CARS to cover a broad range of temperatures [55]. This technique was extended to triple-pump CARS to measure concentration and temperature by exciting three different molecules [56], and increased bandwidth dual-pump CARS was used to measure seven species in combustion of a mixture of $\text{H}_2/\text{C}_2\text{H}_4$ [57].

Although ns-CARS has served as a useful tool for gas-phase species and temperature measurement, it suffers from several drawbacks. Firstly, most ns-CARS systems employ commercial Nd:YAG lasers due to their high energy output and the requirement of high laser irradiance for the CARS signal generation, but these traditional lasers systems are limited to tens of Hz repetition rate and pose major limitations in probing dynamic phenomena. Moreover, Stark broadening and stimulated Raman pumping at high laser energies required for ns-CARS [58] and complexities from the nonresonant (NR) background signal [59] as well as high sensitivity to collisional broadening limit the applicability and precision of ns-CARS, especially at application where local pressure is not known a priori and in hydrocarbon-rich environments [60, 61].

To circumvent pulse energy requirements and suppress NR background, picosecond laser systems had been employed in gas phase initially at 10 Hz [62, 63] and very recently at 100 kHz in a burst-mode configuration [64]. Moreover, broadband ps dye lasers were employed to demonstrate pure-rotational [65] and rovibrational [66] N_2 thermometry.

The advent of commercially available kHz-repetition-rate amplified femtosecond lasers introduced the capability of extending measurements to kHz rates. In recent years, several variants of femtosecond time-resolved coherent anti-Stokes Raman scattering (fs CARS) have been developed with particular attention paid toward use of these approaches for combustion diagnostics [9, 67, 68]. The major benefits associated with such ultrafast CARS approaches include the high (1–10 kHz) repetition rates available from commercial ultrafast laser systems and the potential to complete the full measurement on timescales that are fast compared to typical collisional timescales at or near atmospheric pressure [69]. Initial gas phase fs-CARS thermometry [70, 71] and measurement of combustion-relevant species [72] were demonstrated in the time domain. Additionally, due to the fast time-scale over which the fs-CARS measurement are made, thermometry can be performed independent of collisional effects by mapping out coherence decay from 1-3 ps, and was demonstrated in unknown collisional environments at pressures up to 50 atm [73]. However, time-domain CARS required long time duration scanning of a mechanical delay

stage, limiting single-laser-shot capability. Alternatively, chirped probe fs CARS [67] was later developed to map the time domain molecular response to the frequency domain and allowed for single-laser-shot species concentration [74] measurement and thermometry in gas phase at 1-5 kHz [68, 75, 76], albeit with limited ability to isolate chemical species and increased complexity in modeling the nonlinear parameter space associated with the highly chirped probe pulse [77].

For species identification, reduced modeling complexity, and less sensitivity to laser characteristics, an alternative is to utilize a narrowed ps probe-pulse to resolve the single-laser-shot CARS spectrum and was first demonstrated in condensed phase [78, 79] and gas phase [80] measurement. In this hybrid fs/ps CARS technique, initial Raman coherences are typically introduced by broadband fs-preparation pulses, namely pump (ω_p) and Stokes (ω_s), followed by a frequency-narrowed, time-delayed ps-probe (ω_{pr}) pulse that allows for multiplexed detection of the Raman active modes. This technique has shown particularly great promise for extension toward accurate thermometry at elevated pressures, primarily by the simultaneous virtues of a) readily assignable, spectrally resolved temperature-dependent features; b) the rejection of background nonresonant contributions; and c) the ability to complete single-laser-shot measurements within 1–10 ps to avoid collisional broadening effects that occur at longer timescales [81]. Alleviating the need to model collision-dependent effects has been discussed as an important possible benefit of time-resolved CARS approaches [73, 82], particularly since accurate modeling of collisions requires knowledge of colliding-partner mixture compositions.

The main challenge of hybrid fs/ps CARS comes with generating the narrowband ps pulse, which directly drives the spectral resolution of hybrid fs/ps CARS. Two general approaches for generating or shaping of the ps-probe include: (i) phase-locking separate fs- and ps- laser systems (two-laser solution), and (ii) generating a narrowband ps pulse derived from the broadband fs-pulse (single-laser solution). The former has been employed for 20 Hz CARS spectroscopy in gas phase to demonstrate at a point for both rotational and vibrational transitions of multiple species through the application of self-phase modulation [83], in atmospheric pressure flame for one dimensional rotational CARS (1-D) [84, 85], and in room temperature rotational N₂ CARS for plane imaging (2-D) [86]. This approach has been expanded to 1 kHz 2-D rotational CARS up to 700 K by Miller *et al.* [87]. However, the high cost and experimental complexities of two externally synchronized laser systems obfuscate the path to widespread use.

For the single-laser solution, two methods have been demonstrated to generate a ps-probe from the fs-laser source, with a trade-off between energy per pulse and spectral characteristics. The original works on hybrid fs/ps CARS spectral detection [78] and single-laser-shot N₂ vibrational CARS thermometry at flame temperatures [88] used a 4-*f* pulse shaper to generate a spectrally narrow, transform-limited probe pulse with variable ps-pulse width and with increased sensitivity for a range of temperatures from 300 K to 2400 K [89]. Follow-on works also utilized an optical filter [90] or etalon [91] for N₂ single-shot rotational CARS thermometry up to 800 K, or a volume Bragg grating (VBG) [92] for N₂ vibrational CARS thermometry at flame temperature with limitation to single-laser-shot measurement. However, all led to significant reduction in the probe pulse energy (~ 10 $\mu\text{J}/\text{pulse}$) and residual sideband signatures in the spectral and temporal profiles that required care in the experimental and modeling procedures [90, 91]. A nonlinear method by Kearney *et al.* based on the work in Ref. [93] used a second harmonic bandwidth compressor (SHBC) to combine two fs-pulses with linear chirp in opposite directions through sum frequency generation (SFG) to generate a high energy ps-probe pulse. With up to 30% conversion of the fundamental broadband pulse to a narrowband ps-probe pulse with ~ 3.5 cm^{-1} bandwidth and ~ 1.1 mJ/pulse , this approach has been used for fs/ps rotational CARS thermometry up to 2400 K [94, 95] and extended to a dual-pump hybrid fs/ps CARS for rotational/vibrational nonequilibrium energy distribution in a dielectric barrier discharge plasma [96]. However, introduction of imperfect phase conjugation due to instantaneous changes in spatial overlap and difficulty in achieving perfect opposite linear chirp between two pulses during SFG results in spectral wings and blue shifted satellite pulses [97]. This necessitates careful filtering of the ps-probe to avoid non-physical features in the CARS spectra that require extensive modeling effort of the laser pulse characteristics, and often affects the precision of the measurements. This can be potentially circumvented by combining an SHBC and 4-*f* pulse filter, but this approach has only been shown for rotational CARS measurements up to 1000 K and using a probe energy of 5 μJ [97].

In this dissertation, hybrid fs/ps vibrational CARS is explored in a high-pressure diffusion flame with a view towards collision independent accurate and precise thermometry at combustion relevant conditions. Also, a novel ps-probe pulse generation technique is investigated and demonstrated for flame temperatures in a two-beam hybrid fs/ps rotational CARS arrangement.

1.4 Hybrid fs/ps CARS Model

Coherent anti-Stokes Raman scattering is a four-wave mixing technique involving interaction of a polarizable molecular species with three input (optical) electric-field pulses, known as the pump (ω_p), Stokes (ω_s) and probe (ω_{pr}). From the conservation of energy (signal frequency) and momentum (phase matching), the generated CARS signal mode can be expressed as [37, 38, 98]

$$\omega_{CARS} = \omega_p - \omega_s + \omega_{pr} \quad 1.11$$

$$\mathbf{k}_{CARS} = \mathbf{k}_p - \mathbf{k}_s + \mathbf{k}_{pr} \quad 1.12$$

where ω is the frequency and \mathbf{k} is the wave vector along the beam propagation direction. The intensity of the generated CARS signal in frequency domain can be expressed as

$$I_{CARS}(\omega) \propto \left| P_{res}^{(3)}(\omega) + P_{nonres}^{(3)}(\omega) \right|^2 \quad 1.13$$

where $P_{res}^{(3)}$ and $P_{nonres}^{(3)}$ are the complex third-order polarizations arising from resonant and nonresonant (NR) interactions within the sample, respectively. While ns CAR is modeled in the frequency domain and treated as a steady process, fs-CARS modeling is carried out in the time domain. Moreover, in hybrid fs/ps CARS, the initial Raman coherences are prepared by the broadband fs pump and Stokes pulses that decay in time as a result of collisional dephasing, followed by a time delayed narrowband ps pulse used to probe the molecular response. As such, the NR signal, which decays much faster than the resonant contribution, is suppressed as the probe pulse is not overlapped in time with the two fs preparation-pulses and is neglected in the model.

The resonant frequency domain CARS component $P_{res}^{(3)}(\omega, \tau_{12}, \tau_{23})$ is the inverse Fourier transform (IFT) of the time-domain complex polarization

$$P_{CARS}^{(3)}(t, \tau_{12}, \tau_{23}) = \left(\frac{i}{\hbar}\right)^3 \int_0^\infty dt_3 \int_0^\infty dt_2 \int_0^\infty dt_1 [R_4(t_3, t_2, t_1) * E_{pr}(t - t_3) E_s^*(t + \tau_{23} - t_3 - t_2) E_p(t + \tau_{12} + \tau_{23} - t_3 - t_2 - t_1) e^{i(\omega_p - \omega_s + \omega_{pr})t_3} e^{i(\omega_p - \omega_s)t_2} e^{i\omega_p t_1}] \quad 1.14$$

where $E_p(t)$, $E_s(t)$ and $E_{pr}(t)$ represent the complex time-domain electric-field envelopes, and ω_p , ω_s and ω_{pr} are the associated frequencies of the carrier waves of pump, Stokes, and probe respectively. Following the nomenclature in Ref. [98], $R_4(t)$ is the third-order molecular response

function arising from the Raman-active molecular resonances present near the pump-Stokes difference frequency ($\omega_p - \omega_s$). Note that, the spatial component of the electric fields are accounted for in the phase-matching configuration (Eq. 1.12) and not explicitly obvious in Eq. 1.14. Within this equation, the integration variables t_1 , t_2 , and t_3 are the coherence timescales separating field interactions i.e. the pump-Stokes, Stokes-probe, and probe-CARS interactions respectively (see Figure 1.2a). For hybrid fs/ps CARS, the expression can be simplified by the fact that both pump and probe are detuned far from any electronic resonances of the molecular species being probed and the virtual state c is short lived. As such, the third-order response function, $R_4(t)$, over timescales t_1 and t_3 can be assumed to be fast compared to the time-dependence of the pulse electric-field envelopes and dephases instantaneously during both t_1 and t_3 . So, the molecular response function for the first and third coherence timescales can be replaced with delta functions, such that, $R_4(t_3, t_2, t_1) \approx \delta(t_3)R_4(t_2)\delta(t_1)$. Also, for hybrid fs/ps CARS the pump and Stokes pulses arrive the probe volume at the same time ($\tau_{12} \approx 0$), and the probe pulse is delayed ($\tau_{23} > 0$) relative to the pump and Stokes pulses to suppress NR background. As such, Eq. 1.14 reduces to

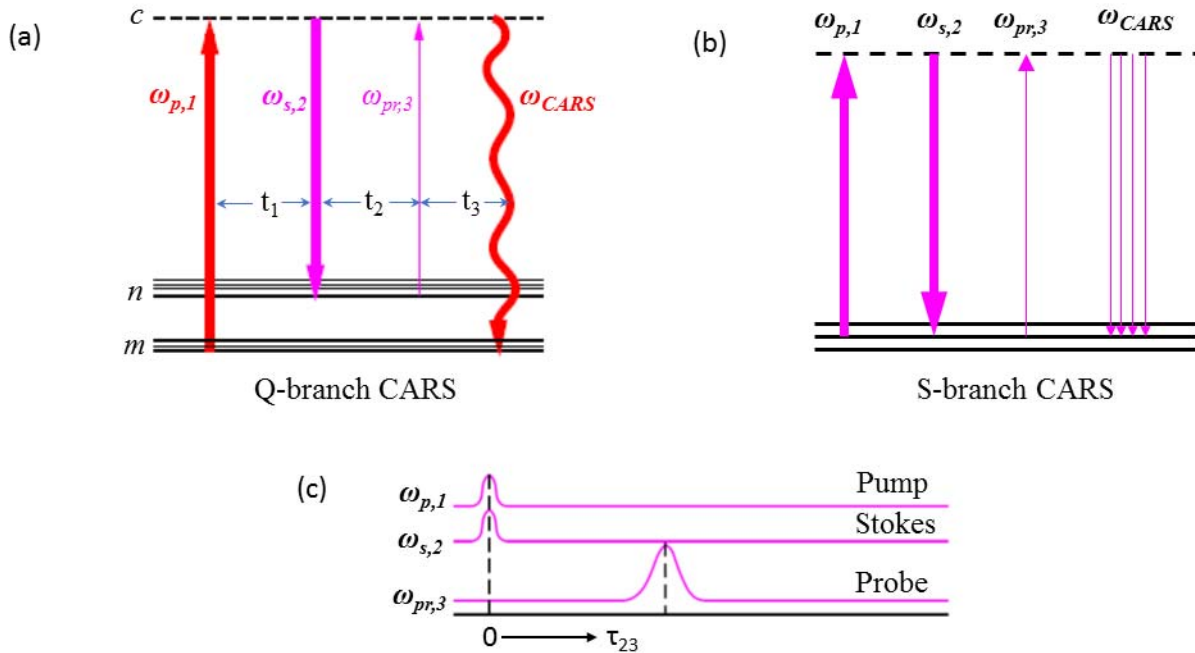


Figure 1.2 Wave-mixing energy level diagram. Frequency-domain diagram: (a) Vibrational CARS; (b) Rotational CARS; (c) Time-domain picture depicting the relative position of different pulses for hybrid fs/ps CARS. Dashed line represents virtual energy state.

$$P_{CARS}^{(3)}(t, \tau_{23}) = \left(\frac{i}{\hbar}\right)^3 E_{pr}(t_3) \int_0^\infty dt_2 [R_4(t_2) * E_s^*(t + \tau_{23} - t_2) E_p(t + \tau_{23} - t_2) e^{i(\omega_p - \omega_s)t_2}] \quad 1.15$$

The complex exponential term in Eq. 1.15 represents the frequency and phase associated with each resonant Raman transition. The term $E_s^* E_p$ product is the convolution of the pump and Stokes lineshapes in frequency-domain, i.e. pointwise multiplication of pump and Stokes electric-field in time-domain. Note that, convolution in either the time- or frequency-domain will be presented by "*" in the formulation of hybrid fs/ps CARS model in this dissertation. The integral in the square bracket is the temporal convolution of molecular response with the pump-Stokes product. There are schools of thought on the way the pump-Stokes electric field can be introduced in the hybrid fs/ps CARS model. Firstly, the pump and Stokes electric fields can be explicitly introduced in the model, as is the case in Eq. 1.15, and by determining the chirp associated with pump and Stokes electric fields using time scans in a non-resonator (e.g., Ar); along with the bandwidths of these pulses, the spectral envelope that spans the observed CARS signal is incorporated in the model [88, 89, 99]. In the second approach, the pump and Stokes pulses are assumed to have infinite bandwidth, i.e. impulsive in time-domain [$E_s(t), E_p(t) \approx \delta(t)$] comparing to the timescales associated with the t_2 and need not to be included in the model [94, 95, 97]; rather the spectral response of the pump/Stokes pulses are imparted on the convolution of the probe and molecular response via multiplication of the modeled molecular response with experimentally obtained NR signal in Ar. From an experimental point of view, for vibrational CARS, where the temperature sensitivity and accuracy is derived from the relative intensity of the spectral features near the bandhead of transitions, the measurement is less susceptible to any chirp associated in the pump and Stokes pulses (chirped pulses are normal in practical high pressure experiment, as the fs beams pass through the windows) and the first method is used in this dissertation. However, to minimize uncertainties in the determination of pump/Stokes chirp, extra floating parameters are used in the model to compensate for any offset of pump/Stokes chirp relative to the nominal measured value. On the other hand, for pure-rotational CARS, especially at flame temperatures, the precision and accuracy of the measurement primarily depend on the well-separated rotational transitions peaks—especially at high J -transitions—where the pump-Stokes bandwidths are limited. Hence, the second approach, where the convolution of pump and Stokes are experimentally measured and recorded in the spectrograph, was found to reduce the modeling parameters and complexity.

1.4.1 Third-order molecular response function

Now, using the assumptions made in the preceding section, the time-domain expression of molecular response function will be presented, which includes the summation of all Raman-active transitions for $n \leftarrow \leftarrow m$ energy levels (see Figure 1.2a)

$$R_4(t_2) = \sum_{m,n} \left(\frac{\partial \sigma}{\partial \Omega} \Delta \rho \right)_{m,n} e^{-i(\omega_{m,n} + \Gamma_{m,n})t_2} \quad 1.16$$

where $\omega_{m,n}$ is the Raman transition frequency for $n \leftarrow \leftarrow m$ transition and given as

$$\omega_{m,n} = \frac{2\pi}{hc} (E_n - E_m) \quad 1.17$$

where the rotational and vibrational energy level, $E_{v,J}$, for a diatomic molecule, such as N_2 , is determined from the Born-Oppenheimer approximation [100]

$$\begin{aligned} E(v, J) &= hc[G(v) + F_v(J)] \\ &= hc\left[\omega_e\left(v + \frac{1}{2}\right) - \omega_e x_e\left(v + \frac{1}{2}\right)^2 + \omega_e y_e\left(v + \frac{1}{2}\right)^3 - \omega_e z_e\left(v + \frac{1}{2}\right)^4 + \right. \\ &\quad \left. [B_e - \alpha_e\left(v + \frac{1}{2}\right) + \gamma_e\left(v + \frac{1}{2}\right)^2]J(J+1) - \right. \\ &\quad \left. [D_e + \beta_e\left(v + \frac{1}{2}\right) + \delta_e\left(v + \frac{1}{2}\right)^2]J^2(J+1)^2\right] \end{aligned} \quad 1.18$$

where, h is Planck's constant; c is the speed of light in a vacuum; $G(v)$ is the vibrational energy term; ω_e is the fundamental vibrational frequency of the oscillator; v and J are the vibrational and rotational quantum numbers, respectively; x_e , y_e , and z_e are higher-order anharmonicity factors that account for unequal spacing of the vibrational states; and $F_v(J)$ is the rotational energy term that includes the vibration-rotation interaction and the centrifugal distortion constants. B_e , α_e , γ_e , D_e , δ_e and β_e are standard Herzberg molecular parameters. The value of these parameters for N_2 are presented in Appendix A.

A diatomic molecular transition is Raman-active if it satisfies the Raman selection rules as presented in Table 1.3 along with their associated branch IDs.

Table 1.3 Raman selection rules.

Transition	Δv	ΔJ	Branch ID
Vibrational (CARS)	± 1	0	Q
Rotational (CARS)	0	+2	S
Rotational (CSRS*)	0	-2	O

*CSRS—Coherent Stokes Raman scattering

Raman transition strength

The term $(\partial\sigma/\partial\omega\Delta\rho)_{m,n}$ in Eq. 1.16 is the Raman transition strength, which includes the differential Raman cross-sections for the respective transition, $\partial\sigma/\partial\omega|_{m,n}$ and population difference between the two energy levels involved in the transition, $\Delta\rho_{m,n}$. The populations of different molecular energy levels are a strong function of temperature and can be described using Boltzmann statistics [100], except where the energy distributions significantly deviate from Boltzmann equilibrium. The population differences for vibrational and rotational CARS transitions can be expressed as

$$\Delta\rho_{v+1,J\leftarrow v,J} = \frac{g_J g_m(J)}{Z(T)} [\exp(-\frac{E(v+1,J)}{k_B T}) - \exp(-\frac{E(v,J)}{k_B T})]; \text{ Q-branch} \quad 1.19$$

$$\Delta\rho_{v,J+2\leftarrow v,J} = \frac{g_J g_m(J)}{Z(T)} [\exp(-\frac{E(v,J+2)}{k_B T}) - \exp(-\frac{E(v,J)}{k_B T})]; \text{ S-branch} \quad 1.20$$

where $Z(T)$ is the total internal energy partition function

$$Z(T) = \sum_v \sum_J g_J g_m(J) \exp[-\frac{E_{v,J}}{k_B T}] \quad 1.21$$

where, in Eq. 1.19–1.21, $g_m(J) = 2J + 1$ is the degeneracy of a rotational energy state (m); k_B is the Boltzmann constant; T is the temperature; $E(v,J)$ is calculated from Eq. 1.18. Note that in Eq. 1.19 and 1.20, the nuclear J -dependent spin factor is included explicitly. For a molecule with symmetric electronic wavefunction (e.g. N₂), this factor can be expressed as

$$\begin{aligned}
g_J &= \left[\frac{g_n(g_n+1)}{2} \right]_{J=\text{even}} \\
g_J &= \left[\frac{g_n(g_n-1)}{2} \right]_{J=\text{odd}}
\end{aligned}
\tag{1.22}$$

where $g_n = 2m_n + 1$ is the nuclear spin degeneracy and m_n is the nuclear spin quantum number (for N_2 , $m_n=1$) [99]. Note that, for Q-branch transitions, there is no vibrational degeneracy. However, for S-branch transitions, there are multiple states in each energy level due to degeneracy. In Eq. 1.20 the population difference between upper and lower states is multiplied by the degeneracy of the initial state.

Raman cross-sections

For Q-branch transitions, the Raman cross-section $\frac{\partial \sigma}{\partial \omega}$ in Eq. 1.16 is defined as [101]

$$\frac{\partial \sigma}{\partial \omega} \propto (v+1) \left[a' F_{iso}(J) + \frac{4}{45} b_{J'',J'} \gamma'^2 F_{aniso}(J) \right]
\tag{1.23}$$

where a' and γ' are the first derivative of the average polarization isotropy and polarization anisotropy with associated isotropic and anisotropic Herman–Wallis factors, $F_{iso}(J)$ and $F_{aniso}(J)$, respectively. The Herman-Wallis factor, $F(J)$, in Eq. 1.23 takes into account the effect of vibration-rotation coupling on spectral line mixing [101],

$$F_{iso/aniso}(J) = 1 - \left[\frac{3}{2} (a_1 + 1) - 4 \frac{p_2}{p_1} \right] \left(\frac{2B_e}{\omega_e} \right)^2 J(J+1)
\tag{1.24}$$

where p_1 and p_2 are the first and second coefficients of either isotropic or anisotropic polarizability expansion [101] and a_1 is the first Dunham coefficient in the power-series expansion of the ground state N_2 molecular potential [102]. $b_{J'',J'}$ in Eq. 1.23 is the J -dependent Placzek-Teller coefficient [103] that represents the overlap in wavefunction of the initial and final states, and for Q-branch transition

$$b_{J,J} = \frac{J(J+1)}{(2J-1)(2J+3)}
\tag{1.25}$$

Now, pure-rotational CARS S-branch transitions only depend on the anisotropic polarization, and

the corresponding Raman cross-section, Harman-Wallis factor and Placzek-Teller coefficients can be formulated as [104, 105]

$$\frac{\partial \sigma}{\partial \omega} \propto \frac{4}{45} b_{J'',J'} \gamma'^2 F_{aniso}(J) \quad 1.26$$

$$F_{aniso}(J) = \left[1 + \frac{p_1}{p_0} \right]_{aniso} \left(\frac{2B_e}{\omega_e} \right)^2 (J^2 + 3J + 3)^2 \quad 1.27$$

$$b_{J,J+2} = \frac{3(J+1)(J+2)}{2(2J+3)(2J+1)} \quad 1.28$$

Note that, the Placzek-Teller coefficients and the Herman-Wallis factors are calculated for the initial state of the transition.

Collisional dephasing rates and Raman linewidths

For N₂ CARS thermometry described in this dissertation, it is assumed that vibrational dephasing is negligible [106], and J -dependent collisional dephasing rates are dominated by RET. The temperature and pressure dependent collisional dephasing rates, $\Gamma_{m,n}$, in Eq. 1.16 has been studied for different combustion relevant species [45, 47, 60, 107-109]. Empirical results thus acquired are typically fit to scaling laws such as the modified exponential gap (MEG) law [45] and different variants of energy-corrected sudden (ECS) approximation [73, 110, 111]. Unfortunately, parameterized fits of these modified ECS models to linewidths measured at the high temperatures (1000–2500 K) associated with combustion have not been reported to date. As such, best-fit empirical parameters associated with a MEG model of RET for N₂ were used, obtained via fitting of experimental linewidths at elevated pressures and temperatures [45, 112, 113].

According to MEG model, the pressure- and temperature-dependent rates for upward transitions from rotational state i to j ($i < j$) construct the lower triangular matrix of $\Gamma_{m,n}$, and given as

$$\gamma_{ji} = \alpha P \frac{1 - \exp[-m]}{1 - \exp\left[-\frac{mT}{T_0}\right]} \left(\frac{T}{T_0} \right)^n \left(\frac{1 + \frac{aE_i}{k_B T \delta}}{1 + \frac{aE_i}{k_B T}} \right) \exp\left[\frac{-\beta E_{ij}}{k_B T} \right] \quad 1.29$$

where P and T represent pressure and temperature, respectively; α , β and δ represent adjustable parameters that are optimized by least-squares fitting of experimental results at $T_0 = 295$ K; m is an additional adjustable parameter that allows for optimal simulation of experimentally measured J -dependent linewidths; a is a species-dependent constant; and exponent n accounts for the temperature dependences of the collisional RET rates. The values of all MEG model parameters used in this dissertation are presented in Appendix A.

The upper triangular matrix of $\mathbf{\Gamma}_{m,n}$, which includes all the downward transitions, is readily available from microscopic reversibility

$$\gamma_{ij} = \frac{2J_i + 1}{2J_j + 1} \gamma_{ji} \exp \left[\frac{E_{ij}}{k_B T} \right] \quad 1.30$$

The off-diagonal elements of $\mathbf{\Gamma}$ matrix are relatively small compared to the diagonal elements at pressures where line-mixing effects are negligible (i.e. at low gas densities), and diagonal elements only are enough to represent frequency-domain Lorentzian linewidths of Q-branch transitions

$$\Gamma_{J,J} = \sum_{i \neq j} (\gamma_{ji} + \gamma_{ij}) \quad 1.31$$

Following the work of Martinsson *et al.* [47], the diagonal elements of $\mathbf{\Gamma}$ can be used to approximate S-branch linewidths for a transition between states $J + 2 \leftarrow J$ and this approximation is valid if inelastic collisions mostly contribute to the broadening

$$\Gamma_{J+2,J} = \frac{1}{2} (\Gamma_{J,J} + \Gamma_{J+2,J+2}) \quad 1.32$$

For pure rotational CARS, where the transitions are largely separated, increased pressure threshold is observed even at pressures as high as 70 atm [97], and collisional narrowing effect can be neglected in the model. However, under high-pressure conditions off-diagonal elements, which represent state-to-state RET, become significant and it is necessary to account for line-mixing effects, as is the case for high-pressure vibrational CARS. In these situations, the \mathbf{G} -matrix formalism [106] is readily available and is included in the hybrid fs/ps CARS model. Here, \mathbf{G} is a block-diagonal matrix, where each square submatrix contains information on the collisional relaxation and Raman transition frequencies corresponding to each vibrational manifold

$$\mathbf{G}_v = -\mathbf{\Gamma} + i\omega_{v,J} \mathbf{I} \quad 1.33$$

where $\mathbf{\Gamma}$ is the $n \times n$ relaxation matrix and $\omega_{v,J}\mathbf{I}$ represents a diagonal $n \times n$ matrix containing Q-branch transitions of the $v+1 \leftarrow v$ ($J = 0$ to $J_{\max} = n-1$). Diagonalization of \mathbf{G} -matrix produced a series of eigenvalues that contains transition frequencies, $\tilde{\omega}_{m,n}$, and linewidths, $\tilde{\Gamma}_{m,n}$, and are the new input parameters in Eq. 1.16 to simulate the time-domain molecular response function.

Finally, the CARS signal intensity in time-domain is calculated as

$$I_{CARS}(t, \tau_{23}) = \left| \left(\frac{i}{\hbar} \right)^3 E_{pr}(t) \int_0^{\infty} dt_2 [R_4(t) * E_s^*(t + \tau_{23} - t_2) E_p(t + \tau_{23} - t_2) e^{i(\omega_1 - \omega_2)t_2}] \right|^2 \quad 1.34$$

Invoking the Fourier transform, the CARS signal intensity in the frequency-domain matching experimentally measured CARS spectra can be calculated as

$$I_{CARS}(\omega, \tau_{23}) = \left| \int_{-\infty}^{+\infty} \left(\frac{i}{\hbar} \right)^3 E_{pr}(t) \int_0^{\infty} dt_2 [R_4(t) * E_s^*(t + \tau_{23} - t_2) E_p(t + \tau_{23} - t_2) e^{i(\omega_1 - \omega_2)t_2}] e^{-i\omega t} dt \right|^2 \quad 1.35$$

Appendix. A contains all the molecular constants and fitting parameters for hybrid fs/ps N₂ CARS that are used in this dissertation.

1.4.2 Hybrid fs/ps CARS model implementation and data fitting procedure

Generation of temperature and pressure dependent spectral library

Table 1.4 is a pictorial demonstration of the implementation of hybrid fs/ps CARS model for both vibrational and rotational CARS thermometry. As stated earlier, for vibrational CARS the pump-Stokes pulse is explicitly included in the model, whereas for rotational CARS the spectral envelop that spans the observed CARS signal is imparted to the model from experimentally measured NR signal in Ar. The simulated spectra in Table 1.4 are generated for $P = 1$ atm and $T = 2400$ K for both cases. In the simulation probe delays (τ_{23}) of 32.1-ps and 20-ps were used for vibrational and rotational CARS, respectively. For both cases, a Gaussian probe pulse with 3.25 cm^{-1} spectral bandwidth was used. The pump, Stokes and probe wavelength were 675 nm, 800 nm and 800 nm for VCARS, while the same for RCARS were 800 nm, 800 nm and 532 nm. Note that, for both cases pump/Stokes pulses were 100-fs. In the table "*" stands for convolution of two functions in the respective domain, while "×" represents pointwise multiplication.

Table 1.4 Generation of temperature and pressure dependent spectral library for hybrid fs/ps vibrational and rotational CARS

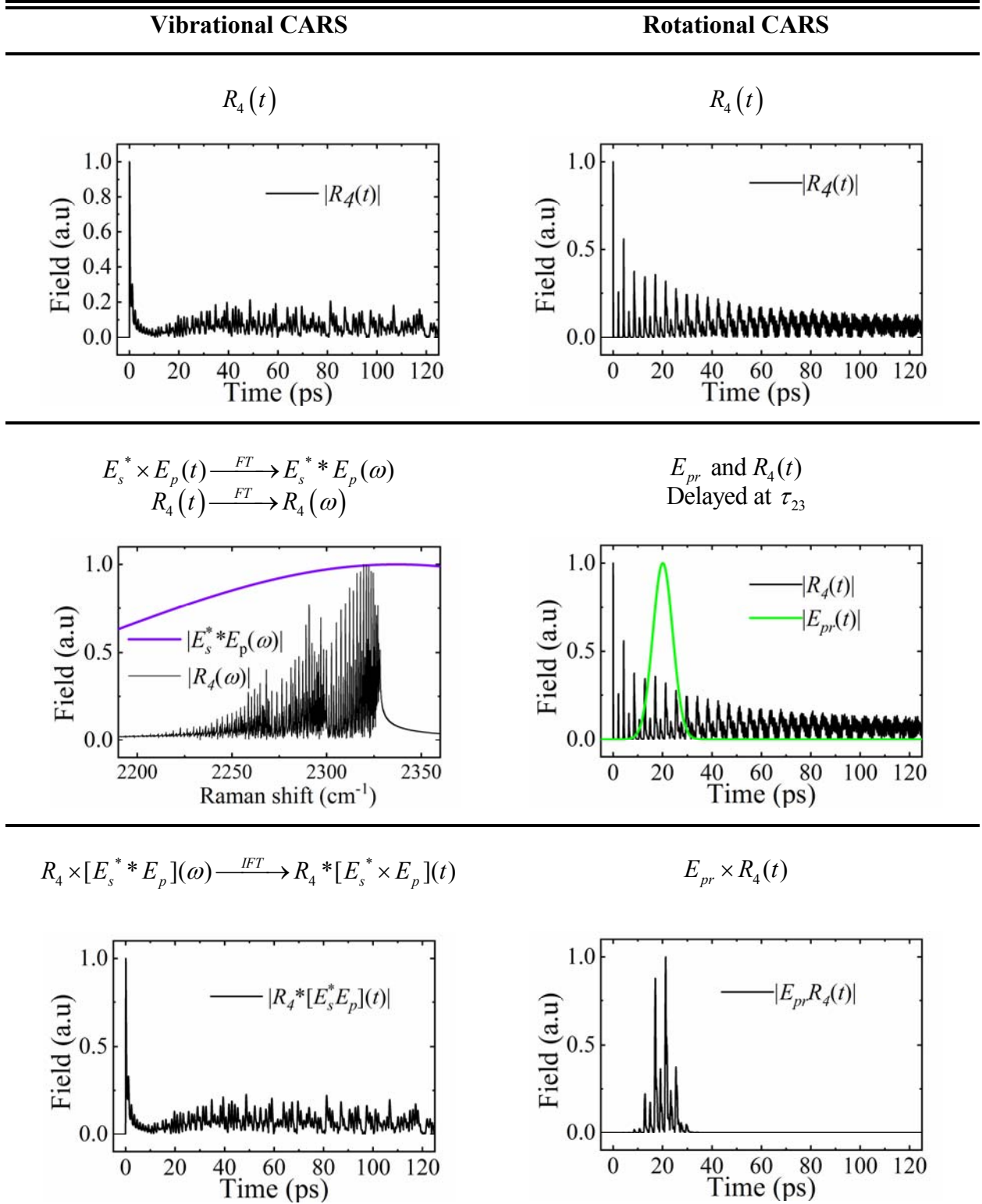
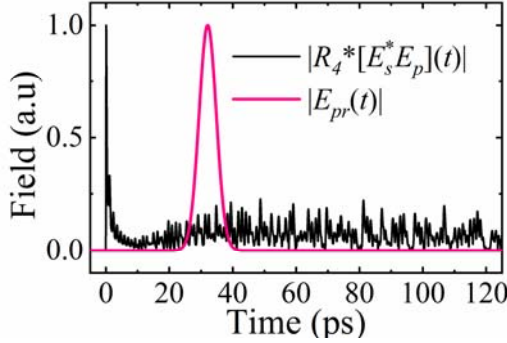
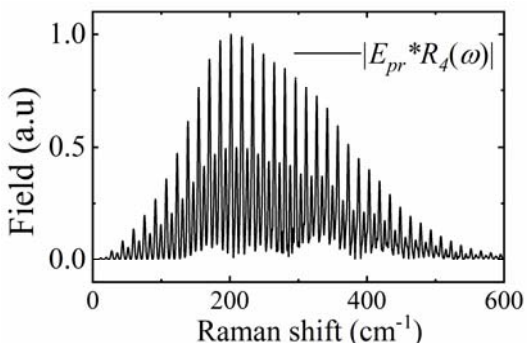
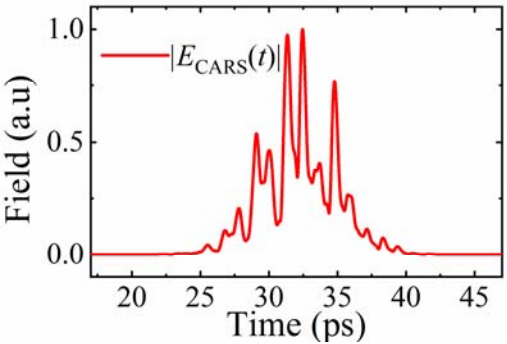
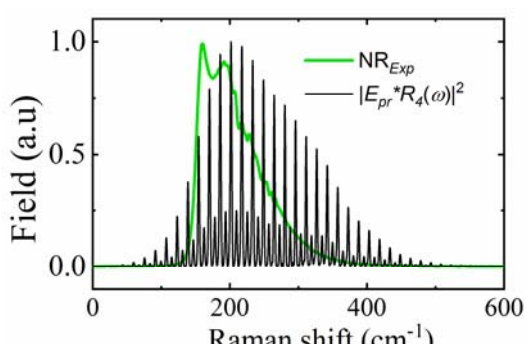
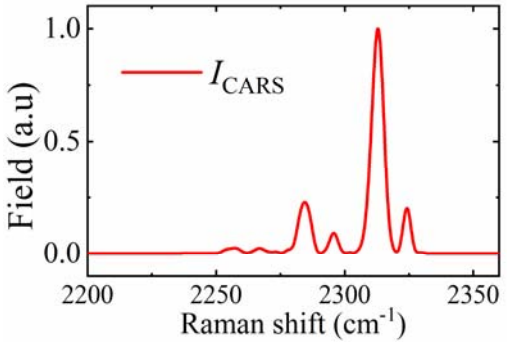
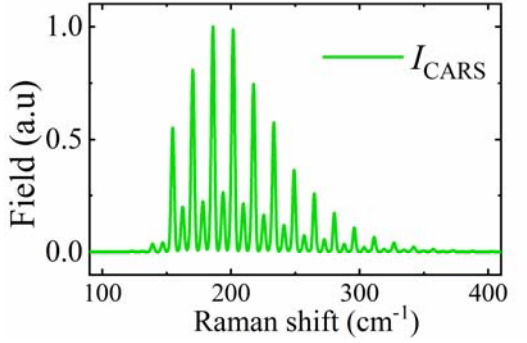


Table 1.4 continued

Vibrational CARS	Rotational CARS
E_{pr} and $R_4^* E_s^* \times E_p(t)$ Delayed at τ_{23}	$E_{pr} \times R_4(t) \xrightarrow{FT} E_{pr}^* R_4(\omega) \sim E_{CARS}(\omega)$
	
$E_{pr} \times [R_4^* E_s^* \times E_p](t) \rightarrow E_{CARS}(t, \tau_{23})$	$E_{CARS}(\omega, \tau_{23}) \xrightarrow{NR_{Exp}} I_{CARS}(\omega, \tau_{23})$
	
$E_{CARS}(t, \tau_{23}) \xrightarrow{FT} E_{CARS}(\omega, \tau_{23}) \rightarrow I_{CARS}(\omega, \tau_{23})$	$I_{CARS}(\omega, \tau_{23})$
	

Experimental data fitting procedure

Once the simulated CARS spectra were generated for different temperatures, a calibrated experimental CARS spectrum with known temperature were fitted with corresponding simulated spectrum at the same temperature to fix floating parameters in the code. These floating parameters included probe-pulse delay offset with nominal τ_{23} , spectral shift in the spectrometer (to match the experimental and simulated wavenumber axis), pump/Stokes bandwidth and chirp offset with nominal measured value (if pump/Stokes-pulse is explicitly included in the model), probe-pulse bandwidth and chirp offset with nominal measured value, center wavelengths, and absolute total signal intensity factor. Once the floating parameters were fixed in the model, the simulated spectra were convolved with a measured instrument function for least-square fitting of the background subtracted experimental data to extract unknown temperatures using a standard nonlinear optimization routine. Temperature was the fitting parameter, along with wavenumber axis shifting and an intensity offset. The objective function minimized by fitting algorithm is

$$R = \sum_{i=1}^x r_i^2 \quad 1.36$$

where x is the number of points in each experimental spectrum and r_i represents residual at the corresponding point.

1.5 Dissertation Summary

This chapter presents a preamble on the motivation for this research work with a general literature review on the development and application of two-photon laser-induced fluorescence and coherent anti-Stokes Raman scattering spectroscopy for gas-phase species and temperature measurements, respectively. The theoretical model for hybrid fs/ps CARS thermometry is presented and a comparison between two different approaches for simulating vibrational and rotational CARS spectra are presented. The following describes in brief the organization of the remainder of this dissertation, which includes more specific literature reviews, experimental descriptions, results, and discussion of five main experimental efforts to advance nonlinear spectroscopy at high pressures, each representing a journal article that has been published or submitted for publication. Chapter 2 presents quantitative femtosecond, two-photon laser-induced (fs TP-LIF) fluorescence

measurement of carbon monoxide (CO) in high-pressure flames. Chapter 3 sheds insight on the different loss mechanisms that might perturb high-pressure application of fs TP-LIF technique as applied specifically to detection of CO. Chapter 4 covers quantitative fs TP-LIF of atomic oxygen (O-atom) in a high-pressure H₂/air flame, along with potential effects of high-pressure on collisional quenching and other interferences. Chapter 5 presents collision independent vibrational hybrid fs/ps CARS thermometry at elevated pressures. Chapter 6 introduces a novel ps-probe pulse amplification technique to generate a chirp-free, single-mode ps-probe with flexible TBP for application in rotational CARS thermometry. Chapter 7 contains a summary of this dissertation with directions for future research work.

2. FEMTOSECOND, TWO-PHOTON, LASER-INDUCED FLUORESCENCE (TP-LIF) MEASUREMENT OF CO IN HIGH-PRESSURE FLAMES

Modified from a paper published in *Applied Optics* **57**, 5666-5671 (2018).

K. Arafat Rahman, Karna S. Patel, Mikhail N. Slipchenko, Terrence R. Meyer, Zhili Zhang, Yue Wu, James R. Gord, and Sukesh Roy

Quantitative, kHz-rate measurement of carbon monoxide mole fractions by femtosecond (fs) two-photon, laser-induced fluorescence (TP-LIF) was demonstrated in high-pressure, luminous flames over a range of fuel-air ratios. Femtosecond excitation at 230.1 nm was used to pump CO two-photon rovibrational $X^1\Sigma^+ \rightarrow B^1\Sigma^+$ transitions in the Hopfield-Birge system and avoid photolytic interferences with excitation irradiance $\sim 1.7 \times 10^{10}$ W/cm². The effects of excitation wavelength, detection scheme, and potential sources of de-excitation were also assessed to optimize the signal-to-background and signal-to-noise ratios and achieve excellent agreement with theoretically predicted CO mole fractions at low and high pressure.

2.1 Introduction

Carbon monoxide (CO) is a major pollutant and key intermediate species for many chemical kinetic pathways in combustion systems. In flames it is generated as a byproduct of incomplete combustion of hydrocarbon fuels. Hence, quantitative spatiotemporally resolved measurements of CO concentrations within the flame zone are important for developing a more comprehensive understanding of combustion processes at realistic operating pressures.

Coherent anti-Stokes Raman scattering (CARS) has been used for measurement of CO in fuel-rich flames at atmospheric conditions [114] and could potentially be utilized for measurements at high pressure. Challenges in this approach include the need for pointwise spatial profiling and the influence of collisional broadening at high pressures. The use of fs CARS has been proposed for measurements with reduced sensitivity to collisional broadening, but the applicability for *in-situ* measurements in flame environments has yet to be demonstrated [115]. Absorption spectroscopy has also been utilized for detection of CO in flame environments, albeit with limitations on spatial resolution due to the path-averaged nature of the measurements [116].

Scores of other laser-based diagnostic techniques have been employed for nonintrusive, *in-situ* measurements of CO in atmospheric pressure combustion systems, such as 2+1 resonance-enhanced multiphoton ionization [117], Raman/Rayleigh scattering [118], amplified stimulated emission [119, 120], and laser-induced fluorescence (LIF) [39, 121, 122]. The excellent spatial resolution, species-selective excitation and emission, and high sensitivity of LIF makes this technique a suitable candidate for detection of flame radicals and intermediate species, and it has been used for visualization of different species in reacting flows for the last few decades [19, 123, 124].

The feasibility of CO PLIF has been demonstrated using infrared excitation of vibrational transitions and mid-infrared detection of vibrational fluorescence at room temperature conditions. Because of the lack of gated intensified detectors in this wavelength range, the applicability for use of this approach in luminous high-pressure flames requires further investigation. Alternatively, excitation of electronic transitions allows for ultraviolet (UV) excitation and detection in the visible range where gated intensified cameras are readily available. For species such as CO, however, the electronic transitions lie within the vacuum ultraviolet wavelength range and are not accessible via single-photon excitation. For such species, two-photon (TP) excitation schemes have been successfully applied for excitation in the ultraviolet range and detection of flame species at red-shifted wavelengths [27, 121, 125].

Different schemes have been proposed for TP-LIF of CO, with the most widely used excitation schemes involving nanosecond (ns)-duration laser pulses where two-photons at 230.1 nm excite the CO molecule from the ground $X^1\Sigma^+$ ($v'' = 0$) state to the $B^1\Sigma^+$ ($v' = 0$) state in the Hopfield-Birge system of CO [29, 126]. As the rotational constants are similar for X and B states, multiple rotational lines in the Q -branch are excited, resulting in fluorescence primarily from the $B^1\Sigma^+ \rightarrow A^1\Pi$ Ångström system. Visible fluorescence in the spectral range of 400–625 nm can then be detected without scattering interferences from the excitation beam. Challenges associated with ns-duration lasers, however, include perturbation of flame chemistry by the high energy laser, relatively low signal levels, and estimation of temperature- and pressure- dependent quenching rates [127-129]. Additional challenges are expected with ns TP-LIF at high pressure due to pressure-dependent absorption line broadening and shifting [130].

The presence of photolytic interferences associated with high excitation pulse energies obfuscates the LIF signal and is a major obstacle to accurate and robust measurement of CO using

ns-duration laser pulses. The main sources of photolytic interferences are: 1) photochemical formation of CO from CO₂, 2) CO photoionization in a 2+1 photon process, 3) C₂ cross-talk, and 4) stimulated emission. Nefedov *et al.* proposed a procedure to correct for CO₂ photo-dissociation on CO TP-LIF measurements [131]. An alternative pumping approach ($C^1\Sigma^+ \leftarrow X^1\Sigma^+$) has also been suggested in the literature to eliminate C₂ swan-band emissions; this approach is less influenced by quenching process and associated with a stronger two-photon absorption cross-section but has a much weaker branching ratio for spontaneous emission of the excited state [39].

Alternatively, since the TP-LIF signal depends strongly on the laser irradiance (quadratically), ultrashort picosecond (ps) and femtosecond (fs) pulses can be used to provide higher laser irradiance with relatively modest laser energies for stronger TP-LIF signals with reduced or eliminated photolytic perturbation. Brackmann et al. reported the use of ps lasers to reduce photolytic interferences from C₂ using CO TP-LIF measurements in ethylene–air flames [132]. Further improvement of CO TP-LIF measurements can be achieved using fs-laser excitation, as demonstrated recently in steady and unsteady atmospheric methane-air flames [33, 133].

In addition, because of the inherent broadband nature of femtosecond pulses, it is of interest to investigate the feasibility of such ultrashort lasers in quantitative CO measurements at higher pressures. At these conditions, the effects of collisional quenching may be exacerbated, but the broadband nature of the fs pulses may help to alleviate the effects of line broadening and line shifting. The current work further extends recent advancements in CO fs TP-LIF to evaluate the accuracy of this approach for measurements at high-pressure conditions. A steady laminar CH₄/Air flame with known equilibrium CO concentrations was employed to investigate potential interferences and verify measurement accuracy over a range of fuel-air ratios at elevated pressure. We furthermore investigated laser excitation energy, excitation wavelength, quenching rates, as well as two potential detection systems to maximize the signal-to-background and signal-to-noise ratios at high pressures when flame luminosity becomes a significant concern.

2.2 Experimental Apparatus and Conditions

The laser source for the present study consisted of an 800 nm, 1-kHz, 7.2-mJ/pulse 100-fs full-width at half-maximum (FWHM), regeneratively amplified Ti:sapphire laser system. The primary 7.2 mJ output of the fundamental 800 nm wavelength was split into 4.3 mJ and 2.9 mJ beam paths, and an optical parametric amplifier (OPA) was pumped by the 4.3 mJ beam with the signal output

wavelength at 1291 nm. This beam was frequency doubled twice to produce radiation at 323 nm. Finally, this beam was sum-frequency-mixed with 1.1 mJ of the 2.9 mJ fundamental beam to produce vertically polarized beam with $\sim 50 \mu\text{J/pulse}$ at 230.1 nm. The 230.1 nm output was then guided into the high-pressure test cell via a combination of $f = -1000 \text{ mm}$ cylindrical and $f = +250 \text{ mm}$ spherical lenses to excite two-photon transitions in the $X^1\Sigma^+$ to $B^1\Sigma^+$ system of CO. This optical setup produced a vertical laser sheet that was 2.4 mm high and $200 \mu\text{m}$ wide propagating through the flame. Images were collected at 8 mm above the burner surface. Optical access to the high-pressure test cell (see Figure 2.1) was provided through three 25.4 mm thick UV fused-silica windows purged with nitrogen during operation to avoid water condensation and soot formation. Because of the high peak irradiance of the fs pulses in the deep UV, the choice of window material (Corning 7979) and size of the beam at the cell entrance window was optimized to avoid multiphoton absorption and degradation of the excitation pulse.

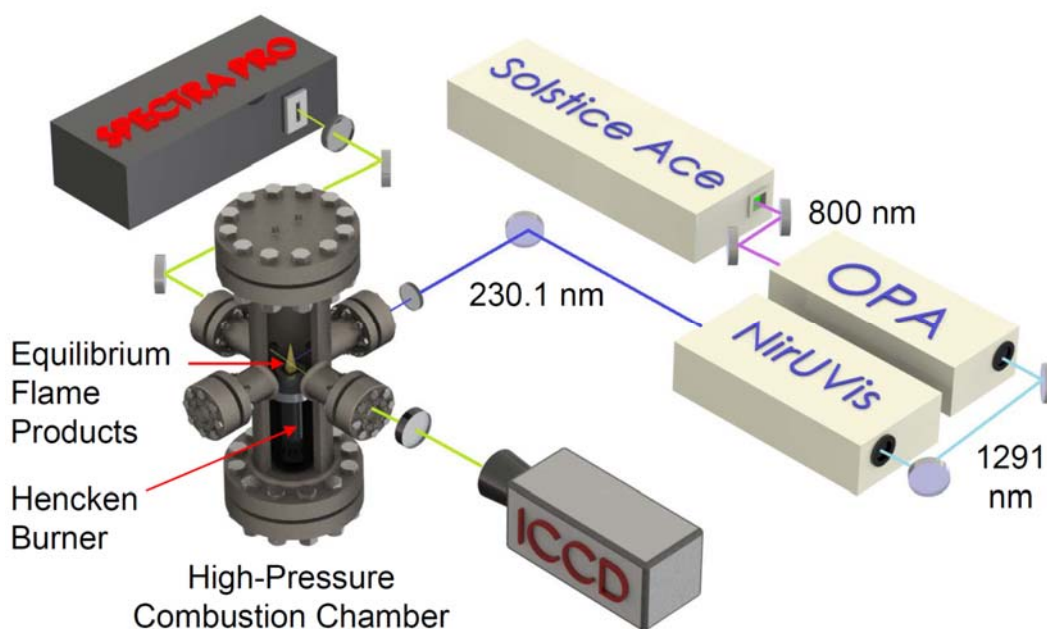


Figure 2.1 Experimental setup of the fs laser, imaging, and spectrally resolved detection system for CO fs TP-LIF.

Images of fluorescence from several CO emission bands were collected using two different detection systems, including: 1) the combination of a high-speed (kHz) image intensifier (IRO, LaVision GmbH) and CMOS camera (FASTCAM SA-Z, Photron), and 2) a low-speed, intensified CCD camera (PI-Max4-SB ICCD, Princeton Instruments). A spectral filter with a transmission

window of 357-521 nm was used to minimize background signals from flame and soot emission. An 85-mm, $f/1.4$ camera lens and a 20-mm lens extender were used to achieve high collection efficiency with high magnification for line imaging.

The fluorescence signal of TP-LIF can be expressed as [28, 29]

$$S_{TP-LIF} = CN_{CO}I_L^{m=2}\sigma \frac{A}{Q + A + P + \sigma_i I_L} \quad 2.1$$

where C represents a group of experimental constants including the solid angle and efficiency of the optical collection system; N_{CO} [cm^{-3}] is the number density of CO in the ground electronic state; σ [$\text{cm}^4 \times \text{s}$] is the two-photon rate coefficient, which is a function of the spectrally integrated two-photon absorption cross-section (σ_0) [134], molecular transition line-shape, excitation frequency, laser linewidth and temperature; I_L [W/cm^2] is the laser irradiance; m is the exponent for irradiance dependency of the TP-LIF signal; A [s^{-1}] is the Einstein coefficient for spontaneous emission [135]; Q [s^{-1}] represents the collisional quenching rate [127]; P [s^{-1}] is the predissociation rate; and σ_i [cm^2] is the photoionization cross-section [136].

2.3 Results and Discussion

2.3.1 Effects of excitation wavelength and energy

The dependence of CO TP-LIF signal on excitation wavelength was examined at two different pressures (1 and 5 atm) by imaging TP-LIF signals in a steady, nearly adiabatic Hencken burner flame [137] for a fuel-rich equivalence ratio, ϕ , of 1.3 and scanning the OPA output wavelength (see Figure 2.2a). An average of 200 images were recorded using the high-speed intensified CMOS camera while varying the OPA wavelength. The intensifier gate width was 100 ns, and an intensifier gain of 80% was used to maximize the signal-to-noise ratio (SNR). The bandwidth of the excitation pulse was found to be in the range of 0.75 nm to 0.8 nm FWHM ($\sim 150 \text{ cm}^{-1}$) at these two different pressures. Variations of $\pm 10\%$ in the $10 \text{ } \mu\text{J}/\text{pulse}$ excitation beam was accounted for during the wavelength scan. While broadening of the absorption line is expected at higher pressure, its effects are minimized by the broadband nature of the fs laser pulse.

It is evident from Eq. 2.1 that the theoretical TP-LIF signal should be proportional to I_L^2 in the absence of photolysis or multi-photon ionization processes. The former can lead to laser-

induced generation of CO molecules, while the latter competes with the TP-LIF process and will limit the signal at higher laser energies.

Hence, the dependence of CO TP-LIF signal on excitation laser energy was investigated at two different pressures (1 and 5 atm) at the same flame condition as mentioned above. Each data point consisted of an average from 200 background-corrected images. The average signal and standard deviation (error bars for $\pm 2\sigma$) are shown in Figure 2.2b. The near quadratic dependence was found at 1 atm (within 2%) and 5 atm (within 6%), indicating very little interference from photolysis or multi-photon ionization up to $\sim 10 \mu\text{J/pulse}$ ($1.7 \times 10^{10} \text{ W/cm}^2$) in both cases. Beyond

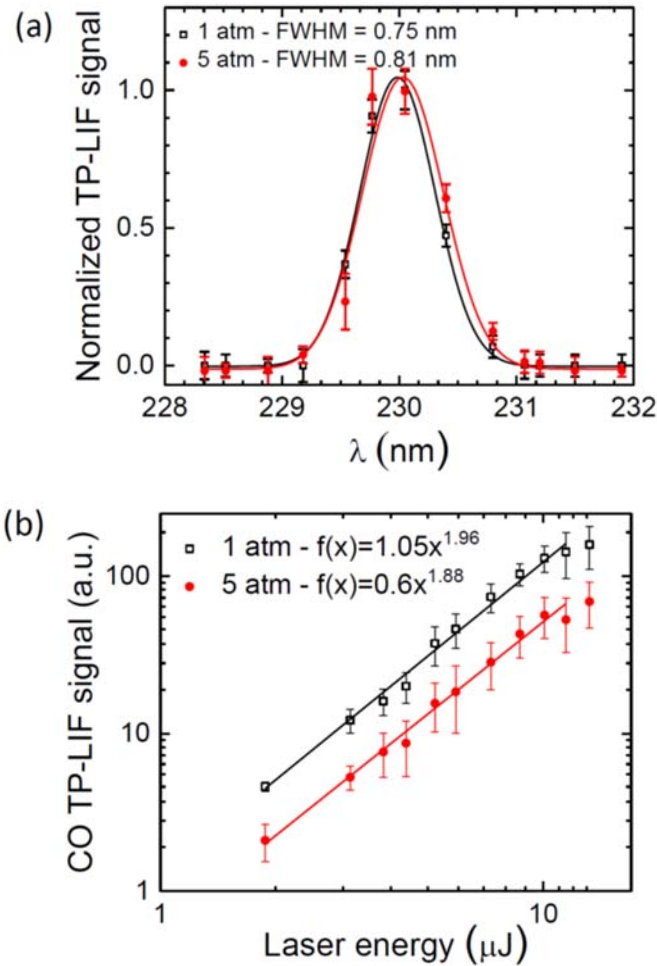


Figure 2.2 (a) CO TP-LIF signal dependence on the laser excitation wavelength at 1 and 5 atm showing experimental data (symbols) with a Gaussian fit (line) and (b) CO TP-LIF signal dependence on the excitation laser energy at 1 and 5 atm. $10 \mu\text{J/pulse}$ corresponds to an irradiance of $\sim 1.7 \times 10^{10} \text{ W/cm}^2$. Error bars represent $\pm \sigma$.

this laser energy, the substantial drop below the quadratic power dependence indicates that competing effects that depend on laser irradiance, such as multi-photon ionization, become significant.

2.3.2 TP-LIF images of the flame profile at high pressure

Figure 2.3 shows averaged and single shot images of CO fs TP-LIF at four different pressures in the CH₄-air Hencken burner flames utilizing an excitation energy of 10 $\mu\text{J}/\text{pulse}$ ($\sim 1.7 \times 10^{10} \text{ W}/\text{cm}^2$). The Hencken burner was used in standard non-premixed configuration that produces flat, uniform, steady, and nearly adiabatic flame after rapid surface mixing [137]. Although we could successfully obtain images beyond 5 atm using Hencken burner, which is designed for atmospheric pressure conditions, at higher pressures the flame structure and luminosity changed significantly. While the Hencken calibration burner normally produces a near-adiabatic flame above a rapid mixing zone, at high pressure the mixing rate appears to be significantly slower, and it is no longer possible to assume flow-field uniformity. Instead, the well-mixed diffusion flame is converted to an array of independent fuel jets that burn as separate diffusion flames [138]. This is due to the inverse relation between pressure and mass-momentum diffusion. For this reason, the quantitative nature of the CO measurement was investigated up to 5 atm, as discussed further below. Nonetheless, the images in Figure 2.3 illustrate that it is feasible to acquire single-shot images of CO fs TP-LIF at high pressure (up to 12 atm) to discern the single-shot structure of the CO concentration field in non-uniform or unsteady flames.

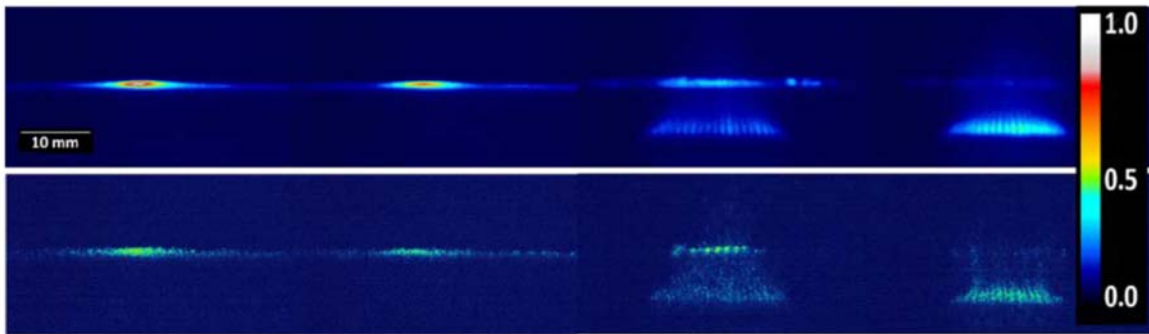


Figure 2.3 Averaged (upper row) and single-shot (lower row) CO fs TP-LIF signals at 1, 4, 8, 12 atm (left to right). Camera: ICCD (PI-Max4-SB). The main flow exit of the Hencken burner was 25×25 mm. Laser sheet was approximately 8 mm above the burner surface.

2.3.3 Effects of flame luminosity and detection system

One of the major challenges with high-pressure measurement of CO fs TP-LIF is background luminosity from the CH₄-air flame [33, 126, 131], which appears near the burner surface at 8 and 12 atm in Fig. Figure 2.3. To optimize the detection scheme, two imaging systems were investigated for the high-pressure TP-LIF measurements, as described in section 2.2. To compare these two systems, 300 single shot images of CO fs TP-LIF signal were collected at identical flame conditions. At 1 atm, the LIF images recorded by the intensifier and CMOS camera combination with a laser irradiance of 1.7×10^{10} W/cm² have a peak single-shot SNR of 30 and a median SNR of 17 with $\sigma = 4.3$. For the same laser irradiance, the ICCD camera has peak SNR of 19 and a median SNR of 13 with $\sigma = 1.6$. As such, the ICCD camera showed very consistent single-shot measurements, while the intensifier-and CMOS camera combination showed better SNR at low pressure conditions and allowed measurements at kHz rates.

To evaluate the effects of flame luminosity at higher pressures, the CO-TP-LIF signal and flame background were recorded from 1–5 atm, as shown in Figure 2.4. For each data point, 300 images were collected and averaged. An intensifier gate of 100 ns was used for intensifier and CMOS camera combination (minimum gate width for the system), while a 15 ns was the gate width was used for ICCD camera, limited by the 5-ns jitter in the fs pulse. While the intensifier and CMOS camera combination shows higher sensitivities and SNR at lower pressures, beyond 4 atm the measurements are limited by the increasingly luminous flame background, which competes with the fs TP-LIF signal and decreases SNR. Thus, it is close to its detection limit with a median SNR of 2 at 5 atm. In contrast, the ICCD has a median SNR of 5 at the same pressure. The improved performance of the ICCD also enables higher-SNR with lower excitation energy to help avoid potential photolytic interferences. In future work, however, it would be of interest to utilize an intensifier and CMOS camera combination with a shorter gate width to improve signal levels and achieve kHz rate single-shot imaging.

Despite the use of a short time gate with the ICCD camera, the effects of background chemiluminescence increased at high pressures relative to the TP-LIF signal. This is illustrated by the fluorescence spectra of Figure 2.5a, which were collected at flame conditions and displayed without background corrections to illustrate the relative effects of flame luminosity. These emission spectra were recorded using a 500-mm spectrometer equipped with a 300 g/mm grating coupled to the ICCD camera. An 85-mm, *f*/1.4 lens was used to direct the fluorescence signal into

the entrance slit. The spectral resolution of the detection system was approximately 4 nm. A total of 10,000 laser shots were accumulated on the ICCD and vertically binned. The averaged spectra in Figure 2.5a are normalized by the highest peak of the CO TP-LIF signal at 1 atm (at 483 nm), such that the figure illustrates the relative of intensities of the signal at 5 atm.

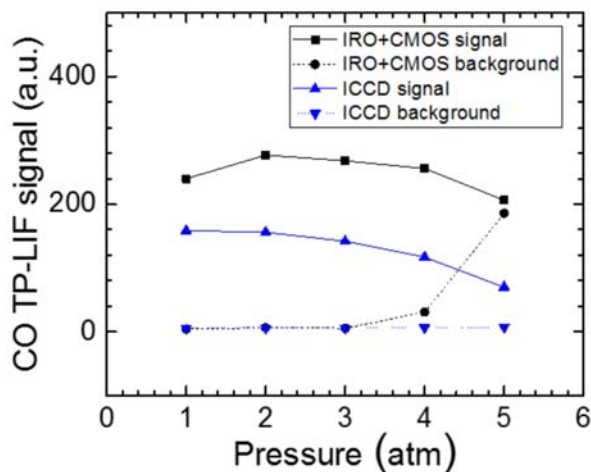


Figure 2.4 CO TP-LIF and flame background signals using an intensifier (IRO) and CMOS camera combination versus an ICCD camera with a shorter time gate for 1–5 atm CH₄-air Hencken burner flames at $\phi = 1.3$.

2.3.4 Potential sources of de-excitation at elevated pressure

The data in Figure 2.5a can also be used to assess potential interferences from photodissociation, or other photochemical effects caused by a high-peak-energy UV laser pulse. To assess the potential impact of these processes at higher pressure, the emission spectra of CO fs TP-LIF signal for CH₄/air Hencken-burner flame ($\phi = 1.3$) were investigated at 1 and 5 atm at slightly higher irradiance (~ 1.3 times) than the irradiance we reported as the multiphoton ionization limit (Figure 2.2b). These interferences can alter the mole fractions of CO or other species in the flame and bias the fs TP-LIF signal measurement, thereby limiting the laser energy that can be utilized for TP-LIF. Major sources of photolysis that might affect the CO TP-LIF measurements include



The detected spectral signature in Figure 2.5a includes strong fluorescence peaks from the $B(v''=0) \rightarrow A$ Ångström band ($v'' = 0, 1, 2, 3, 4$) in the range of 450 nm to 620 nm. It also includes two strong emission lines at 412 nm and 440 nm, which previously had been attributed to the $C^1\Sigma^+ \rightarrow A^1\Pi$ transitions at 412.5 nm (0,2), 438 nm (0,3) and 466.1 nm (0,4) [33]; however, we measured the same spectra in a mixing chamber (cold CO) and found no evidence of these peaks. On the other hand, $B^1\Sigma^+(v''=1) \rightarrow A^1\Pi$ also has emission lines at 412.3 nm (1,0), 439.2 nm (1,1), and 469.7 nm (1,2), which could occur after the excitation of the $X^1\Sigma^+(v''=1) \rightarrow B^1\Sigma^+(v''=1)$ system. The separation between $X^1\Sigma^+(v''=0)$ and $X^1\Sigma^+(v''=1)$ is 2130 cm^{-1} , which is similar to 2050 cm^{-1} for $B^1\Sigma^+(v'=0-1)$. So, the separation between $X^1\Sigma^+ \rightarrow B^1\Sigma^+$ (0-0) and (1-1) diagonal bands is $\sim 80\text{ cm}^{-1}$, which is significantly lower than the laser bandwidth (150 cm^{-1}). Thus, it is possible that both (0-0) and (1-1) bands are excited in flame in which $X^1\Sigma^+(v''=1)$ is substantially populated at high temperatures (see Figure 2.5b). Li *et. al.* performed similar experiments in a McKenna burner premixed flame at atmospheric condition and found very similar results [133]. One potential application of $B(1) \rightarrow A(0)$ emission band might be the quantitative measurement of CO in highly sooty flames where presence of C_2 Swan-band emissions overlaps most of the $B(0) \rightarrow A$ Ångström-band. However, even at rich flames, the combination of low average power i.e. fs-lasers and shorter detection gate width used in these experiments ($\sim 10\text{-}15\text{-ns}$) is sufficient to eliminate C_2 swan band emission (both laser-generated and nascent C_2). As such, the temperature dependence of the associated transition of diagonal bands might be useful in measurement of temperature in flames by CO fs TP-LIF.

Other potential sources of uncertainty in excitation processes for the $B^1\Sigma^+$ state that might affect the TP-LIF signal at elevated pressure may also be considered. Photo-dissociation of CH_4 was not detected as a potential source of interference due to the lack of CH_4 above the Hencken burner at the current flame conditions, as evidenced by the lack of a CH emission line ($A \rightarrow X$) near 430 nm [139]. Another factor that might affect the fs TP-LIF signal is the introduction of second-order phase (linear chirp) in the various optical components. Based on prior work, a factor of 2 decrease in signal might result because of chirped pulses that is common from an OPA [35]. This may be exacerbated as the beam propagates through the focusing lens and cell window, and was the reason of narrower excitation bandwidth than the laser bandwidth in Figure 2.2a. However, this should not affect the quantitative nature of the measurement as it is consistent for a specific pressure condition, although it could impact the detection limits at higher pressure.

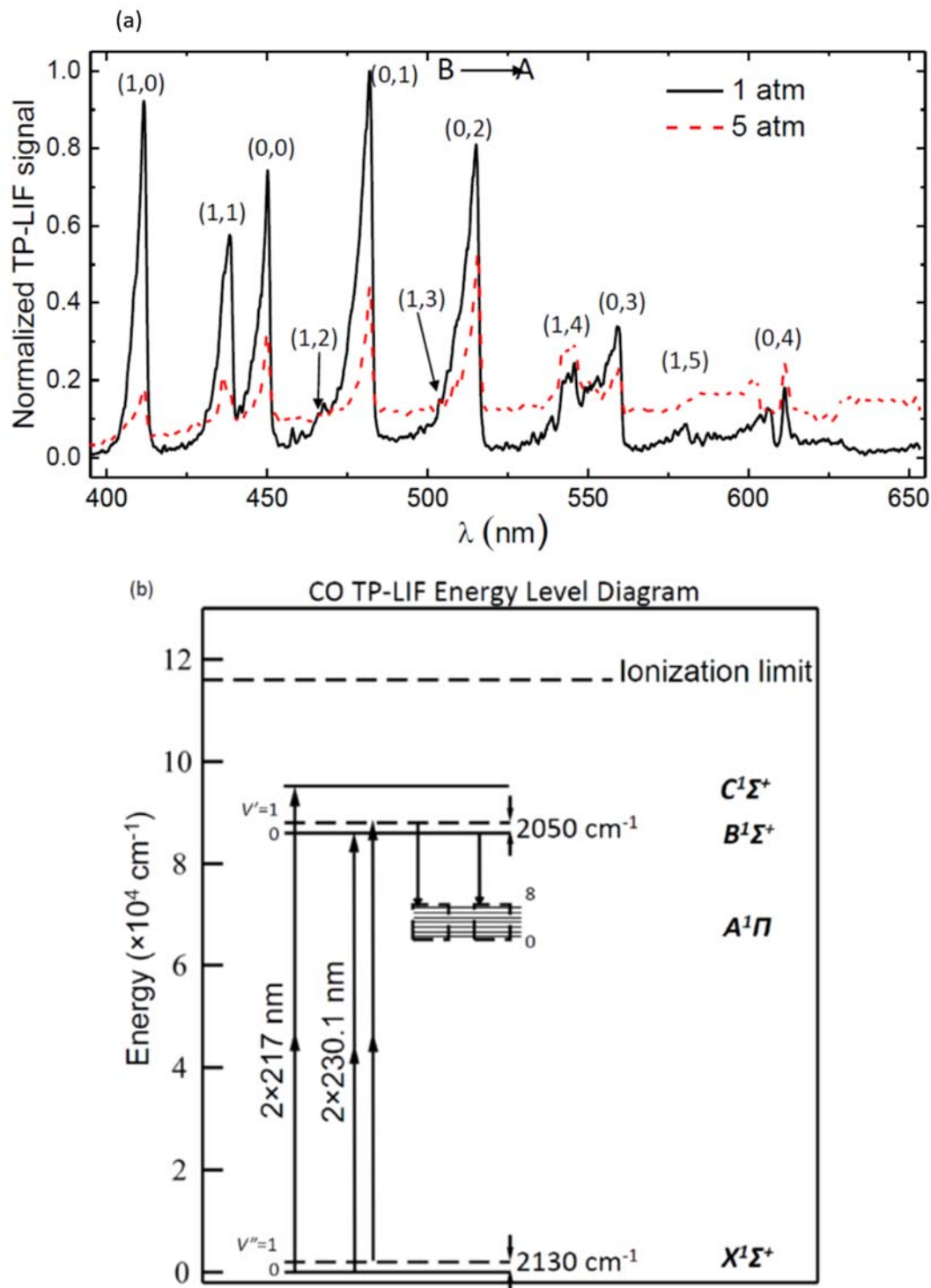


Figure 2.5 (a) CO fs TP-LIF emission spectra measured in a $\phi = 1.3$ CH₄-air flame. Laser irradiance was 2.3×10^{10} W/cm² (13 μ J/pulse). Both the 1 and 5 atm spectra were normalized by the peak signal at 1 atm near 483 nm. (b) Simplified energy level diagram indicating the (0-0) and (1-1) transitions in the $B^1\Sigma^+ \leftarrow X^1\Sigma^+$ system excited at 230.1 nm in this work.

2.3.5 Quantitative CO TP-LIF measurement at different pressures

To verify the quantitative nature of the measurements, a comparison was made between the theoretical equilibrium CO mole fractions and the CO fs TP-LIF signals averaged over 300 images and collected at various fuel-lean to fuel-rich equivalence ratios at 1 and 5 atm, as shown in Figure 2.6. It was found that the dependence of the CO mole fractions on equivalence ratio was in close agreement with the trends expected from equilibrium calculations from $\phi = 0.9$ (lower detection limit) to $\phi = 1.5$ at both 1 atm and 5 atm. This close agreement was achieved without corrections for the variation of quenching rates in the presence of different product species and collision partners. This implies that variations in the collisional quenching cross-sections with varying flame-product concentrations have little effect on the relative CO fs TP-LIF signals, allowing quantitative measurements with proper calibration using a flame with known CO concentrations. Support for the insensitivity to collisional quenching is found by plotting the theoretical quenching rate as a function of equivalence ratio based on published values [127] and equilibrium concentrations of various quenching species. As shown in Figure 2.7, the quenching rate varies by $\sim 7\%$ for equivalence ratios from 0.9 to 1.5. Hence, the CO mole fraction is a direct function of the CO signal over the entire equivalence ratio range investigated in this work.

In Figure 2.6b note that the slight discrepancy of $\sim 5\%$ at fuel-rich conditions and at higher pressure can be attributed, in part, to higher uncertainty caused by background chemiluminescence and fluorescence interferences from nearby molecular transitions, as shown previously in Figure 2.5a.

2.4 Conclusions

Fs TP-LIF was demonstrated for quantitative single-shot or kHz-rate measurements of the CO mole fraction at elevated pressures in a CH₄/air calibration burner. Various challenges that might be associated with the high-pressure flame measurements, such as background chemiluminescence, photolytic interferences, and multiphoton excitation and ionization, were addressed. It is suggested that the laser irradiance should not exceed 1.7×10^{10} W/cm² to avoid significant contributions from multiphoton de-excitation processes and potential photolytic interferences regardless of the pressure investigated in this work. Careful attention to the potential

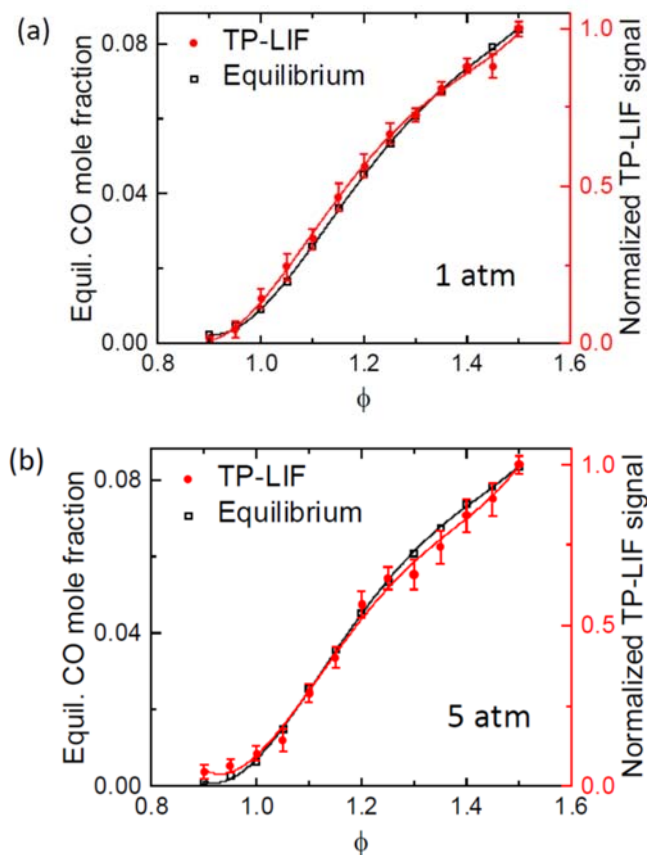


Figure 2.6 Comparison of CO mole fractions from equilibrium theory and experimental CO fs TP-LIF signals at various equivalence ratios for pressures of (a) 1 atm and (b) 5 atm. ICCD gate width is 15 ns. Error bars represent $\pm\sigma$.

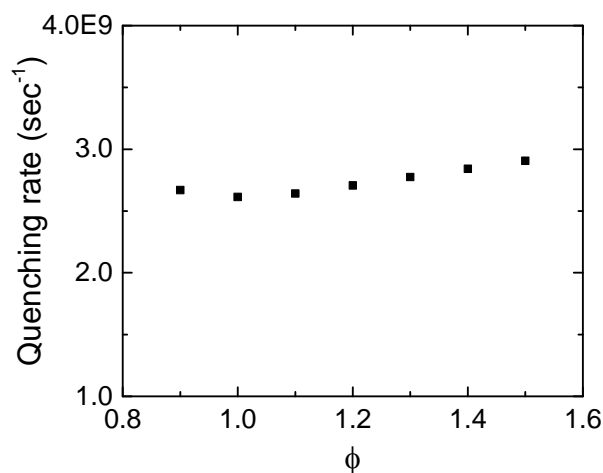


Figure 2.7 Theoretical quenching rates as a function of equivalence ratio assuming equilibrium concentrations of quenching species for the products of CH_4 -air combustion.

sources of interference allowed a very good match between the theoretical CO equilibrium mole-fraction predictions and the TP-LIF signal at different pressures and for varying equivalence ratios. This would enable quantitative measurement of absolute CO mole fractions with proper calibration. Dependence of the fs TP-LIF signal on pressure for line imaging, along with the relative merits of two different imaging systems, were also addressed to enable future investigations of unsteady, non-uniform flames.

3. PRESSURE-SCALING CHARACTERISTICS OF FEMTOSECOND, TWO- PHOTON LASER-INDUCED FLUORESCENCE OF CARBON MONOXIDE

Modified from a paper published in *Applied Optics* **58**, 7458-7465 (2019).

K. Arafat Rahman, Venkat Athmanathan, Mikhail N. Slipchenko, Terrence R. Meyer, and Suresh Roy

Broadband femtosecond (fs) two-photon laser-induced fluorescence (TP-LIF) of the $B^1\Sigma^+ \leftarrow \leftarrow X^1\Sigma^+$, Hopfield-Birge system of carbon monoxide (CO) is believed to have two major advantages compared to narrowband nanosecond (ns) excitation. It should (i) minimize the effects of pressure-dependent absorption line broadening and shifting, and (ii) produce pressure independent TP-LIF signals as the effect of increase in quenching due to molecular collisions is offset by the increase in number density. However, there is an observed nonlinear drop in the CO TP-LIF signal with increasing pressure. In this work, we systematically investigate the relative impact of potential de-excitation mechanisms, including collisional quenching, forward lasing, attenuation of the source laser by the test cell windows or by the gas media, and a 2+1 photoionization process. As expected, line broadening and collisional quenching play minor roles in the pressure-scaling behavior, but the CO fs TP-LIF signals deviate from theory primarily because of two major reasons. First, attenuation of the excitation laser at high pressures significantly reduces the laser irradiance available at the probe volume. Second, a 2+1 photoionization process becomes significant as the number density increases with pressure and acts as major de-excitation pathway. This work summarizes the phenomena and strategies that need to be considered for quantitative CO fs TP-LIF at high pressures.

3.1 Motivation

Revisiting Eq. 2.1, the fluorescence signal of CO fs TP-LIF can be expressed as

$$S_{TP-LIF} = CN_{CO} I_L^{m=2} \sigma \frac{A}{Q + A + P + \sigma_i I_L} \quad 3.1$$

As the spectral linewidth ($\sim 180 \text{ cm}^{-1}$) of the fs laser is significantly broader than the typical spectral linewidth of molecular transition ($< 0.2 \text{ cm}^{-1}$), the two-photon rate coefficient, σ , in Eq. 3.1 can be

expressed as a direct function of σ_0 and the spectral bandwidth of the excitation laser only [133], and can be assumed to be independent of pressure broadening or shifting. Since predissociation for CO is negligible and $A \ll Q$, then in the absence of photoionization Eq. 3.1 can be expressed as

$$S_{TP-LIF} \propto I_L^{m=2} N_{CO} / Q \quad 3.2$$

As the number density, N_{CO} , and quenching, Q , scale linearly with pressure (P), the fs CO TP-LIF signal should also be independent of pressure. Wang *et al.* recently reported further experiments of CO fs TP-LIF in a high-pressure non-reacting mixing chamber with the purpose of evaluating the pressure-scaling characteristics of the signal. They reported a strong nonlinear decay of the TP-LIF signal with pressure [140] and proposed several potential loss mechanisms such as collisional quenching, photoionization etc. However, they stopped short of quantifying the relative contributions of each mechanism and identifying the specific conditions under which these different mechanisms may be significant. For example, collisional quenching is proposed as a potential loss mechanism at higher pressures, although this is not consistent with theory. As such, a more detailed investigation is needed to determine which loss mechanisms are most important, which can be ignored, and what experimental parameters affect their behavior. In addition, Wang *et al.* used a laser irradiance that was two-orders-of-magnitude higher than that reported in the literature as the photoionization-free irradiance for atmospheric-pressure applications. As such, a third photon can be absorbed at the excited state and a 2+1 photon, resonance-enhanced transition is possible to the ionization continuum, which could potentially be one of the major perturbing sources in the measurement of fs CO TP-LIF. So, their conclusions about the pressure scaling of the TP-LIF signals are likely compounded by the effects of photoionization, which may have a different pressure dependence. Furthermore, such laser energies could cause potential nonlinear interactions at the test cell windows or other phenomena such as forward lasing that may impact the TP-LIF signals.

In the present study, therefore, a detailed imaging and spectroscopic investigation of CO fs TP-LIF is conducted at elevated pressure both at flame conditions and in a well-characterized, high-pressure mixing chamber. The magnitude of different potential loss mechanisms is quantified, and the impact of various experimental conditions on these loss mechanisms are thoroughly evaluated to enable more accurate CO TP-LIF measurements at high pressures.

3.2 Experimental Setup

The experimental setup consisted of a 1 kHz, 800-nm, 7.2 mJ/pulse regeneratively amplified Ti:Sapphire ultrafast laser source (Solstice Ace; Spectra Physics, Inc.) having 100-fs temporal pulsewidth. The fundamental beam at 800 nm was used to pump an optical parametric amplifier (OPA), which generated the TP-LIF excitation beam at 230.1-nm to excite multiple ro-vibrational transitions in the Hopfield-Birge system of CO. At this wavelength the OPA can produce ~ 50 $\mu\text{J/pulse}$ with a spectral bandwidth of ~ 180 cm^{-1} . This 230.1 nm beam was then guided into the probe volume via multiple dielectric mirrors and a combination of an $f = -1000$ mm cylindrical lens and an $f = +250$ mm spherical lens. One of the dielectric mirrors was replaced with a 90/10 beam splitter to monitor the input laser energy continuously during the experiment using a power meter (XLP12 head, Gentec). This optical setup produced a laser sheet that was 2.4 mm high and 200 μm thick at the probe volume. Two high-pressure devices were used in this work. First, a CH_4/Air flame was stabilized over a 25.4×25.4 mm Hencken calibration burner in a high-pressure test cell (as described in section 2.2). To minimize experimental uncertainties in the pressure scaling of the CO fs TP-LIF signal, an optically accessible gas sampling and mixing chamber rated up to 30 atm was used (Figure 3.1b). Images of the fluorescence signal from several CO emission bands were collected using an intensified charged-coupled device (ICCD) camera (PI-Max4-SB CCD, Princeton Instruments) with an 85-mm, $f/1.4$ camera lens in combination with a 20-mm extension tube to achieve high collection efficiency with high magnification for line imaging. A spectral filter with a 357–521 nm transmission window was used to minimize interference from background flame emission. The gate width in the intensifier was 15-ns. The mixing chamber had four 38.1 mm diameter UV fused silica windows (12.7 mm thickness) with a 203.2 mm path length in the direction of beam propagation. A 500-mm spectrometer with a 3600 g/mm grating (Acton SpectraPro 2500, Princeton Instruments) was used to spectrally resolve the transmitted 230.1 nm beam after two-photon excitation of CO. Images of CO fs TP-LIF were collected in the transverse direction via one of two mirrors located 50.8 mm from path of the beam. One of the windows in the transverse direction was replaced with a stainless-steel metal blank with electrical feed-through to facilitate two 25-mm brushless DC fans inside the mixing chamber. This was found to be critical to ensure proper mixing and minimize buoyancy effects on gas mixtures with large variations in density (such as He and CO). Proper mixing was verified by ensuring constant CO fs TP-LIF images over a period of 3 hours for a mixture of He and CO (94%:6% by vol.). Prior to each

measurement, the mixing chamber was purged multiple times with buffer gas and then filled with pure CO or a CO-buffer gas mixture based on the law of partial pressures. The pressure in the mixing chamber was monitored by a pressure transducer (GE UNIK 0-68 atm, ± 0.027 atm uncertainty) sampling at 1 kHz.

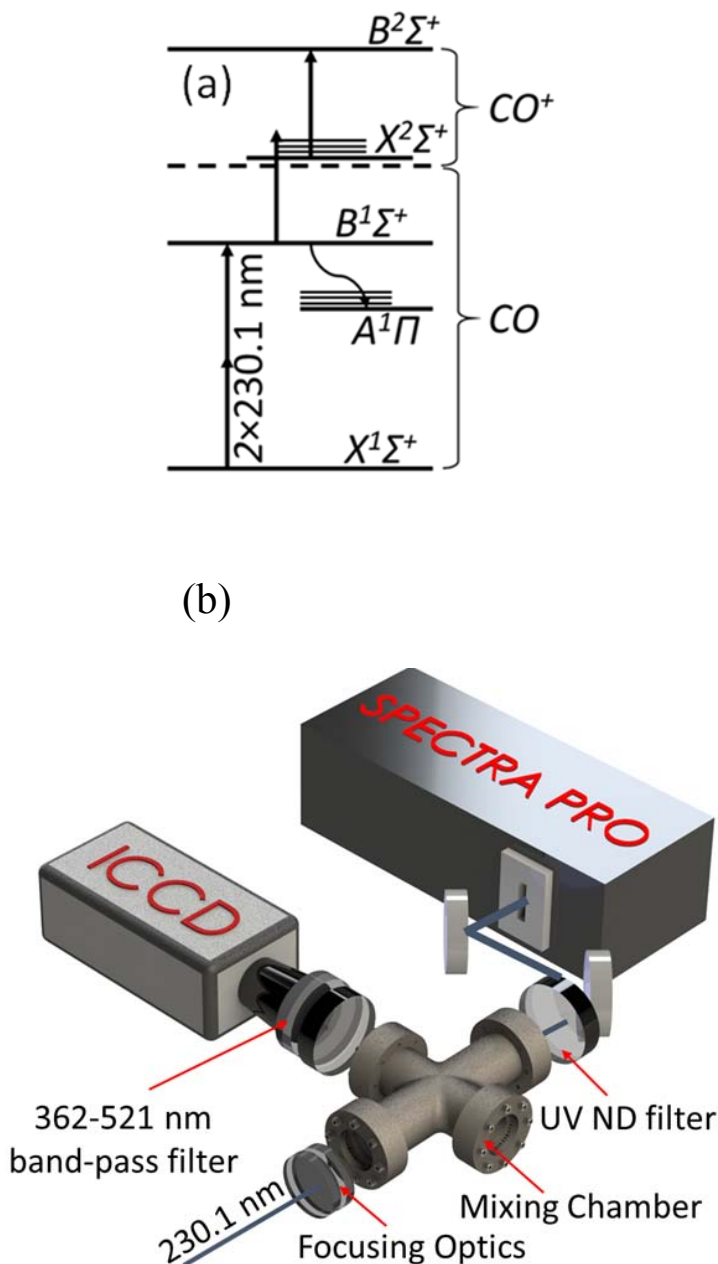


Figure 3.1 a) Simplified energy level diagram for CO fs TP-LIF showing the excitation at 230.1 nm. The dashed line represents the ionization potential, b) schematic diagram of the experimental set-up for CO fs TP-LIF in a mixing chamber.

3.3 Results and Discussion

3.3.1 Irradiance limitation at the window

Since the length of the mixing chamber is one-half that of the high-pressure combustion vessel in the direction of the beam propagation, the irradiance was much higher at the window using the same sheet forming optics as for the combustion vessel. As this can significantly affect the TP-LIF signal, the size of the beam should be optimized at the entrance window to avoid multiphoton absorption and degradation of the excitation laser beam. As shown in Figure 3.2 both the thickness of the window and the irradiance of the laser beam at the window influences the spectral broadening and the peak irradiance available at the probe volume. High irradiance at the window caused the laser beam spectrum to deviate from its Gaussian nature towards a top-hat profile. Hence for experiments in the mixing chamber, a $f = +150$ mm cylindrical lens was used. This optical setup produced a laser sheet that was 7 mm high and 120 μm thick at the probe volume, and the laser energy was adjusted to provide the same peak irradiance as the previous sheet forming optics. This arrangement reduced the irradiance at the window by factor of ~ 4 , thus minimizing the non-linear effects from the window.

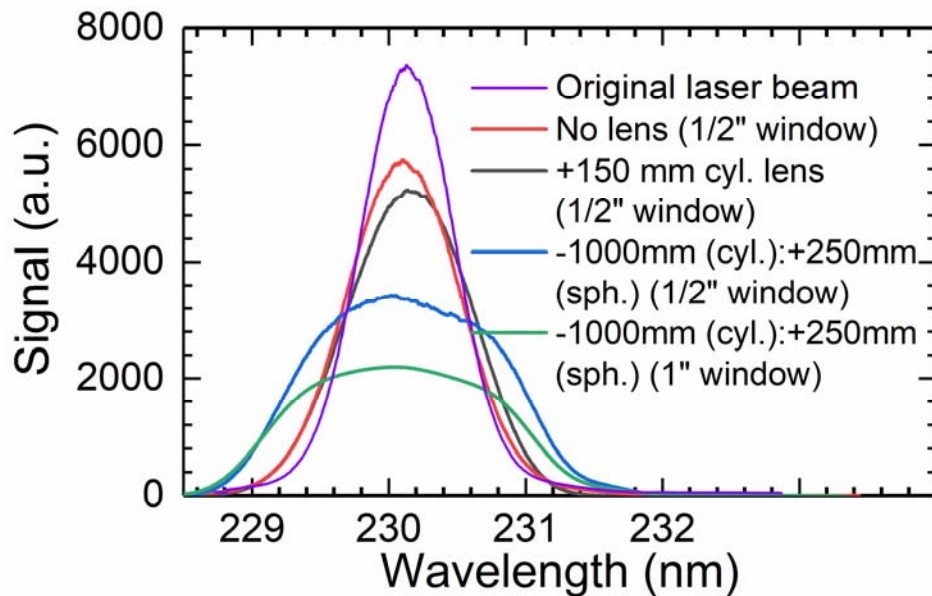


Figure 3.2 Trends showing the effects of multiphoton absorption and degradation of the UV excitation beam for different window transmission configurations.

3.3.2 Pressure scaling of CO fs TP-LIF

The dependence of CO fs TP-LIF signal on pressure was investigated both in a CH₄–Air Hencken burner flame for a fuel-rich equivalence ratio of $\Phi = 1.3$ (CO mole fraction 6%) and in a mixing chamber filled with various combinations of CO-buffer gas mixtures. At each pressure, 200 single-laser-shot TP-LIF images were collected and averaged. The background-corrected, normalized CO fs TP-LIF data are shown in Figure 3.3. The position of maximum signal shifted approximately 1.7 mm away from the focusing lens with an increase in pressure from 1 to 20 atm, likely caused by a change in refractive index of the gas media with increasing pressure. This variation in the location of maximum signal was accounted for by analyzing the data with a MATLAB script which finds the position of peak-signal for each dataset. Evaluation of the scaling of CO fs TP-LIF signal with pressure showed a strong decay even though the excitation irradiance was maintained at $\sim 1.7 \times 10^{10}$ W/cm², where photolytic interferences and perturbation due to photoionization were shown to be minimal at atmospheric conditions [33, 141]. The signal decreases by 90% in flame when the total pressure rises to 12 atm (see Figure 3.3a). A similar but slightly lower decay with pressure was observed in a mixture of 6% CO and 94% N₂ (See Figure 3.3b). In this case CO fs TP-LIF signal decreases by 90% as the pressure rises to 20 atm. The signal, however, decays at a much slower rate as the same experiment was conducted in a mixture of 2% CO and 98% N₂. Considering the effect of changing refracting index which would increase the beam waist with pressure, hence decrease the CO fs TP-LIF signal by virtue of I_L^2 dependency, the reduction in fs TP-LIF signal because of this reason can be calculated as less than 3% from 1 to 20 atm. And, could not explain the strong nonlinearity in the signal. To evaluate the source of this decay we systematically examined different perturbation mechanism that might contribute at higher pressures, as discussed in the following sections.

3.3.3 Effects of quenching

Variations of the CO fs TP-LIF signal as a function of pressure in different buffer gas mixtures was measured to investigate the effects of several colliding partners. 200 single-laser-shot images were collected at different pressures and for various pairs of collisional partners chosen from CO, CO₂, N₂, and He, and the average TP-LIF signals are shown in Figure 3.4. In the first case the chamber was filled with a mixture of CO (6 %) and He (94%), where helium has the

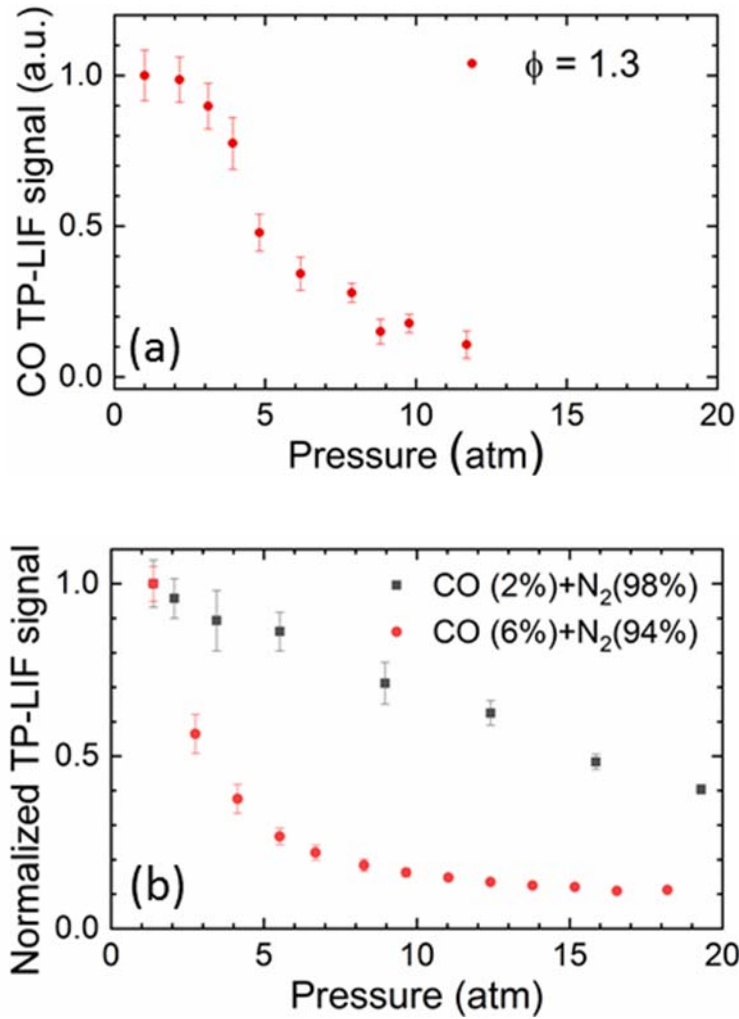


Figure 3.3 CO fs TP-LIF signal as a function of pressure in (a) $\Phi = 1.3$ CH₄-Air flame stabilized in a Hencken burner. (b) mixtures of CO and N₂. Laser irradiance was $\sim 1.7 \times 10^{10}$ W/cm² measured at 1 atm. Error bar represents $\pm \sigma$.

smallest quenching cross-section of the different quenchers. For the second case, the chamber was filled with CO (6%), CO₂ (5%), N₂ (65%), and He (24%). These mole fractions represent the corresponding mole fractions for CO, CO₂, and N₂ in a methane-air flame for $\Phi = 1.3$. It was found that irrespective of the quenchers the signal decays in a similar fashion (slightly slower for the CO+He case). However, the absolute signal levels in the case with CO+CO₂+N₂+He are an order of magnitude lower (red points in Figure 3.4). Settersten *et al.* reported species- and temperature-dependent cross-sections for the quenching of fluorescence from the $B^1\Sigma^+$ state of CO for all major quenchers [127]. Using the reported cross-section values of CO₂ and N₂, quenching corrections were applied to the TP-LIF signal for the mixture of CO+CO₂+N₂+He. The corrected signal

approximately matches the absolute signal for the case of CO+He (slight discrepancy can be attributed to uncertainty associated with the reported quenching cross-sections and instantaneous mole fraction of CO and different colliding partners for different experiments) but the corrections have no effect on the pressure-dependent decay of the signal. Given the theoretical expectation from Eq. 3.2 that the effects of increasing number density and quenching should make the CO TP-LIF signal independent of pressure, and the fact that quenching corrections do not alter the non-linear pressure dependence of the TP-LIF signal, a different explanation must be found for this non-linear dependence.

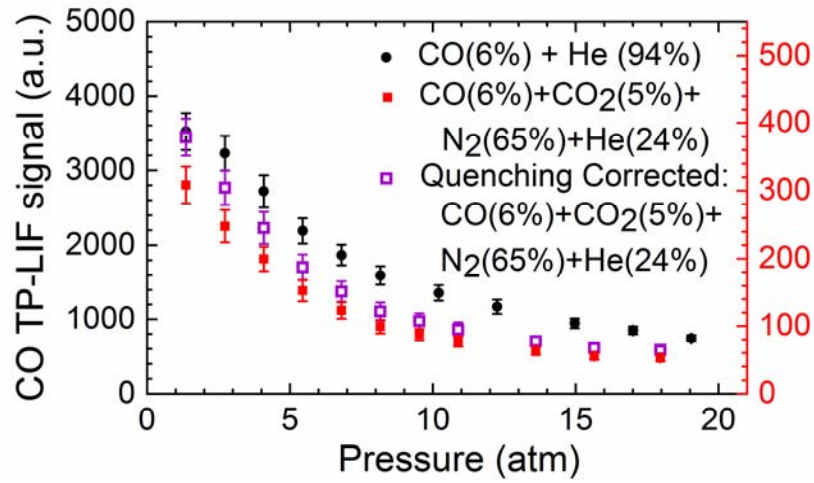


Figure 3.4 CO fs TP-LIF signal as a function of pressure in a mixing chamber for CO with different collision partners at a laser irradiance of $\sim 1.7 \times 10^{10}$ W/cm² at 1 atm. Quenching corrected data for the case of CO (6%), CO₂ (5%), N₂ (65%), and He (24%) use the same scale on the left as for the case of CO (6%) and He (94%). The uncorrected data use the scale on the right. Error bars represent $\pm \sigma$.

3.3.4 Forward lasing

Forward and backward lasing induced by two-photon laser excitation could act as a potential de-excitation pathway in the measurement of CO fs TP-LIF [120]. Recently fs two-photon-excited backward lasing was demonstrated for atomic hydrogen in an atmospheric-pressure flame [142]. In the presence of this de-excitation mechanism the signal in the direction of laser (*i.e.*, forward lasing + LIF) could be an order of magnitude higher than the signal transverse to the beam path (*i.e.*, only LIF). To investigate this effect, we collected images of the signal in both directions while the mixing chamber was filled with CO (6%) and N₂ (94%). The same collection optics were used for both measurements. A 266 nm long-pass filter was used to block the laser while imaging along

the laser path. As the point of view is different in the forward and transverse directions, the total signal collected in the camera sensor was used and shown in Figure 3.5. Very similar pressure scaling was found both in the forward and transverse directions, and the order of magnitudes of the signals are similar for various pressures. Slight discrepancies could be attributed to two image collection directions (line of sight vs. transverse imaging). Hence forward lasing at higher pressure could not explain the significant non-linear decay of CO fs TP-LIF signal with pressure.

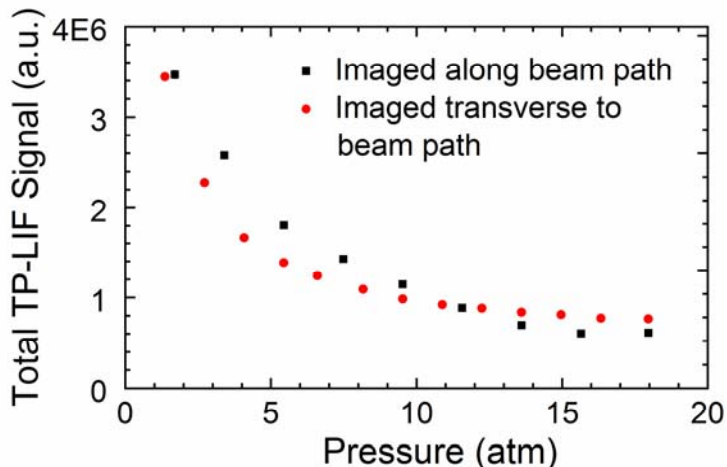


Figure 3.5 CO fs TP-LIF signal at varying pressure from two different point of imaging. In the presence of forward lasing, signal along the beam path is expected to be much higher than the signal transverse to the beam path. Total signal accumulated on the camera is plotted. Laser irradiance was $\sim 1.7 \times 10^{10} \text{ W/cm}^2$ at 1 atm.

3.3.5 Absorption of the excitation laser beam

Attenuation of the source laser by optical absorption from major species and scattering losses in high-pressure environments can reduce the transmission of UV light and the peak irradiance available at the probe volume. As it was not feasible to measure the laser energy directly at the focal volume in high-pressure experiments, a spectrometer was placed at the end of the mixing chamber and was used to measure the emitted unfocused UV beam spectrum with an ICCD.

Figure 3.6a shows the spectrometer trace of the unfocused transmitted UV beam used for excitation of CO fs TP-LIF at different pressures. 200 single-laser-shot spectra were collected, and averaged data are shown in the figure. The mixing chamber contained CO (6%) and N₂ (94%). The change in the area under the curve of this spectrum with pressure directly related to the losses in the mixing chamber, and when normalized with respect to the atmospheric data, can be used as

a measure of attenuation of the excitation laser in the test cell, and are shown in Figure 3.6b. It is clearly seen from the figure that as the pressure rises to 20 atm, almost 20% of the laser energy is attenuated. As the gas medium becomes increasingly opaque for UV radiation at high pressures, considerably less laser irradiance is available in the probe volume, and corrections would be needed to account for this effect.

This effect is exacerbated in flames where other major species such as CO₂, H₂O etc. can contribute significantly to this process. In a similar experiment (discussed in sub-section 4.3.6), it was found that almost 40% of the input energy is attenuated in an H₂/Air Hencken burner flame at a pressure of 10 atm [143]. Another reason for an increase in the attenuation of the UV beam at flame conditions is that the UV broadband absorption cross-section of major flame species such as CO₂ and H₂O can be an order of magnitude higher at high temperatures [144]. As described earlier in Eq. 3.1, the CO TP-LIF signals scale with I_L^2 , and as the irradiance available at the probe volume decreases with pressure, it will affect the TP-LIF signal nonlinearly. Hence, the nonlinear decay of the CO TP-LIF with pressure can be attributed, in part, to attenuation of the UV excitation laser irradiance with pressure, as shown in Figure 3.3. A correction factor for this effect would need to consider the path length through the flame and the local flame conditions. For the current non-reacting mixing chamber experiments, this effect accounts for only about 20% of the drop in the TP-LIF signal at 20 atm, and additional loss mechanisms are investigated, as discussed below.

3.3.6 Photoionization

As laser attenuation cannot explain entirely the nonlinear drop in the CO TP-LIF signal with pressure, additional spectroscopic investigation was conducted by collecting the spectra of the 230.1 nm beam with two-photon absorption (focused beam) and without two-photon absorption (unfocused beam). Figure 3.7a shows the spectrometer traces of the unfocused and focused 230.1 nm beams after passing through the mixing chamber with CO (6%) and N₂ (94%) at 1.4 atm. The laser irradiance at the probe volume was $\sim 1.7 \times 10^{10}$ W/cm² for the focused beam at atmospheric pressure. 200 single-laser-shot spectra were collected, and averaged data are presented in the figure.

In a two-photon absorption process, it is expected that different photon-pairs across the entire spectral bandwidth of the FTL fs excitation pulse would be absorbed by the probed molecule

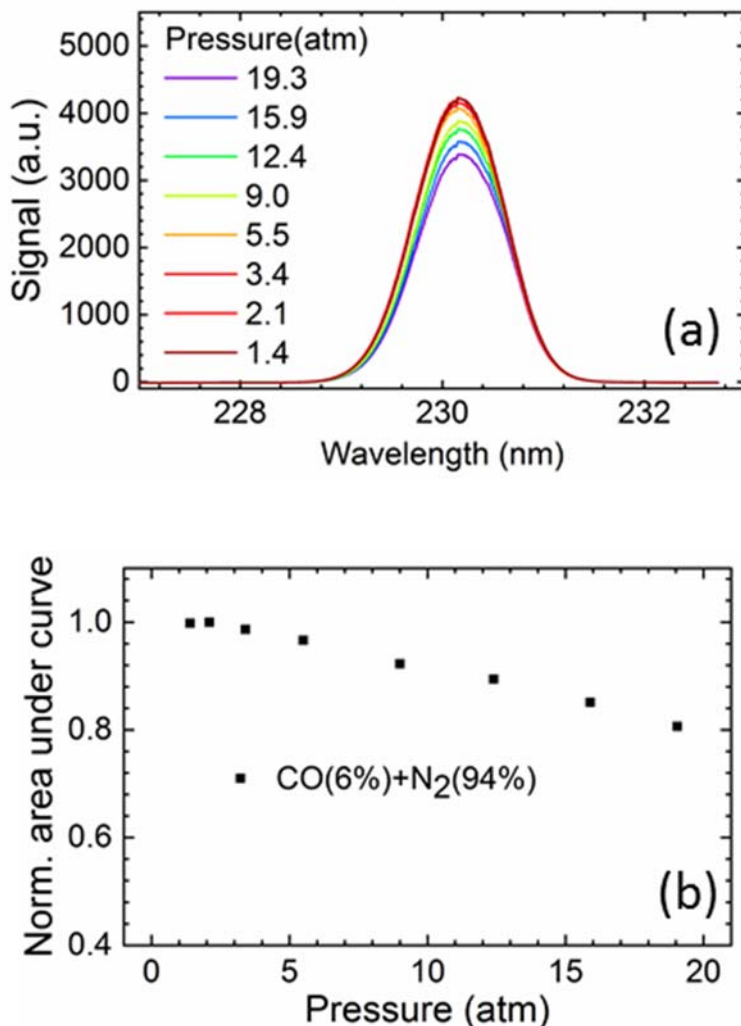


Figure 3.6 Attenuation of the UV laser in the mixing chamber at different pressures. (a) Spectra of the transmitted unfocused 230.1 nm beam from the mixing chamber filled with CO (6%) and N₂ (94%). (b) Normalized area under the curve. Almost 20% of the input energy is lost in the chamber as the pressure rises to 20 atm. For pressure scaling of CO fs TP-LIF signal, a correction factor was introduced from this experiment.

such that an absorption dip would not appear in the transmitted beam spectrum. This is the case near atmospheric pressure for the unfocused beam, but as shown in Figure 3.7a the transmitted beam spectrum is altered slightly for the case of a focused beam. This alteration of the transmitted focused beam spectrum is more apparent at higher pressures, as shown in Figure 3.7b, where distinctive single-photon absorption features appear near 230 nm (see dashed arrows). It is apparent that the intensities of these absorption features increase with pressure at a fixed CO mole fraction. However, at a fixed number density of CO (N_{CO}), the intensities of these feature are nearly

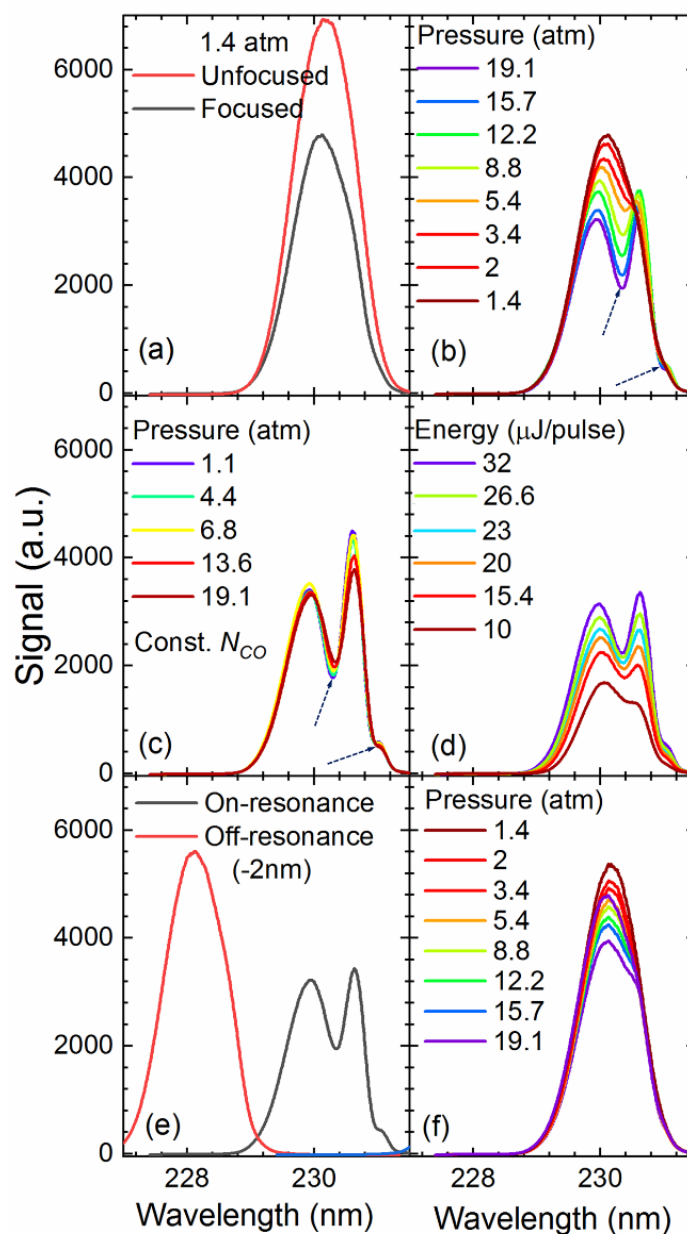


Figure 3.7 Spectra of transmitted 230.1 nm beam after two-photon absorption in the mixing chamber containing CO and N₂ at different conditions: (a) At atmospheric conditions approximately ideal two-photon absorption can be seen from the unfocused beam without two-photon absorption (red) and focused beam with two-photon absorption (grey). Laser irradiance of the focused beam was $\sim 1.7 \times 10^{10}$ W/cm² at 1 atm. (b) Varying pressure, fixed CO mole fraction of 6%. As the pressure increases certain absorption features can be seen in the spectrum. (c) Fixed N_{CO} , and varying pressure. The intensity of the features is independent of pressure. (d) Varying laser irradiance at 20 atm. Intensity of the feature increases with laser irradiance. (e) Detuning the laser off two-photon resonance eliminates this feature at any pressure (shown for 20 atm). (f) Transmitted focused beam at 2% CO, with perturbing absorption features nearly eliminated. Arrows indicate absorption features from a 2+1 photoionization process.

independent of pressure (Figure 3.7c). Figure 3.7d shows that as the laser irradiance goes up at a fixed pressure, the intensities of the absorption feature also go up. Detuning the laser to CO $B^1\Sigma^+ \leftarrow X^1\Sigma^+$ off-resonance eliminates the feature (Figure 3.7e). Moreover, by reducing the CO mole fraction from 6% to 2% with a balance of N₂, the presence of this perturbing effect is minimal even up to ~20 atm (see Figure 3.7f). This is consistent with the much slower decay of the CO fs TP-LIF signal with pressure for 2% CO versus 6% CO with a balance of N₂, as shown previously in Figure 3.3b. The spectral characteristics of these absorption features are consistent with the excited state CO undergoing $X^2\Sigma^+ \leftarrow B^1\Sigma^+$ 2+1 resonance-enhanced multiphoton ionization (REMPI), as shown in Figure 3.1a. Teodoro *et al.* even showed the possibility of a $B^2\Sigma^+ \leftarrow X^2\Sigma^+$ transition (see Figure 3.1a) of ground state CO⁺ by a doubly resonant pair of two-photon processes using a ps-laser [145]. Based on these observations, the presence of 2+1 photoionization was verified using a Rayleigh microwave scattering (RMS) technique [146, 147]. Nonetheless, it can be concluded that as the N_{CO} is increasing with pressure and the population of the excited electronic state increases, TP-LIF becomes more susceptible to perturbation by the 2+1 photoionization process. This addresses the second and potentially more significant cause of the nonlinear decay of CO fs TP-LIF with pressure. As such, careful experimental design is necessary to circumvent this perturbation mechanism so that this effect is minimized at high number densities.

3.3.7 Interference-minimized pressure scaling

Finally, the onset of photoionization was investigated by changing the laser energy and analyzing the transmitted 230.1 nm in a mixture of CO (6%) and N₂ (94%) (see Figure 3.8). The 2+1 photoionization feature was monitored for different laser irradiances. The solid line is the transmitted laser beam for a fluence of $\sim 6 \times 10^9$ W/cm² at 1 atm. The shape of this focused transmitted spectrum is identical for pressures up to 20 atm (dashed line in Figure 3.8) for the mixture of CO (6%) and N₂ (94%). Moreover, the data in Figure 3.9a at a fluence $\sim 6 \times 10^9$ W/cm² for 6% CO do not show a highly nonlinear drop in the CO fs TP-LIF signal with pressure up to 20 atm, which is in contrast with the case of $\sim 1.7 \times 10^{10}$ W/cm² shown previously in Figure 3.3b and as reported by Wang *et al.* [140]. However, the pressure scaling is similar between the high- and low-fluence cases in Figure 3.3b and Figure 3.9a, respectively.

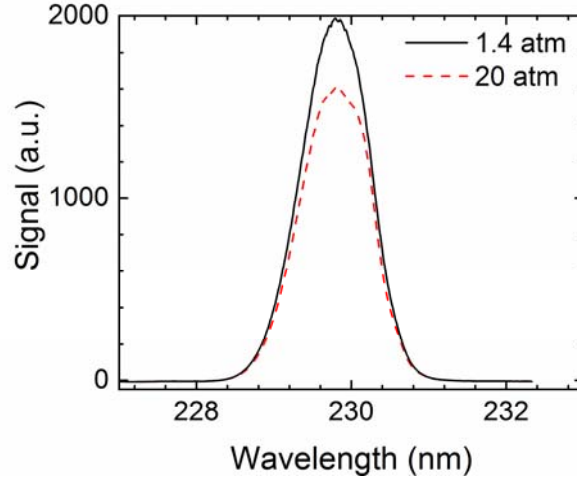


Figure 3.8 Spectra of transmitted 230.1 nm focused beam after two-photon absorption in the mixing chamber containing CO (6%) and N₂ (94%) measured at the upper limit atmospheric pressure laser irradiance of 6×10^9 W/cm². The 2+1 photoionization absorption feature is absent over the pressure range of 1–20 atm at this irradiance.

These trends are consistent with the loss mechanism due to 2+1 photoionization being minimized at lower fluence and at high CO concentrations. Applying a correction for attenuation of the UV light by the gas medium, it is found for the case of 6% CO that the corrected fs TP-LIF signal at 20 atm is still $\sim 25\%$ lower than that at atmospheric pressure (see Figure 3.9b), which implies that additional loss mechanisms are still present. One such loss mechanism was coined in sub-section 3.3.2 as the change in refractive index with pressure caused $\sim 3\%$ loss in TP-LIF signal from 1–20 atm. Moreover, we tuned the OPA to different CO $B^1\Sigma^+ \rightarrow A^1\Pi$ emission wavelengths and passed the beam through the mixing chamber filled with test gases to check for radiation trapping with pressure. It is estimated that the loss in the CO fs TP-LIF signal due to radiation trapping varies by less than $\sim 3\%$ from 1–20 atm. We can furthermore conclude that while some 2+1 photoionization may be present at low fluence, the spectral lineshape of the transmitted beam at 20 atm in Figure 3.8 implies that this effect is also relatively small. Based on the data in Figure 3.7a, however, it is clear that a correction for absorption using the unfocused beam does not account for the higher two-photon absorption and more severe reduction in the laser irradiance that would occur at the probe volume for the case of the focused beam. Unfortunately, the reported two-photon absorption cross-section in literature varies by 1–3 orders of magnitude [134, 148, 149], and there is little data available in this pressure range. Furthermore, the beam focusing characteristics would complicate a two-photon absorption correction even if the cross-sections are

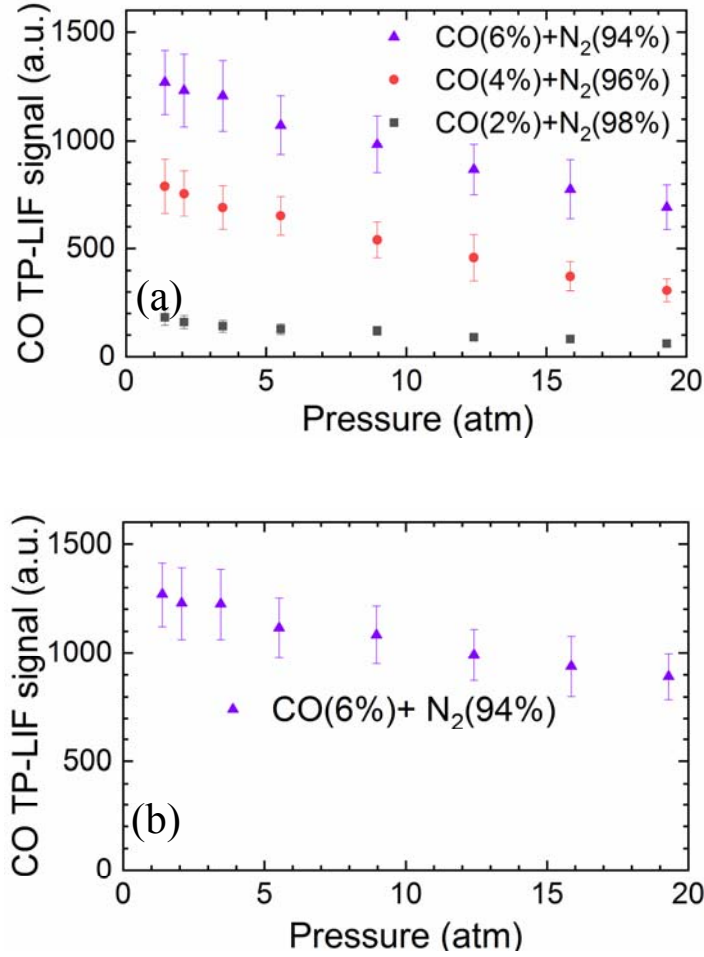


Figure 3.9 CO fs TP-LIF signal at various pressures and (a) varying CO mole fractions. (b) CO fs TP-LIF signal corrected for the actual irradiance available at the probe volume for a mixture of CO (6%) and N₂ (94%) as estimated from measurements of the transmitted laser energy. Laser irradiance at the probe volume was $\sim 6 \times 10^9$ W/cm² at atmospheric pressure.

known. Hence, the inability to measure the actual irradiance at the probe volume for the case of a focused beam at high pressure is a remaining source of uncertainty in the pressure scaling of CO fs TP-LIF and merits further investigation that is beyond the scope of this work.

3.4 Conclusions

In summary, potential loss mechanisms for CO fs TP-LIF were investigated for pressures from 1 to 20 atm to cover CO number densities that are relevant for practical high-pressure combustion systems. Initial measurements were conducted in a CH₄/Air calibration burner and a mixing chamber at elevated pressures, both showing a significant drop-in CO fs TP-LIF signals with

pressure. Detailed measurements were then conducted in the mixing chamber filled with different volume fractions of CO and other buffer gases.

After eliminating the effects of nonlinearities at the test cell windows, collisional quenching, and forward lasing, it was found that the nature of pressure scaling of the CO fs TP-LIF signal can be attributed primarily to two main factors. First, the attenuation of the source laser at high-pressure conditions can greatly reduce the actual laser irradiance available at the probe volume and, therefore, reduce the TP-LIF signal. Measuring the attenuation using an unfocused beam can partially correct for this drop-in irradiance at the probe volume, and further investigation is needed to understand the two-photon absorption process in a focused beam. Second, a 2+1 photon absorption-based photoionization process exacerbates the CO fs TP-LIF signal decay at elevated pressure. As the number density of probed species goes up with pressure, effects of photoionization that could be overlooked at atmospheric conditions can become significant at higher pressures due to this de-excitation pathway. Analyzing the spectrum of the transmitted beam after the two-photon excitation process is important for assessing the impact of 2+1 photoionization at various CO number densities and for varying laser irradiance. To avoid the contribution of 2+1 photoionization over the full range of experimental conditions, one should find the perturbation free input laser irradiance by analyzing the transmitted excitation beam at the highest number density to be attained in a given experiment (in this case at highest pressure) and using the same irradiance through the entire experiment. It is suggested that at a pressure of 20 atm, a temperature of 300 K, and with a CO mole fraction of 6%, the laser irradiance should not exceed $\sim 6 \times 10^9 \text{ W/cm}^2$ to avoid significant contributions from multiphoton loss mechanisms. At flame temperatures, lower number densities may allow higher laser irradiance to avoid 2+1 photoionization while ensuring sufficient signals using standard detection schemes.

4. QUANTITATIVE FEMTOSECOND, TWO-PHOTON LASER-INDUCED FLUORESCENCE OF ATOMIC OXYGEN IN HIGH-PRESSURE FLAMES

Modified from a paper published in *Applied Optics* **58**, 1984-1990 (2019).

K. Arafat Rahman, Venkat Athmanathan, Mikhail N. Slipchenko, Sukesh Roy, Zhili Zhang, and Terrence R. Meyer

Quantitative femtosecond two-photon laser-induced fluorescence of atomic oxygen was demonstrated in an H₂/Air flame at pressures up to 10 atm. Femtosecond excitation at 226.1 nm was used to pump the $3p^3P_{J'=0,1,2} \leftarrow 2p^3P_{J''=0,1,2}$ electronic transition of atomic oxygen. Contributions from multiphoton de-excitation, production of atomic oxygen and photolytic interferences were investigated and minimized by limiting the laser irradiance to $\sim 10^{11}$ W/cm². Quantitative agreement was achieved with the theoretical equilibrium mole fraction of atomic oxygen over a wide range of fuel-air ratios and pressures in an H₂/Air laminar calibration burner.

4.1 Introduction

The measurement of highly reactive radical species is of fundamental importance since they play critical role in flame and plasma chemistry [150, 151]. Atomic oxygen (O) is particularly important as it is a key intermediate species in chain-branching reactions [152], nitric oxide (NO) formation [153], and plasma energy transfer processes [154, 155]. Quantitative measurements of atomic oxygen in flames at elevated pressures are important for developing a better understanding of combustion processes at relevant operating conditions.

Raman spectroscopy [156] and Coherent anti-Stokes Raman scattering (CARS) [157] have been used for measurement of atomic oxygen in flames with a detection limit of 1%. However, sensitivity limits and spectral interferences have prevented further development of these techniques for atomic flame species detection. Radar resonance enhance multi-photon ionization (REMPI) has been successfully applied in flames for measurement of absolute atomic oxygen concentrations, although disagreement with equilibrium predictions at fuel lean and rich conditions resulted from susceptibility to background ionization and photolytic interferences [158].

The most commonly used scheme for two-photon transitions of the ground electronic state of O involves excitation at 226 nm of $3p^3P_{J'=0,1,2} \leftarrow \leftarrow 2p^3P_{J''=0,1,2}$, followed by fluorescence at 845 nm from $3p^3P_{J'=0,1,2} \rightarrow 3s^3S$ decay. The simplified energy level diagram for this scheme is shown in Figure 4.1.

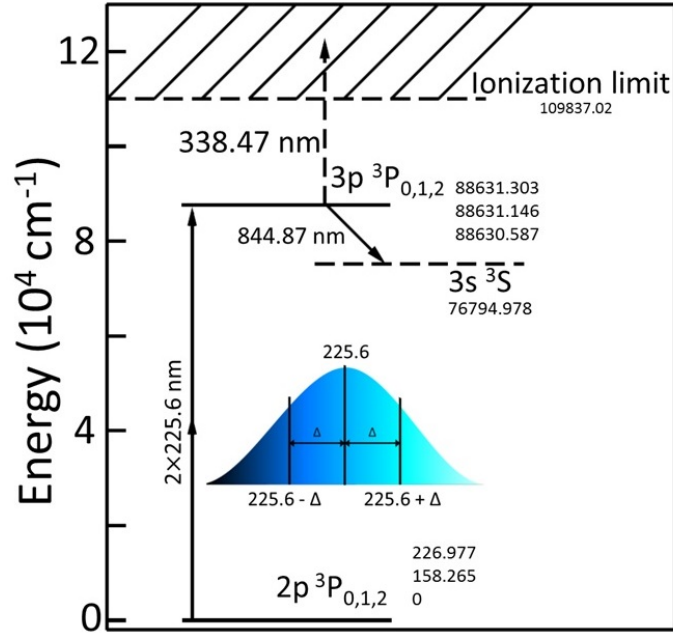


Figure 4.1 Energy level diagram of the $3p^3P_{J'=0,1,2} \leftarrow \leftarrow 2p^3P_{J''=0,1,2}$ atomic oxygen transition excited at 226 nm. Inset shows multiple in-phase photon-pairs in the broadband fs excitation pulse contributing to the resonant transition.

In this work, we investigate the use of fs TP-LIF for quantitative measurement of O atoms in a high-pressure calibration flame with known equilibrium mole fractions. The inherently lower equilibrium number density of O atoms at high-pressures and spatial constraints on collection optics in windowed test rigs limit signal levels relative to the substantial increase in background flame luminosity. Meanwhile, potential interferences limit the laser excitation energies that can be delivered to the probe volume. The high irradiance of fs pulses can cause several known de-excitation mechanisms of the excited state or trigger laser induced generation of O atoms in the flame, which could prevent quantitative accuracy over the full range of conditions. The main interference sources for fs O-atom TP-LIF are: (1) 2+1 photoionization of the excited-state O atom [159], (2) laser generated O atoms from O_2 and CO_2 [160, 161], (3) rapid predissociation to O

atoms after single-photon excitation of O₂ Schumann-Runge bands [162], and (4) stimulated emission [142, 163].

In this work we explored multiple strategies to circumvent the aforementioned interference sources and achieve quantitative accuracy at high-pressure flame conditions over a range of fuel-air ratios. A steady laminar H₂/Air calibration flame was operated in a windowed pressure vessel to enable comparisons with known equilibrium O-atom mole fractions. Furthermore, we investigated the dependence on laser wavelength, irradiance, and quenching rates at pressures up to 10 atm, where the background flame luminosity increases significantly.

4.2 Experimental Apparatus

A regeneratively amplified Ti:sapphire laser system (Solstice Ace; Spectra Physics, Inc.) was used as the fs-laser source. The 7.2-mJ/pulse output of the laser at 800 nm and 1 kHz repetition rate with a pulsewidth of 100 fs full-width at half-maximum (FWHM) was then split into two beams of 4.3 mJ and 2.9 mJ. An optical parametric amplifier (OPA) was pumped by the 4.3 mJ beam, which produces a signal beam at 1259.33 nm (TOPAS Prime; Coherent, Inc). The 1259.33 nm output of the OPA was then frequency doubled twice to convert the beam to 314.83 nm (NirUVs; Coherent, Inc), followed by sum-frequency mixing of the 314.83 nm beam with the fundamental 800 nm beam to produce 40 μ J/pulse at 226 nm. Multiple 45° dielectric mirrors were then used to eliminate the residual energy from the OPA and to route the 226 nm beam to the high-pressure combustion test rig (see Figure 4.2). One of the dielectric mirrors was replaced by a 50/50 beam splitter, and the transmitted beam was monitored continuously to check for the fluctuation of laser irradiance during the experiments. A +300 mm spherical lens was used to focus the beam into the high-pressure combustion chamber, producing a focal volume of \sim 230 μ m diameter and \sim 2.5 mm length to excite $3p^3P \leftarrow \leftarrow 2p^3P$ two-photon transitions of atomic oxygen. Optical access to the test rig was provided through three 25.4 mm UV-fused silica windows (Corning 7979) purged by N₂ to prevent water condensation. The size of the beam at the entrance of the window and the window material were optimally chosen to minimize multiphoton absorption and degradation of the high peak irradiance fs-laser pulse at the window. A premixed H₂/Air flame was stabilized over a 25.4 \times 25.4 mm Hencken calibration burner, which produced a steady, laminar flow of nearly adiabatic equilibrium flame products over a wide range of equivalence ratios (ϕ) [137, 138]. Two 50 mm diameter spectral filters were used in combination (Semrock FF01-840/12 and FF01-850/10) with

an effective transmission window of 2 nm (>93% transmission) to spectrally separate the $3p^3P \rightarrow 3s^3S$ fluorescence signal at 845 nm. The fluorescence images were recorded by the combination of an image intensifier (IRO; LaVision GmbH) and EMCCD camera (Newton 970; Andor Tech.) to enable high efficiency single-laser-shot and averaged detection of O fs TP-LIF signal. The collection optics were comprised of an uncoated +60 mm focal length spherical lens (placed inside the pressure vessel to maximize the collection angle) and an 85 mm, $f/1.4$ Nikon camera lens arranged in a conjugate configuration to collect and focus the fluorescence signal onto the intensifier. The introduction of collection optics inside the test rig instead of using the camera lens alone enabled a factor of two increase in signal-noise-ratio (SNR). Images were collected at 10 mm above the burner surface.

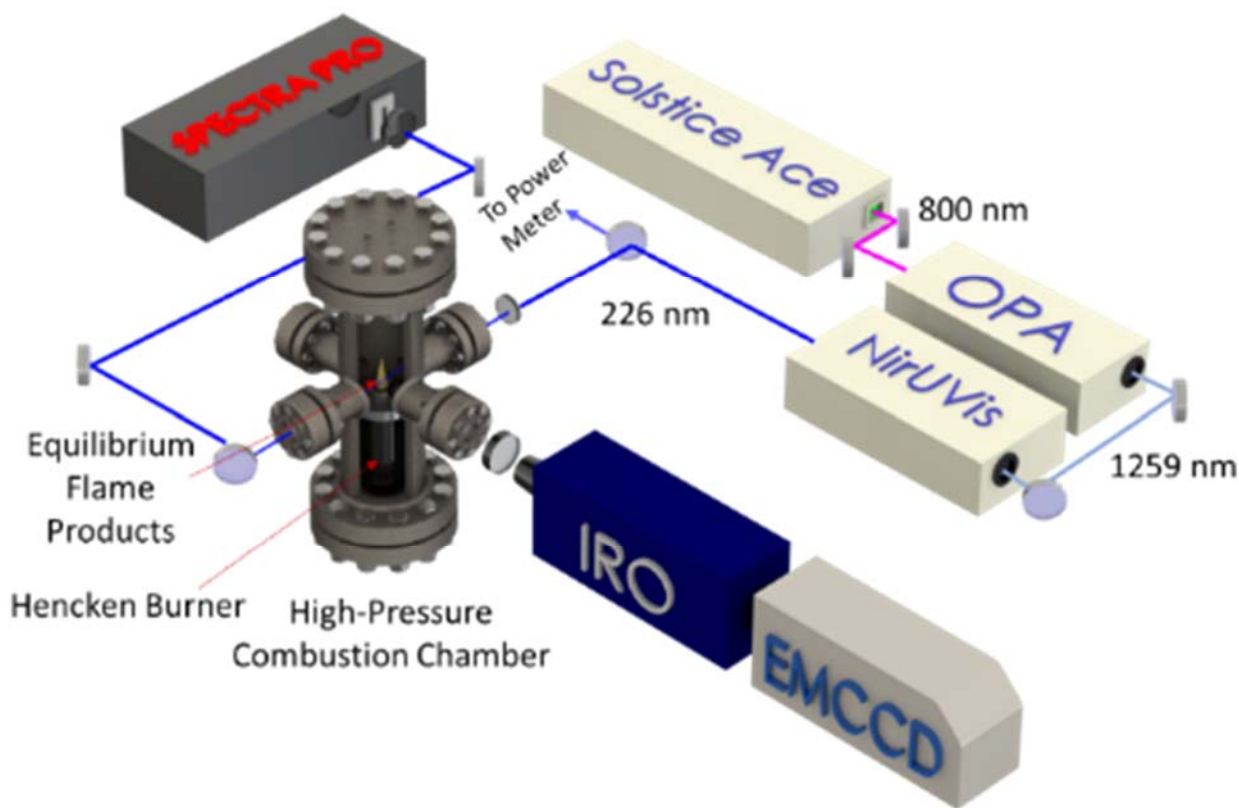


Figure 4.2 Experimental setup of the fs laser, spectrometer, and imaging system for atomic O fs TP-LIF.

The fluorescence signal for O fs TP-LIF can be expressed as

$$S_{TP-LIF} = CN_o \sigma^{(2)} \frac{A_{23}}{Q_2 + A_2 + P + \sigma_i I_L} \iint (I_L(t, \vec{r}) / h\nu)^2 dt dV \quad 4.1$$

where C includes all experimental constants for calculating fluorescence collection efficiency; N_o is the number density of atomic oxygen in ground electronic state; $\sigma^{(2)}$ represents two-photon absorption cross section [164]; A_{23} is the spontaneous emission rate of the excited electronic state (State 2 in Figure 4.1); A_2 is total spontaneous emission rate of excited electronic state [165]; P is the predissociation rate; σ_i is the photoionization cross section [164]; Q_2 is the quenching rate [166, 167]; $h\nu$ is the photon energy of the laser; I_L is the laser irradiance; and V is the detection volume.

4.3 Results and Discussion

4.3.1 Effects of excitation wavelength

The dependence of atomic oxygen fs TP-LIF signal on excitation wavelength was investigated by scanning the OPA near $3p^3P_{J'=0,1,2} \leftarrow 2p^3P_{J''=0,1,2}$ transition at two different pressures (1 and 5 atm) in the H₂/Air Hencken burner flame at $\phi = 0.95$. An intensifier gain of 60% with 100 ns gate and EM gain of 70% were used. 700 shots were accumulated on the imaging system and a set 100 such images were collected at each wavelength, with the normalized TP-LIF signal shown in Figure 4.3. Note that the bandwidth of the excitation pulse at 1 and 5 atm pressure was found to be 1.05 and 1.01 nm FWHM respectively. The lower $2p^3P_J$ and upper $3p^3P_J$ states of atomic oxygen are divided into three levels with orbital angular quantum number $J = 0, 1, 2$ [168]. The upper levels spacing are much closer than the laser bandwidth, but the lower states have an energy spacing (see Figure 4.3) corresponding to $J' \leftarrow J''$ TP-LIF excitation wavelengths of 225.655 nm (0-0), 226.058 nm(1-1), and 226.233 nm (2-2). At flame temperatures, more than 90% of the ground level atomic oxygen population resides in the $J'' = 1, 2$ states [160]. Hence, the TP-LIF signal at both pressures peaks near 226.1 nm implying more efficient excitation of the $J'' = 1, 2$ states. From Figure 4.3, it is also evident that the effects of pressure dependent absorption line broadening and shifting, major challenges for ns-laser excitation [169], are minimized by the transform-limited nature of the broadband fs pulse.

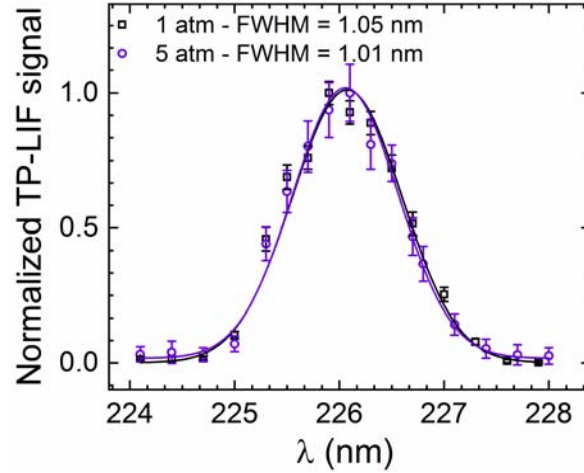


Figure 4.3 Atomic oxygen TP-LIF signal dependence on the laser excitation wavelength at 1 and 5 atm showing normalized experimental data (symbols) with a Gaussian fit (line) at 1 and 5 atm. Laser energy was 5 $\mu\text{J}/\text{pulse}$. Error bars represent $\pm\sigma$.

4.3.2 Dependence of o fs TP-LIF signal on laser irradiance

In the absence of any perturbing effects, the TP-LIF signal should follow a quadratic relationship with the laser irradiance ($S_{TP-LIF} \propto I_L^{m=2}$), as evident from Eq. 4.1. However, photolysis and 2+1 photon-ionization can significantly perturb the fs O-atom TP-LIF signal by photochemical production of O atoms and ionization of the excited-state population. The former leads to irradiance dependency with $m > 2$, while the latter causes the signal to increase less rapidly with laser irradiance, causing an exponent $m < 2$. As such, dependency of the O-atom TP-LIF signal on laser irradiance was investigated at two deferent pressures (1 and 5 atm) at the same equivalence ratio of $\phi = 0.95$, as described above. The laser was tuned to 226.1 nm since the O-atom fs TP-LIF signal maximizes at this wavelength. Three sets of 200 single-shot images were recorded. At this condition the O-atom mole fraction in the flame is about 610 and 310 ppm for 1 and 5 atm, respectively. The background-corrected, averaged signal and error bars (based on $\pm\sigma$) are shown in Figure 4.4. Near quadratic dependence was found up to 5 $\mu\text{J}/\text{pulse}$ ($\sim 10^{11} \text{ W}/\text{cm}^2$) at 1 atm (within 6%) and 5 atm (within 3%), which is a necessary condition to ensure that the fluorescence signal is collected within the limits of validation of Eq. 4.1. Note that at this irradiance and O atom number density the effects of stimulated emission are also negligible [31, 142] and were not investigated as a perturbing source. This near quadratic dependence does not guarantee a completely interference-free measurement, as under certain experimental conditions different

interfering mechanisms (both single and multiphoton processes) can occur simultaneously in an opposing manner, resulting in a quadratic dependence of the signal. Thus, additional strategies are required to ensure the absence of all perturbing effects, as discussed below.

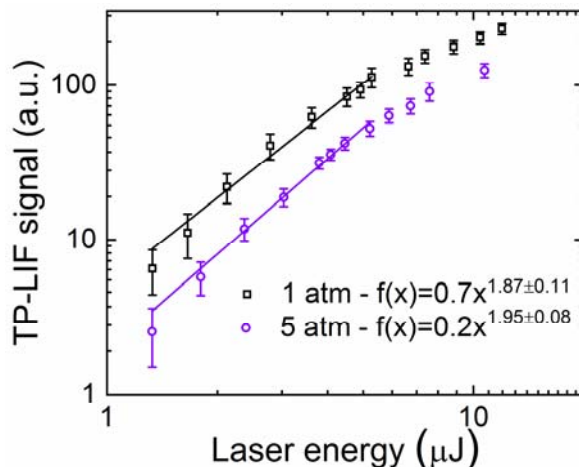


Figure 4.4 Atomic oxygen TP-LIF signal dependence on the excitation laser energy at 1 and 5 atm. 5 $\mu\text{J}/\text{pulse}$ corresponds to an irradiance of $\sim 10^{11} \text{ W}/\text{cm}^2$. Error bars represent $\pm\sigma$.

4.3.3 Interferences from O_2

As CO_2 and O_2 are the main two sources of photolytic production of O atoms in flames, they warrant careful investigation to determine their influence on the feasibility of quantitative measurements, especially at elevated pressures where the number density of perturbing sources increases. The effect of photolytically produced atomic oxygen from CO_2 has been addressed in recent publications [31, 33, 141] and beyond the scope of this paper. As mentioned earlier, photolytic production of atomic oxygen from O_2 mainly stems from two major sources. (1) A laser generated plasma in the probe volume can enhance the dissociation of O_2 by electrons [170] and (2) thermally excited vibrational levels ($v'' > 0$) in ground electronic states of O_2 can undergo single-photon transition at 226 nm in the Schumann-Runge bands followed by rapid predissociation to produce O atoms in the flame [162]. At room temperature the latter cannot be measured [161] and is discussed in the next section. To investigate the laser generated O atoms that are contributing to the fs TP-LIF signal, we filled the test rig with 100% O_2 and observed the O-atom fs TP-LIF signal in the probe volume. The data based on 3 sets of 200 single-shot images are shown in Figure 4.5. As collection optics and detection system used here were the same as in Figure 4.4, a comparison can be made to determine the relative contribution of this effect to the overall O-atom TP-LIF

signal in a flame. With a O_2 mole fraction of 1% at $\phi = 0.95$ and lower density at flame temperatures, we conclude that laser-generated O-atoms by the creation of plasma constitutes less than 1% of the total TP-LIF signal at the reported photoionization-free irradiance $\sim 10^{11} \text{ W/cm}^2$, which is well within the measurement uncertainty.

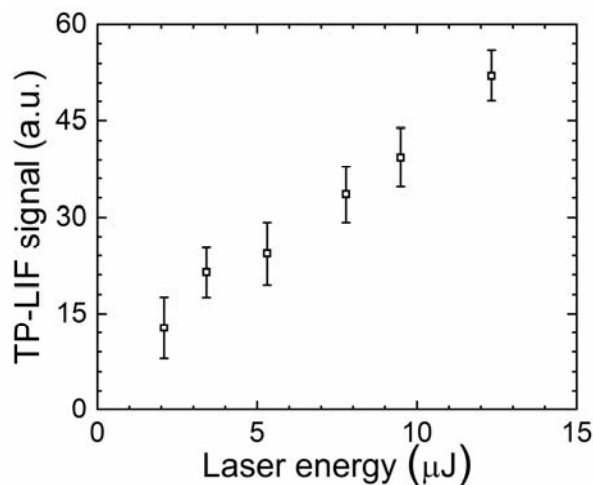


Figure 4.5 O-atom fs TP-LIF signal originating from 100% O_2 at room temperature. Based on signal levels for 1% O_2 mole fractions in Figure 4.4, laser generated O atoms from O_2 account for much less than 1% of the TP-LIF signal in a $\phi = 0.95$ flame.

4.3.4 Quantitative O-atom fs TP-LIF measurement

To assess the effect of other potential interferences on O-atom fs TP-LIF, from photodissociation or other photochemical effects at elevated pressures, such as single-photon excitation of O-atoms at flame temperatures, de-excitation by collisional quenching by other equilibrium products, etc., a comparison was made between the theoretical equilibrium mole fractions in the calibration burner and O-atom fs TP-LIF signals for a range of equivalence ratios. 700 shots were accumulated on the imaging system and 100 accumulated images were recorded at various fuel-lean to fuel-rich equivalence ratios at 1, 3, and 5 atm. The averaged results for 1 and 5 atm are shown in Figure 4.6(a-b). It can be seen from these figures that the dependence of the O-atom fs TP-LIF signal is in close agreement with the trends expected from theoretical calculations from the NASA CEA chemical equilibrium code [171] for a range of equivalence ratios and pressures. Note that excess O-atoms that would originate from the excited molecular oxygen in Schumann-Runge bands, as described in the previous sub-section, would result in a discrepancy that is most apparent at fuel-lean conditions. As this discrepancy of $\sim 5\%$ at lean conditions are close to the experimental

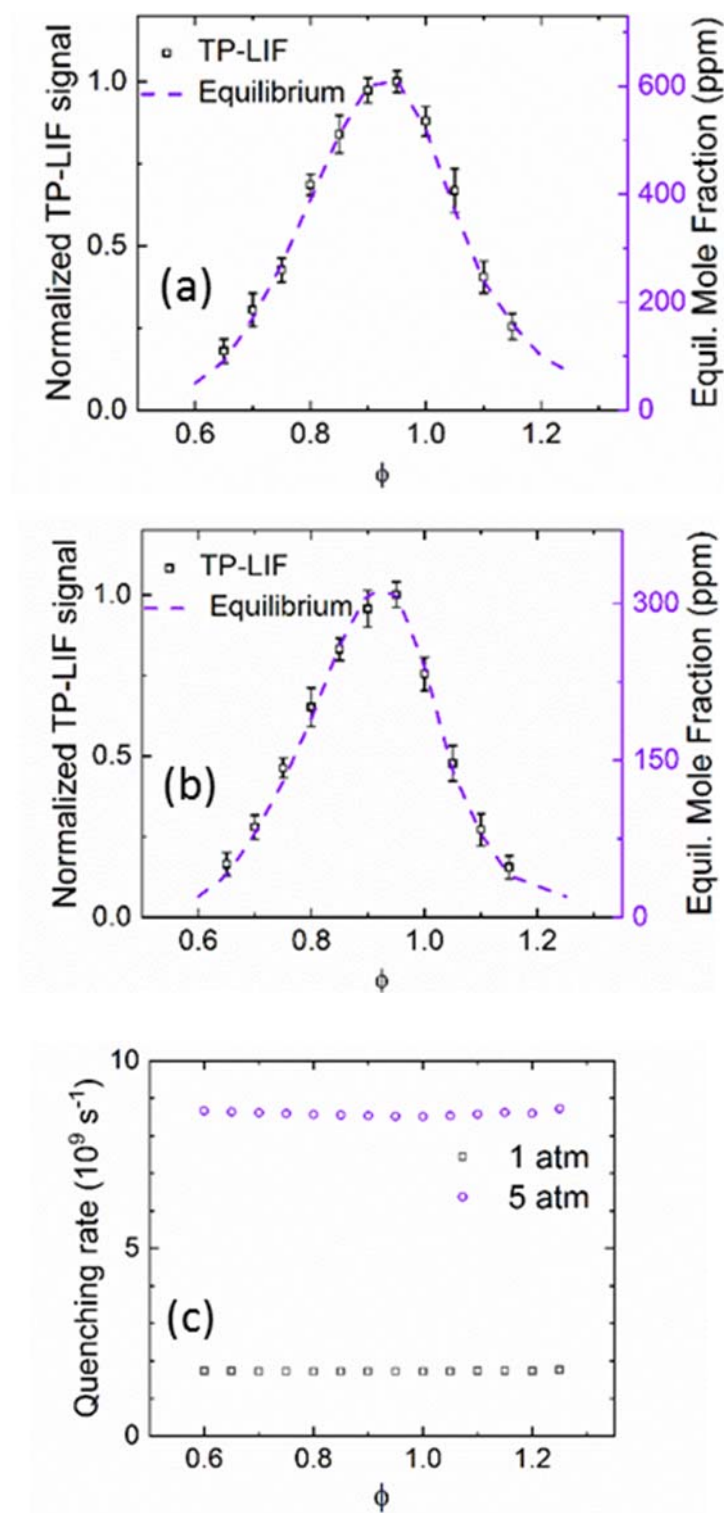


Figure 4.6 Comparison of O mole fractions from equilibrium theory and experimental O-atom fs TP-LIF signals at various equivalence ratios for pressures of (a) 1 atm and (b) 5 atm in H₂/Air Hencken burner flame products. Laser energy was 5 $\mu\text{J}/\text{pulse}$ in probe volume. Error bars represent $\pm\sigma$. (c) Theoretical quenching rates as a function of equivalence ratio assuming equilibrium concentrations of major quenching species of the products of H₂/Air combustion.

uncertainty at low and high pressures, this source of interference is relatively minor. This close match was achieved without corrections for species-dependent quenching rates. This implies that the variation of collisional quenching rates with changing flame product species mole fractions, pressure, and temperature have minimal effects on the relative O-atom fs TP-LIF signals. Hence, quantitative measurement of atomic oxygen by fs TP-LIF is possible by proper calibration of the signal with a flame with known O-atom concentration, as done in this current work. To support this argument, the quenching rate (Q) for atomic oxygen was calculated using collisional cross-section data available in literature [164, 166, 168]. Note that these quenching cross-sections were measured at room temperature, and limited empirical data are available at flame temperatures [172]. Frank *et al.* reported a $1/T$ dependence of quenching cross sections on temperature in measurements of O-atom TP-LIF in a Bunsen flame and achieved good agreement with experimental results [167]. These quenching cross sections and $1/T$ dependence were used to compute the quenching rates shown in Figure 4.6c. As shown the figure, the quenching rate varies within $\sim 3\%$ at both 1 and 5 atm over an equivalence ratio range from 0.6 to 1.25. This indicates that the O-atom mole fraction is a direct function of the O-atom fs TP-LIF signal over the entire equivalence ratio range investigated in this work.

4.3.5 O fs TP-LIF images at high pressure

Figure 4.7 shows 700 shots accumulated and single-shot images of O fs TP-LIF at different pressures in the H₂-Air Hencken burner flame at $\phi = 0.95$ using the same $5 \mu\text{J/pulse}$ ($\sim 10^{11} \text{ W/cm}^2$) laser irradiance. The non-uniformity of CH₄-air Hencken burner flames at higher (5-10 atm) pressures was described in a previous article discussing CO fs TP-LIF [141]. Due to the much higher (~ 5 times) mass-diffusivity of H₂ than CH₄, a relatively uniform flame was stabilized in the Hencken burner even up to 10 atm in this study. Rather, the major challenge for high-pressure fs TP-LIF measurements arise from the increasingly luminous background of the flame, which in turn reduces the signal-to-noise-ratio (SNR) dramatically. Beam steering was also observed with increasing pressure, which is of concern in locating the probe volume in turbulent flames. This should not affect the current measurements because of the uniformity of the Hencken burner combustion products. The maximum SNR achieved in the current measurements was 11 and is an improvement over recent O-atom fs TP-LIF measurements at atmospheric pressure [31]. The SNR reaches the single-shot detection limit at 6 atm. The improved SNR over prior work can be

attributed to the combined use of an intensifier and EMCCD, with further improvements possible using a more sensitive intensifier. The corresponding single-laser-shot detection limit was ~50, 90, 300 ppm at 1, 3 and 6 atm respectively.

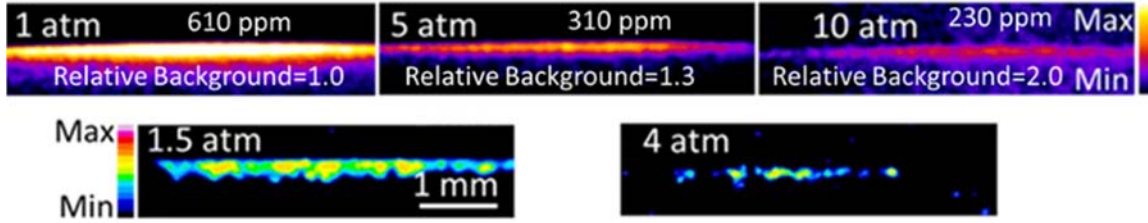


Figure 4.7 Accumulation of 700 shots (upper row) and single-shot (lower row) O-atom fs TP-LIF signals at various pressures. The main flow exit of the Hencken burner was 25.4×25.4 mm. Laser beam was approximately 10 mm above the burner surface. Two different scales have been used to represent accumulated and single-shot images because of significant variation in respective signal levels.

4.3.6 Pressure scaling of O fs TP-LIF signal

From Eq. 4.1 it is evident that if no interfering sources are present, the O-atom fs TP-LIF signal for constant laser irradiance at the probe volume should follow the following relationship

$$S_{TP-LIF} \propto \frac{N_o}{(Q_2 + A_2)} \quad 4.2$$

As the pressure increases, both N_o and Q_2 go up, but because of decreasing equilibrium mole fractions of the O atom with pressure the increase in N_o doesn't cancel the decrease in Q_2 . This leads to a decay in the $N_o/(Q_2 + A_2)$ curve with pressure, as shown Figure 4.8. Also, the actual laser irradiance available in the probe volume at different pressures might be different than what is measured outside the test rig due to laser absorption, and this can reduce the measurement accuracy. To compare S_{TP-LIF} with $N_o/(Q_2 + A_2)$ at different pressure, therefore, it is important to ensure that the laser irradiance remains the same at all conditions. As there is no direct way to measure the laser energy inside the high-pressure combustion test cell, a spectrometer (Acton SpectraPro.; Princeton Instrument) was placed at the end of the test cell and was used to measure the emitted unfocused 226 nm beam spectrum with an ICCD (PIMAX4, Princeton Instrument). The area under the curve of this spectrum is a function of input energy, energy absorbed by the windows, and path averaged loss in the test cell. We found a linear decrease from 5 $\mu\text{J}/\text{pulse}$ to 3 $\mu\text{J}/\text{pulse}$ in the probe volume

as the pressure was increased from 1 to 10 atm. The reason for this loss is still unclear but might be attributed to increase in absorption of the intense fs laser in the window with pressure, scattering by the combustion products inside the test cell, single-photon processes by nearby molecular transitions, etc. The corrected O-atom TP-LIF signal for constant laser irradiance at the probe volume was plotted against N_o/Q_2+A_2 and shown in Figure 4.8. Both plots were normalized to the corresponding atmospheric-pressure value. 700 shots were accumulated for each image and 100 such images were recorded and averaged for a range of pressures from 1 atm to 10 atm at $\phi = 0.85$. The experimental data closely follows the predicted pattern up to 5 atm, beyond which the measurements seem to under-predict the theoretical trend. At 10 atm it deviates from the predicted atomic oxygen concentration by almost 8%. This discrepancy may be attributed, in part, to the uncertainty associated with measurement of laser irradiance that is available in the probe volume or increased chemiluminescence of the high-pressure flame limiting the SNR. It is also partly attributed to a deviation of the Hencken burner from an adiabatic flame at high pressures.

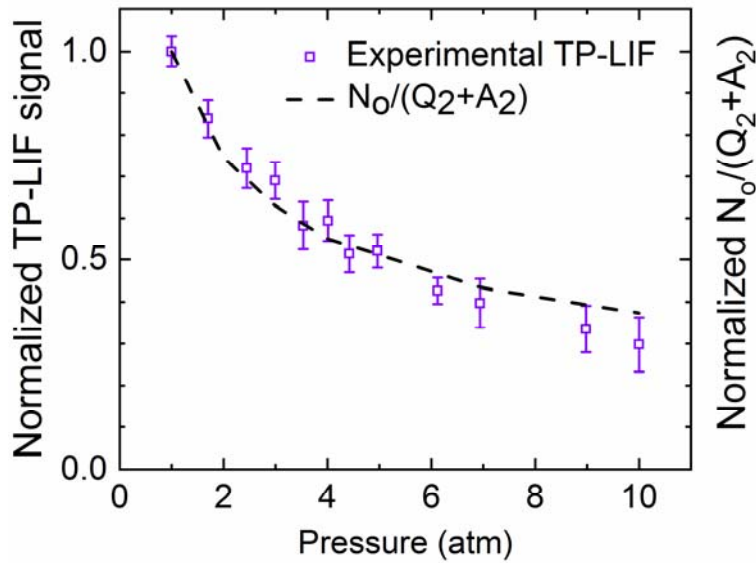


Figure 4.8 Fs TP-LIF signal of atomic oxygen and normalized N_o/Q_2+A_2 at different pressures in a $\phi=0.85$ H₂/Air Hencken burner flame. Both curves are normalized to the corresponding atmospheric pressure value. Laser energy of 5 μ J/pulse. Error bar presents $\pm\sigma$.

4.4 Conclusions

We have demonstrated the application of fs TP-LIF for the quantitative measurement of atomic oxygen in high-pressure flames. Challenges associated with high-pressure application of fs TP-LIF, such as multiphoton ionization, laser generated flame species, photolytic interferences, collisional quenching, background chemiluminescence, laser absorption and beam steering at high pressures were also addressed. It is suggested that the laser irradiance should not exceed $\sim 10^{11}$ W/cm² to avoid multiphoton de-excitation and photolytic interference. Excellent agreement was found with the theoretical atomic oxygen mole fraction for a range of equivalence ratios ($\phi = 0.65$ -1.15) and pressures (1-10 atm), enabling quantitative measurement of atomic oxygen in realistic combustion environments. A maximum single-shot SNR of 11 was achieved, which can be improved and potentially applied to kHz-rate measurements using burst-mode laser excitation and a high-speed intensifier with higher quantum efficiency in the near-infrared region.

5. HYBRID fs/ps VIBRATIONAL CARS THERMOMETRY IN HIGH-PRESSURE FLAMES

Modified from a paper published in *Optics Letters* **43**, 4911-4914 (2018).

Hans U. Stauffer, K. Arafat Rahman, Mikhail N. Slipchenko, Sukesh Roy, James R. Gord, and Terrence R. Meyer

Hybrid fs/ps vibrational coherent anti-Stokes Raman scattering (CARS) of nitrogen is reported for temperature measurements in high-pressure, laminar H₂–air and CH₄–air diffusion flames up to 10 bar. Following coherent Raman excitation by 100-fs-duration pulses, a time-asymmetric probe pulse—produced by passing a broadband, fs-duration pulse through a Fabry–Pérot étalon—is used to probe the coherence at different probe delays and evaluate the effects of collisions on the observed CARS signal. This asymmetric pulse permits detection of spectrally resolved N₂ CARS signal at the earliest probe delays (pulse peak delay ~200–300 fs), allowing full rejection of non-resonant contributions while still minimizing the effects of collisions—allowing single-shot precision of $\pm 2\%$. At these earliest probe delays, observed temperature-dependent signals are found to be independent of pressure over the 1–10 bar pressure range and the 1300–2300 K temperature range, whereas notable pressure dependence is observed at longer probe-pulse delays, becoming more pronounced both with increasing probe-pulse delays and with decreasing temperatures, where collision frequencies are higher.

5.1 Introduction

In recent years, several variants of femtosecond time-resolved coherent anti-Stokes Raman scattering (fs-CARS) have been developed with particular attention paid toward use of these approaches for combustion diagnostics [9, 67, 68, 88]. The hybrid femtosecond/picosecond (fs/ps) CARS technique [78, 81, 88, 91, 94] has shown particularly great promise for extension toward accurate thermometry at elevated pressures, primarily by the simultaneous virtues of a) readily assignable, spectrally resolved temperature-dependent features; b) the rejection of background nonresonant (NR) contributions; and c) the ability to complete single-laser-shot measurements within 1–10 ps to avoid collisional broadening effects that occur at longer timescales [81, 88]. Alleviating the need to model collision-dependent effects has been discussed as an important

possible benefit of time-resolved CARS approaches [73, 82], particularly since accurate modeling of collisions requires knowledge of colliding-partner mixture compositions. Recent fs-CARS work has emphasized the potential of vibrational N₂ CARS to exhibit pressure-independent behavior at early probe delays and at 300 K [73]. However, interference-free, single-laser-shot CARS temperature measurements within combustng flows at probe delays where the effects of collisions are expected to be negligible have not previously been reported at pressures above 1 bar.

In this work, we explore the pressure dependence of hybrid fs/ps vibrational CARS from N₂ gas in reacting flows. In contrast to rotational hybrid fs/ps CARS, in which single-laser-shot conditions at flame temperatures require high-intensity probe pulses [94], this approach can be implemented using simple spectrally narrowed probe pulses. A rapid-onset time-asymmetric, ps-duration probe pulse [81] is used to allow detection at delays as short as 200–300 fs after initial Raman excitation from time-overlapped \sim 100-fs-duration pump and Stokes pulses. This configuration allows optimal detection of spectrally resolved CARS signal free from NR background while minimizing the dependence on collisional effects. A range of fuel–air ratios are investigated in CH₄–air and H₂–air flames to vary temperature and collisional environment. Through careful selection of probe-pulse delay, we demonstrate pressure independence of CARS spectra—and therefore extracted best-fit temperatures—over a 1–10 bar pressure range and a 1300–2300 K temperature range. We also explore the accuracy and precision of such measurements at elevated pressures.

5.2 Experimental set-up for hybrid fs/ps VCARS

The experimental setup used in this work is depicted schematically in Figure 5.1. The primary laser source was a regeneratively amplified Ti:sapphire laser (Solstice Ace; Spectra-Physics, Inc.). The full-width at half-maximum (FWHM) bandwidth of the fundamental laser pulse was \sim 180 cm⁻¹ at 800 nm, with a corresponding nearly transform-limited pulse duration of 100 fs. The fundamental output was split into 4.3- and 2.9-mJ/pulse beams. The stronger portion pumped an optical parametric amplifier (OPA; TOPAS Prime; Light Conversion, Inc.), the output of which was subsequently doubled to produce the 675-nm pump pulse. 1-mJ fraction of the weaker portion was divided via a half-wave plate and thin-film polarizer into Stokes and probe pulses. A Fabry-Pérot étalon (TecOptics, FSR = 288 cm⁻¹; finesse \sim 109) was inserted into the probe beam path to produce a pulse with a time-asymmetric intensity profile exhibiting a rapid (\sim 150 fs) temporal

onset and a slower exponential decay with a 2-ps time constant [77]. Computer-controlled translation stages in the Stokes and probe beam paths were used to delay these pulses with respect to the pump pulse.

Measurements were made in a high-pressure stainless-steel test cell (see Figure 5.1) at pressures ranging from 1 to 10 bar. Optical access was provided via 1"-thick fused-silica windows that were purged with nitrogen to avoid coverage from soot and water condensation. A Hencken burner was used to produce near-adiabatic, laminar CH₄–air flames over a range of fuel–air equivalence ratios ($\phi = 0.8$ –1.25) to vary the equilibrium product-gas temperature within the probe volume. A maximum pressure of 6.6 bar was used for the CH₄–air flames to avoid rapid soot formation under fuel-rich conditions. Measurements were also made on a fuel-lean ($\phi = 0.36$) H₂–air flame at pressures up to 10 bar to extend the experimental conditions to the worst-case (highest) number-density conditions discussed below. The three input CARS beams were arranged with parallel polarizations into a folded BOXCARS configuration. A 500-mm focal length lens focused the beams to a long probe volume (length ~ 8 mm, cross-section ~ 0.1 -mm) located 8 mm above the burner surface; an identical lens collimated the nascent CARS beam. The pump, Stokes, and probe pulse energies at the probe volume were 45 μ J, 230 μ J, and 13 μ J, respectively. The CARS signal was spatially isolated, and dichroic mirrors were used to remove background luminosity of the high-pressure flame. This signal was spectrally dispersed in a monochromator (SPEX 1000M; SPEX Industries Inc.) equipped with a 1200-groove/mm grating and imaged onto a back-illuminated EMCCD (Newton^{EM}, Andor); the resultant detection-system dispersion was measured to be 1.5 cm⁻¹/pixel.

5.3 Considerations for CARS data fitting

Fits to the measured experimental spectra were carried out by modeling the time- and frequency-dependent CARS signal following the procedure described in a previous publication [99]; these fits incorporate a temperature- and pressure-dependent N₂ molecular response function, $R_4(t)$, as well as optical electric fields for the pump, Stokes, and probe pulses determined from measured pulse parameters (bandwidth and chirp). Because these experiments included measurements at some probe-pulse delays that are long compared to collisional timescales, it was

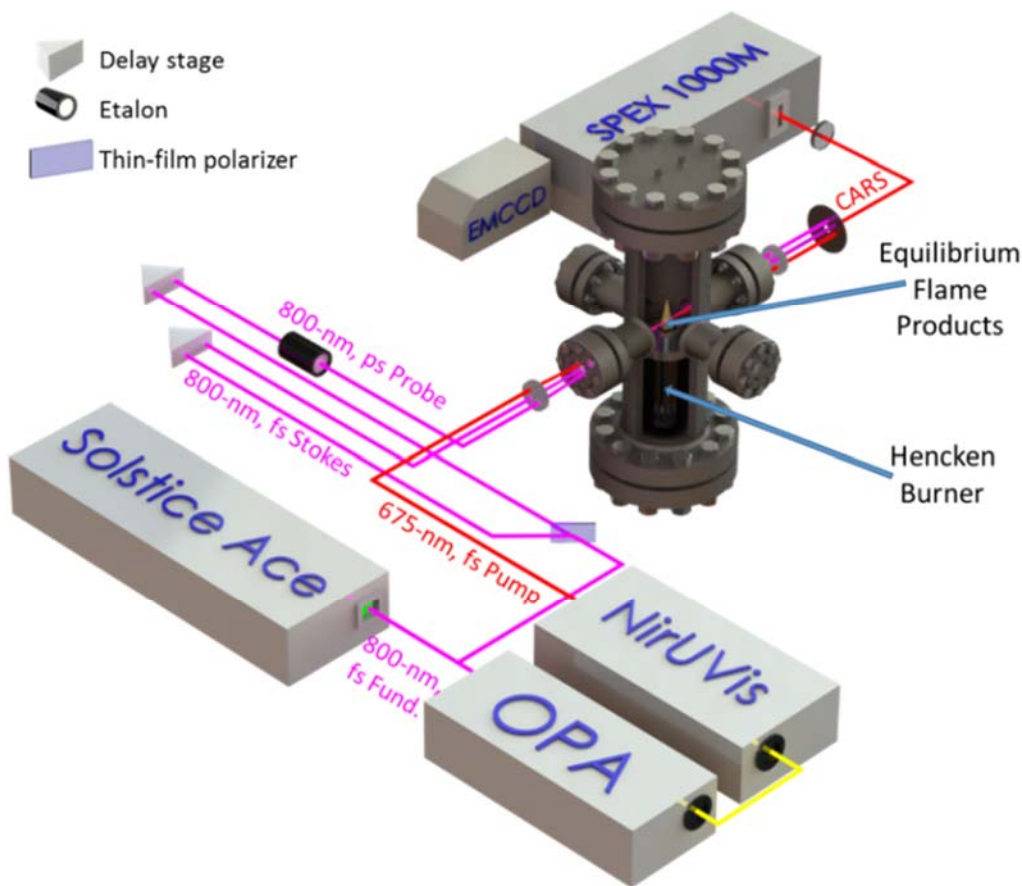


Figure 5.1 Schematic of experimental setup, including three-pulse CARS optical configuration and high-pressure vessel with Hencken burner flame.

important to include rotational-state-dependent linewidth (*i.e.*, time-dependent decay) behavior into the computational simulations. Further, the effects of line mixing have been accounted for in these simulations, following the methodology described by Knopp et al. [111, 173] and employed in prior pressure-dependent studies [73, 99, 111, 173] at room temperature. It is important to note that this prior work demonstrated that optimal matching between experiment and simulation is obtained using modified parameterized versions of the Energy Corrected Sudden (ECS) approximation toward rotational energy transfer (RET) under room-temperature conditions, although such optimal matching to high-pressure (1–5 bar) conditions required modification to the empirical parameters associated with these ECS approximations as compared to prior reported literature values [111]. Unfortunately, parameterized fits of these modified ECS models to linewidths measured at the high temperatures (1000–2500 K) associated with combustion have not been reported to date. Thus, we have instead used best-fit empirical parameters associated with a

modified exponential gap (MEG) model of RET for N₂ self-broadening, obtained via fitting of experimental linewidths from 300 K to 2000 K [45].

Less obvious in this response function, however, are additional J -dependent effects that begin to contribute at longer delays and high pressures associated with the facts that a) low- J N₂ Q -branch transitions generally decay more rapidly than do high- J transitions [45] and b) these low- J transitions are more closely spaced and, therefore, more susceptible to line-mixing effects [111, 173]. At sufficiently short delays, however, these two response-function curves are nearly indistinguishable. It is this feature that is exploited via the use of the time-asymmetric probe pulse, shown as $|E(t)|$ in Figure 5.2a-b and shifted to multiple probe-pulse delays in the experiments discussed below. The $\tau_{23} = 233$ fs delay is selected to be as early as possible while still rejecting the impulsive NR contributions that are present only when the time-overlapped pump and Stokes pulses are present, whereas $\tau_{23} = 32.1$ ps corresponds to an approximate probe delay at which enhanced temperature sensitivity has been observed over a large range of temperatures by virtue of partial recurrences associated with groupings of both low- J and high- J transitions [89].

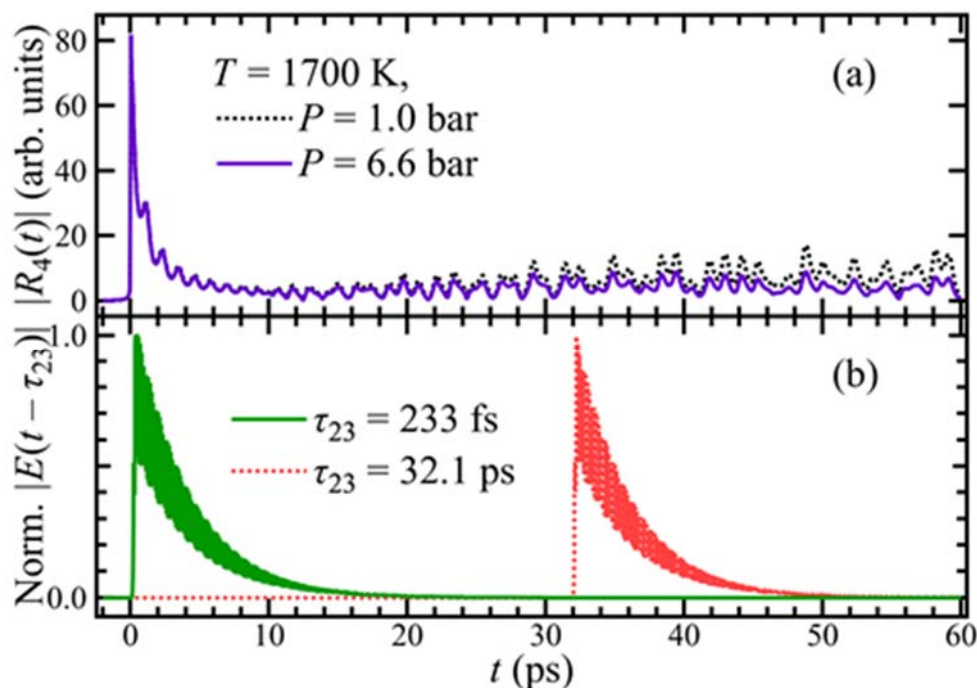


Figure 5.2 Time-dependent magnitudes of simulated (a) molecular response functions, $R_4(t)$, of N₂ at $T = 1700$ K and $P = 1.0$ and 6.6 bar and (b) probe electric fields at two delays ($\tau_{23} = 233$ fs and 32.1 ps).

5.4 Limits of collisional independence

Hybrid fs/ps CARS measurements were made at a variety of ϕ , pressures, and probe-pulse delays. Figure 5.3 depicts examples of normalized, 1500-laser-shot-averaged spectra at two temperature conditions, including $\phi = 0.36$ in a H₂–air flame (adiabatic temperature, $T_{\text{ad}} = 1330$ K) and $\phi = 0.80$ in a CH₄–air flame ($T_{\text{ad}} = 2000$ K) and three selected probe-pulse delays ($\tau_{23} = 233$ fs, 32.1 ps, and 100 ps). For the $\phi = 0.36$ case, results from $P = 1, 4.5$, and 10 bar are included, whereas $P = 1, 3.3$, and 6.6 bar results are shown for the $\phi = 0.80$ case. In comparing the CARS signals from the two equivalence ratio cases, it is clear that the temperature dependence manifests itself primarily in the relative intensities of the features near the bandhead of transitions initiating from the ground vibrational state ($1 \leftarrow 0$) and that of the vibrational hot band ($2 \leftarrow 1$).

Beyond this temperature dependence, the most striking feature from these results is that the spectra observed at the earliest ($\tau_{23} = 233$ fs) delay exhibit essentially no discernible differences in relative intensities of these features at all pressures. This includes the worst-case (highest) number-density scenario explored in this work [i.e., high pressure/low temperature shown in Figure 5.3a]. Exploration of the pressure dependence at lower temperatures is beyond the scope of this current work and will be investigated in future work. It was observed that this early-delay signal—where collisional decay is negligible—exhibited the expected N^2 dependence of the CARS signal on species number density. At the 32.1-ps delay, more notable pressure dependence is observed, particularly with reduced intensities in the low- J regions (near the vibrational bandheads) relative to the high- J regions with increased pressure. In the lower-temperature case ($T_{\text{ad}} = 1330$ K), this effect is obvious in comparing all three pressure conditions, whereas it is significantly less pronounced at $T_{\text{ad}} = 2000$ K. At the longest probe-pulse delay ($\tau_{23} = 100$ ps), obvious differences in relative peak intensities are observed at all pressures. The effects of collisional decay at long probe-pulse delays are further manifested in the relatively poor signal-to-noise ratio (SNR) observed at $\tau_{23} = 100$ ps and $P = 10$ bar [Figure 5.3e], in spite of the N^2 signal dependence observed at collision-independent conditions.

5.5 Temperature accuracy and precision

The temperature accuracy and precision of single-laser-shot hybrid fs/ps CARS measurements were explored at all measured ϕ , P , and τ_{23} conditions. Example results from these single-shot

measurements are depicted in Figure 5.4. Comparisons between selected single-shot spectra and the best-fit simulations used to extract temperature for three pressure conditions at $\phi = 0.8$ are shown in Figure 5.4a–c for $\tau_{23} = 233$ fs and Figure 5.4e–g for $\tau_{23} = 32.1$ ps. Also included as insets are probability density function histograms associated with 1500 single-laser-shot fits.

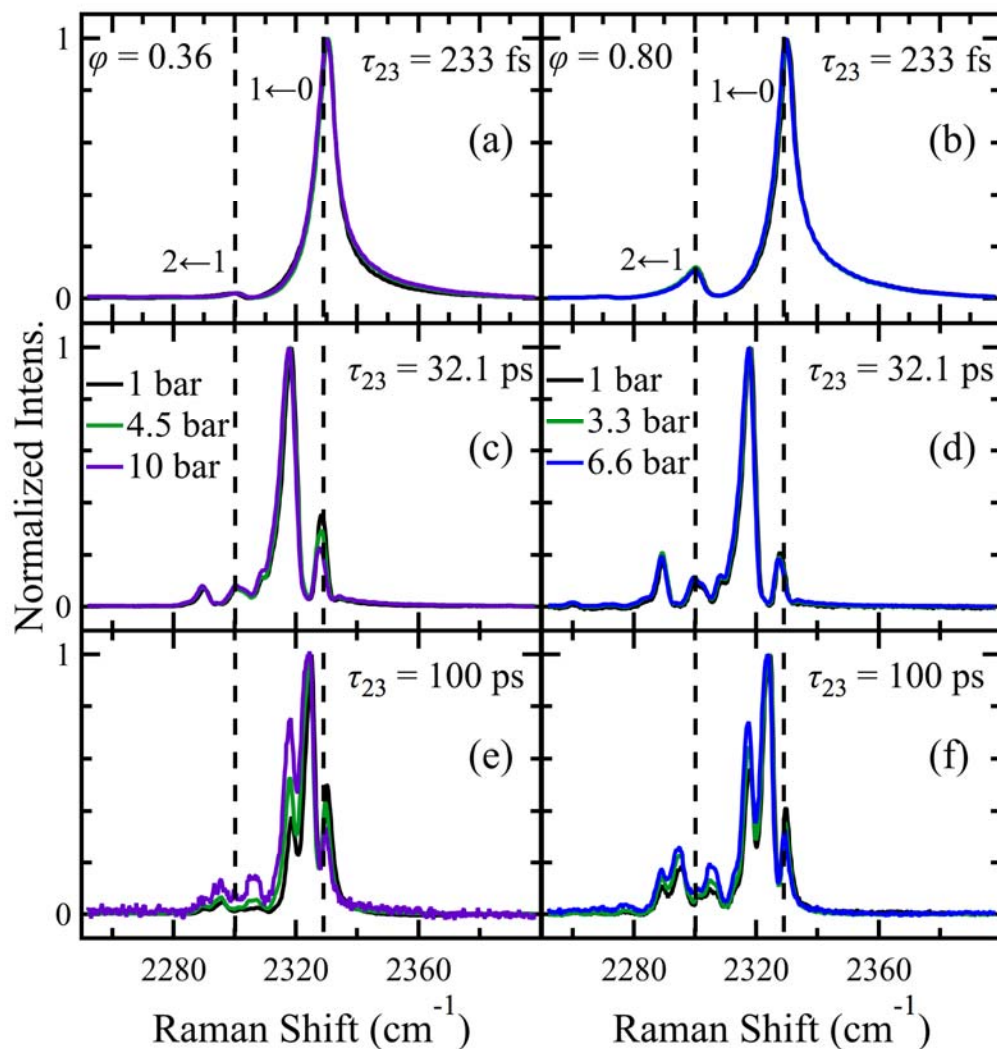


Figure 5.3 Normalized averaged (1500 laser shots) experimental CARS spectra at several P and τ_{23} . Panels (a), (c), and (e): spectra from H_2 –air flames at fuel:air equivalence ratio, $\phi = 0.36$ and $P = 1, 4.5$, and 10 bar. Panels (b), (d), and (f): spectra from CH_4 –air flames at $\phi = 0.8$ and $P = 1, 3.3$, and 6.6 bar. Probe-pulse delays include 233 fs [panels (a) and (b)], 32.1 ps [panels (c) and (d)], and 100 ps [panels (e) and (f)]. Dashed vertical lines: positions of $(2 \leftarrow 1)$ and $(1 \leftarrow 0)$ vibrational bandheads.

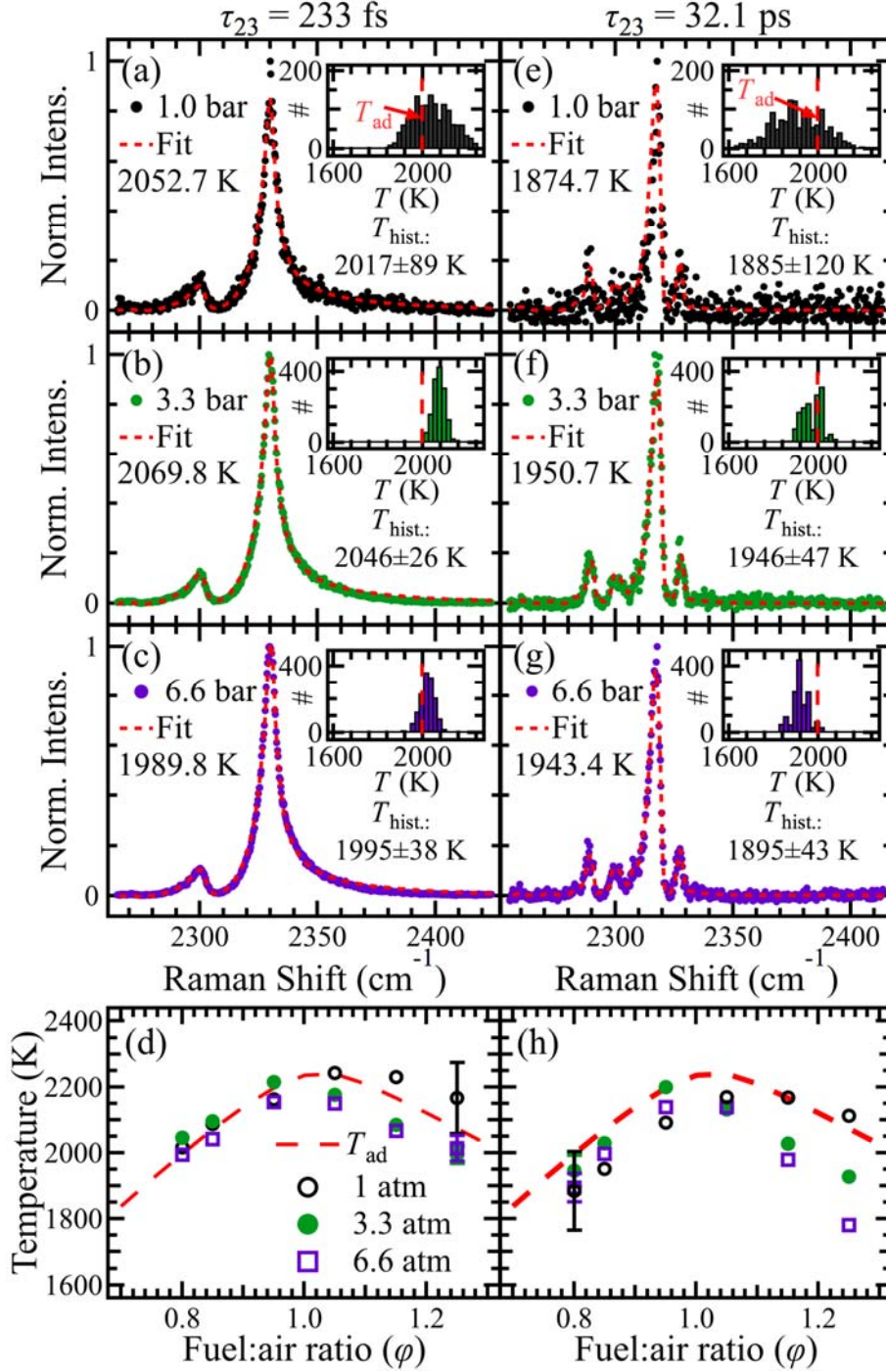


Figure 5.4 Pressure-dependent single-laser-shot results for $\tau_{23} = 233$ fs for CH_4 -air flame, $\phi = 0.8$. Panels (a)–(c): example single-shot spectra at three pressures (1, 3.3, and 6.6 bar, respectively) and corresponding best-fit simulations at denoted temperature. Inset histograms depict probability densities for 1500 laser shots. Panel (d): statistical average of best-fit T (1500 single-shot spectra) at $\tau_{23} = 233$ fs and several values of ϕ for these three pressures. Error bars ($1-\sigma$) are included for $\phi = 1.25$; comparable relative magnitudes are observed at all ϕ (excluded for clarity). Calculated T_{ad} denoted by vertical dashed curves.

At both delays, the 1-bar results exhibit poorer precision (relative standard deviation, σ , of $\sim 4.4\%$) than prior hybrid fs/ps CARS work ($\sim 2.2\%$) under similar conditions [77, 88], likely resulting from sub-optimal matching of the focal points of the three CARS beams. However, by virtue of the N^2 CARS-signal dependence, the SNR improves significantly at elevated pressures, resulting in excellent precisions (1.2–2.2%) at all measured temperatures.

The corresponding accuracies of measured temperature as compared to T_{ad} are shown in Figure 5.4d and Figure 5.4h for CH₄–air flames and $\phi = 0.8$ –1.25. Under fuel-lean conditions at all pressures and at $\phi = 1.05$ at 1 bar, observed accuracies $[(T_{avg} - T_{ad})/T_{ad}]$ are within 2% of the adiabatic temperature for the shortest delay. The accuracies are generally poorer for $\tau_{23} = 32.1$ ps, with simulated temperatures underestimating the adiabatic temperature by 4–6%; this systematic underestimation of temperature at longer probe delays has been observed previously at atmospheric pressure [77] under constraints where a single set of fit parameters is used to fit hybrid fs/ps CARS results at both short (≤ 1 ps) and long (~ 30 ps) probe delays. Under fuel-rich conditions, the 1-bar results for $\tau_{23} = 233$ fs also exhibit some overestimation of the adiabatic temperature; however, this overestimation is within the relatively large error bars associated with the 1-bar results, and similar high-temperature results have been observed previously in CARS measurements under fuel-rich conditions [77, 174]. More notable deviation from T_{ad} , however, is observed under fuel-rich conditions at elevated pressures, with best-fit temperatures deviating beyond the measured error bars below T_{ad} at pressures above 1 bar. These low-temperature deviations result from notably reduced ratios of intensities associated with the vibrational hot band ($2 \leftarrow 1$) features relative to those of the ($1 \leftarrow 0$) band at elevated pressures, and this behavior is also observed at longer probe delays, including $\tau_{23} = 32.1$ ps. Such behavior is inconsistent with poor fits resulting purely from collisional effects since similar collisional effects are not observed under lean conditions, where collision frequencies are comparable to or greater than those expected under fuel-rich conditions. Instead, it is anticipated that the actual flame temperatures in this type of burner are lower than the predicted equilibrium values under fuel-rich conditions and elevated pressures as a result of increased radiative losses from soot production and reduced flame lift-off from the Hencken burner surface, which increases conductive heat-transfer losses under these experimental conditions [175].

5.6 Conclusion

In conclusion, we have demonstrated hybrid fs/ps vibrational CARS measurements of N₂ in a combusting flow operating at elevated pressures (1–10 bar). Although pressure dependent behavior is observed at longer probe-pulse delays ($\tau_{23} > 30$ ps), particularly at reduced temperatures where species number densities are largest, the effects of collisions can be avoided by using early $\tau_{23} \sim 200$ –300-fs probe-pulse delays, facilitated by the use of a time-asymmetric probe pulse. Corresponding measured temperatures exhibit excellent accuracies and precisions—comparable to those observed previously for 1-bar combusting flows—particularly at elevated pressures.

6. FLEXIBLE CHIRP-FREE PROBE PULSE AMPLIFICATION FOR kHz fs-ps ROTATIONAL COHERENT ANTI-STOKES RAMAN SCATTERING

Modified from a paper *accepted with minor revisions*

K. Arafat Rahman, Erik L. Braun, Mikhail N. Slipchenko, Sukesh Roy, and Terrence R. Meyer

The sensitivity of high-repetition-rate hybrid fs/ps rotational coherent anti-Stokes Raman scattering (RCARS) is strongly influenced by the energy available for the ps probe pulse. In this work, a high-energy ps probe pulse that is time-synchronized with the fs pump/Stokes pulse is achieved by using a diode-pumped Nd:YAG amplifier seeded at 1064.4 nm by the output of a fs optical parametric amplifier. Nearly transform-limited, 10 ps pulses with up to 800 $\mu\text{J}/\text{pulse}$ and bandwidth of 1.9 cm^{-1} were generated at the second harmonic 532.2 nm and used for kHz-rate fs/ps RCARS thermometry up to 2400 K with accuracies of 1-2%. We furthermore demonstrate amplification of variable pulsewidths for flexible single-mode (chirp-free) RCARS signal generation.

6.1 Motivation

Until now, the two exemplary methods for the single-laser approach to hybrid fs/ps CARS have been the 4- f pulse shaper, with excellent spectral resolution but low energy throughput, and the SHBC, with high energy yield but limited spectral bandwidth selectivity and more complicated modeling of the CARS spectra. In this work, we demonstrate spectral filtering of the output of a fs optical parametric amplifier followed by diode-pumped Nd:YAG amplification to generate inherently time synchronized, spectrally tailored, spectrally pure, transform-limited, high-energy ps probe pulses. This approach is demonstrated for kHz-rate fs/ps RCARS thermometry and with few model corrections in an H_2/Air Hencken burner flame up to 2400 K.

6.2 Design of the ps-probe amplifier

The primary laser source was a regeneratively amplified Ti:sapphire laser (Solstice Ace; Spectra-Physics, Inc.) that outputs 100 fs, 7 mJ, 800 nm pulses with a nearly transform-limited bandwidth

of $\sim 180 \text{ cm}^{-1}$ at 1 kHz repetition rate, as shown in Figure 6.1a. The fundamental output was split into 3 mJ/pulse and 4 mJ/pulse beam paths, and a portion of the 3 mJ/pulse beam was used for the pump/Stokes beam in the two-beam RCARS setup. The 4 mJ/pulse portion pumped an optical parametric amplifier (TOPAS Prime; Light Conversion, Inc.) to generate the idler at 2128.8 nm, which was subsequently frequency doubled in a BBO crystal to produce radiation at 1064.4 nm. At this wavelength, the available laser energy was 60 $\mu\text{J}/\text{pulse}$. This beam was then routed to a custom narrowband spectral amplifier (NSA), as shown in Figure 6.2b. The NSA consisted of commercially available VBGs (OptiGRATE Corp.), which gives the spectral selectivity of the system, and two diode-pumped Nd:YAG amplifier modules to amplify the selected spectral portion of the beam. The output linewidth of the VBG is inversely proportional to the grating thickness and depends on the refractive index modulation.

Two different VBGs encoded for $\sim 1064 \text{ nm}$ were used with spectral selectivity of 0.41 nm (VBG-I) and 0.27 nm (VBG-II) (measured by MOGLabs, LLC), which correspond to bandwidths of 3.6 cm^{-1} and 2.4 cm^{-1} and output energies of $\sim 0.33 \mu\text{J}/\text{pulse}$ and $\sim 0.13 \mu\text{J}/\text{pulse}$, respectively. This spectral filtering of the original fs pulse output from the OPA produces a ps pulse by virtue of the time-bandwidth product (TBP), which is inherently time-synchronized with the mJ-level 800 nm fs pulses used for the pump/Stokes CARS excitation. The spectrally narrowed low energy ps pulses were passed through a spatial filter and optical isolator before being amplified in the diode-pumped Nd:YAG modules. The spatial filter, present before the double-pass amplification stage, facilitates removal of spatial irregularities in the beam profile originating from the OPA and the VBG and is a necessary condition to avoid small-scale self-focusing in the Nd:YAG rods (discussed below) [176].

6.3 Amplifier output pulse characteristics

The small-signal gains (SSG) of the two diode-pumped Nd:YAG modules were measured with a narrowband ns pulsed source near 1064.4 nm and are shown in Figure 6.1c. The first amplifier module, Amp1 in Figure 6.1b (RBAT24-1P; Northrop Grumman Corp.), has a maximum SSG of 48 with 1 kW of supplied electrical power and a pump duration of 312.5 μs at a repetition rate of 1 kHz. The second amplifier, Amp2 in Figure 6.1b (RBA20-1C; Northrop Grumman Corp.) was pumped with a total supplied pump power of 0.8 kW and a 240 μs pump duration at 1 kHz for a maximum SSG of ~ 10 . The diode module drivers were triggered by the fs laser source, and the SSG was measured with respect to this delay. Water cooling was provided for homogenous heat

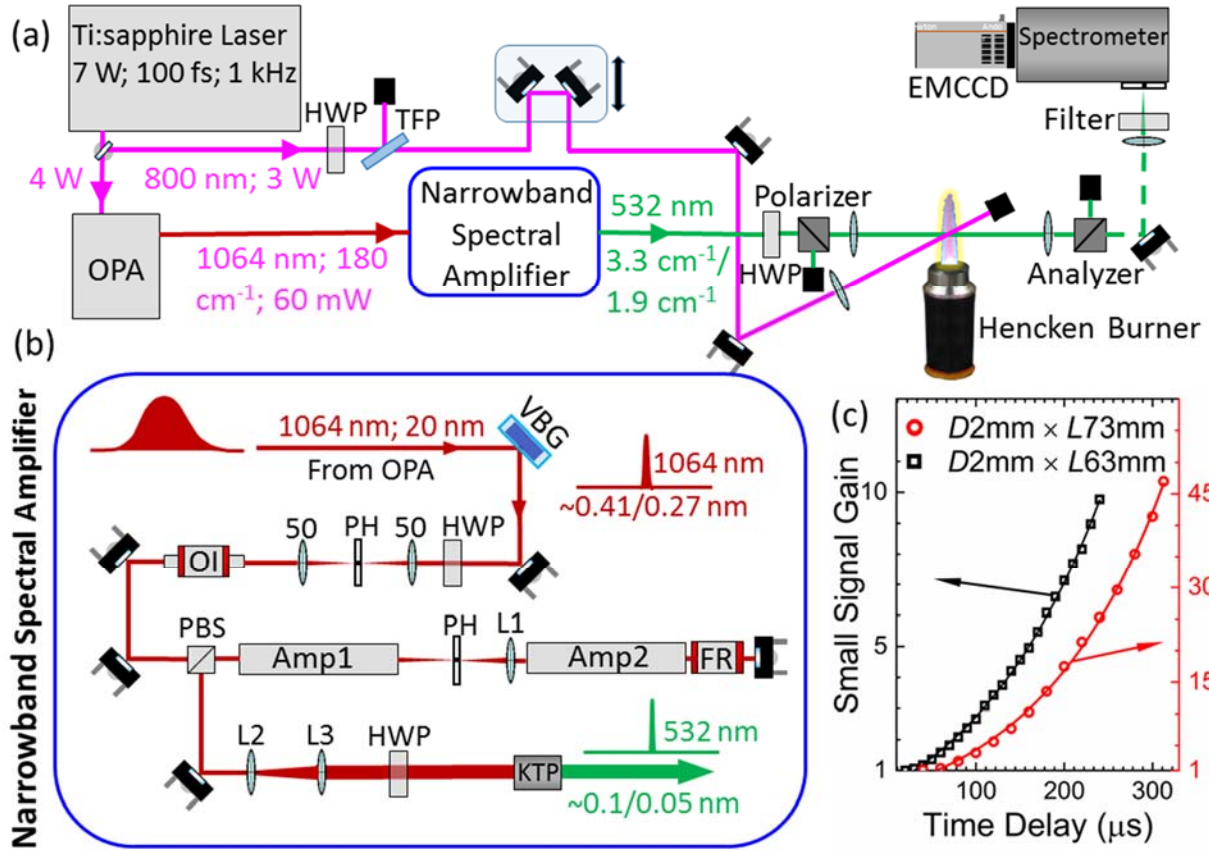


Figure 6.1 Experimental set-up. (a) Two-beam RCARS setup. (b) Layout of the narrowband spectral amplifier; VBG: volume Bragg grating, HWP: half wave plate, PH: pinhole, OI: optical isolator, PBS: polarizing beamsplitting cube, TFP: thin film polarizer, FR: Faraday rotator. (c) Small-signal-gain of the diode-pumped Nd:YAG amplifier modules; D: Diameter, L: Length, Solid line: Single exponential fit.

removal from the Nd:YAG rods, and the coolant temperature was optimized and kept constant for maximum gain in each module.

Throughout the experiment, the electrical energy input into the amplifier stages was kept constant while the time delay was varied to change the gain. At the maximum pump level, the focal length of the thermally induced lens in the Amp1 laser rod was ~ 50 mm, and a pinhole was placed at the focal plane (see Figure 6.1b). The focal length of the thermally induced lens in Amp2 was ~ 300 mm. Lens L1 was used such that the combination of L1 and the thermally induced lens in Amp2 recollimated the beam and completed the relay optics. This arrangement prevented the build-up of ASE and compensated for the thermally induced curvature in the propagating beam wave-front. A 45° Faraday rotator was placed before the 0° mirror to compensate for thermally

induced birefringence. The system was designed keeping the gain of Amp2 fixed at its maximum while only varying the gain in Amp1.

The double-pass output energy as a function of input energy for both VBGs is shown in Figure 6.2a. The optical isolator and HWP were used to vary the input energy, and the highest output energy was ~ 650 $\mu\text{J}/\text{pulse}$ and ~ 1.3 mJ/pulse at 1064.4 nm for VBG-I and VBG-II, respectively. Incorporating losses in the double-pass system, and linear operation in the small-signal regime, the effective SSG was calculated to be ~ 5 and ~ 12.5 in Amp1 for the VBG-I and II respectively and ~ 10 in Amp2 for both cases, which is consistent with the measured values for the corresponding time delay in Figure 6.1c. At the maximum output energy, the pulse energy has a standard deviation of $\sim 2.3\%$ of the mean for the system, measured with photodiode sampling for 5 minutes. The measured values for the first 40 seconds are shown in Figure 6.2b. The inset in Figure 6.2b shows the stability of the spectrally tailored OPA seed source.

The quality of the beam, M^2 , was measured after L3 as the amplified ps pulse transmitted through a 100-mm focal length lens, and a series of time-averaged beam profile measurements were acquired along the optical axis to take $D4\sigma$ beam diameter measurements (see Figure 6.2c). The resulting M^2 value in the x and y directions were 3.5 and 1.6 respectively. The slightly elliptical beam is shown in Figs. 2d and e for the near- and far-field beam profiles, respectively. The inferior M^2 in the x-direction was determined to originate from the VBG operating with the broadband OPA output beam and not from any nonlinearities, since the shape of the output beam was found to be independent of the amplified beam intensity.

After the two-pass, two-stage amplification, the amplified 1064.4 nm beam was frequency doubled in a 6 mm long KTP crystal (Type II). A second harmonic generation (SHG) conversion efficiency of $\sim 63\%$ was achieved at a fluence of $2 \text{ mJ}/\text{cm}^2$. As such, output beam energies of ~ 400 $\mu\text{J}/\text{pulse}$ (VBG-I) and ~ 800 $\mu\text{J}/\text{pulse}$ (VBG-II) at 532.2 nm were available to be used in the RCARS experiment. The ~ 400 $\mu\text{J}/\text{pulse}$ beam had a FWHM bandwidth of 3.3 cm^{-1} , measured after deconvolution with a separately measured 1.7 cm^{-1} spectrograph line spread function (see Figure 6.3a). The time-domain pulse shape was measured by pump-probe intensity cross correlation of the non-resonant signal in argon with the 100 fs pump/Stokes beam and found to be 5.25 ps at FWHM (see Figure 6.3b). This yielded a TBP within ~ 1.1 of the transform limit, and both time and frequency domain pulses showed excellent Gaussian profiles, free from any side-band

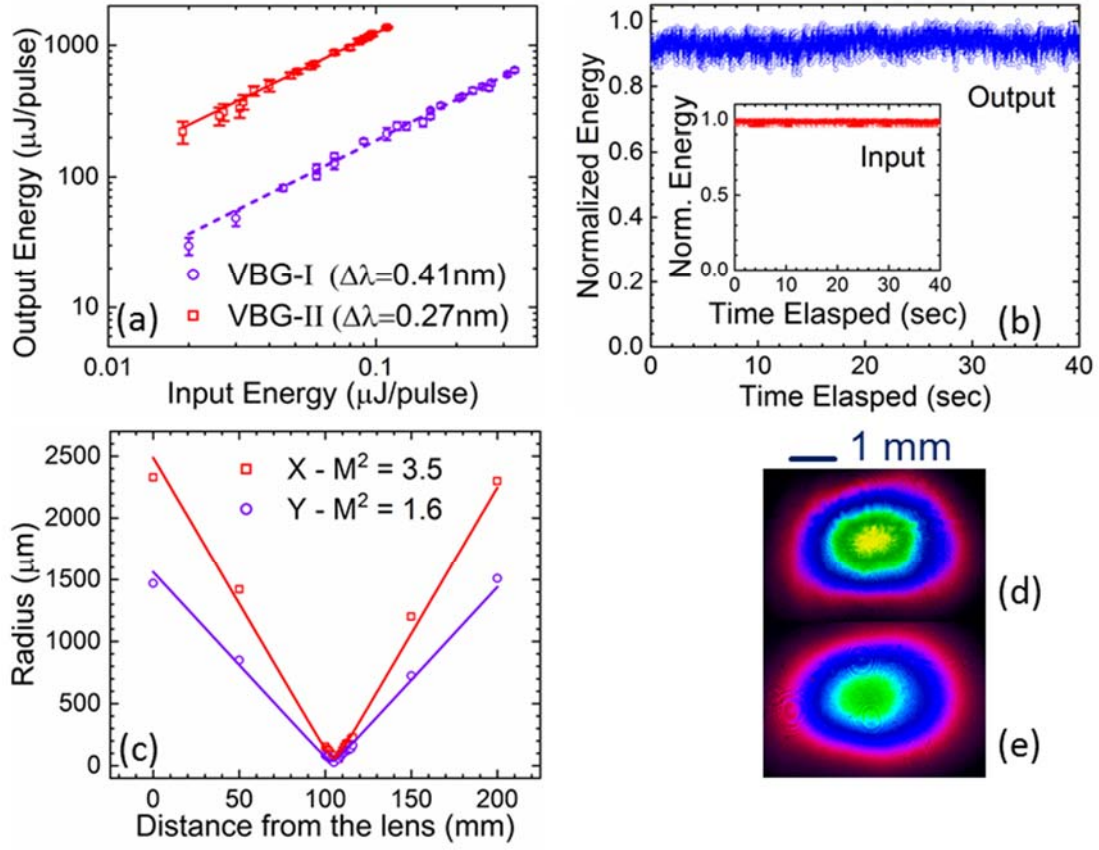


Figure 6.2 Amplifier output characteristics at 1064.4 nm. (a) Input vs. output energy for both VBGs; Error bars: $\pm\sigma$, Solid lines: linear fit. (b) Pulse-to-pulse stability of input and amplified output. (c) Beam quality, M^2 . (d) Near-field beam profile. (e) Far-field beam profile.

structure or spectral wings. This eliminates the necessity for any pre-processing of the ps probe before the nonlinear interaction with pump/Stokes beams for CARS measurements and greatly simplifies the modeling of this virtually chirp-free ps probe. Similar measurements were done for the ~ 800 $\mu\text{J/pulse}$, 532.2 nm beam (VBG-II). The measured linewidth and time-domain cross-correlation, shown in Figure 6.3, has a FWHM bandwidth of ~ 1.9 cm^{-1} and pulsewidth of ~ 10 ps.

Self-focusing and self-modulation of short pulses in an active medium due to the electronic Kerr-effect can severely restrict the overall amplification and output beam quality of the amplified pulse [176], and was the limiting factor in utilizing this system for higher gain. A fraction of the output beam was monitored in a beam profiler to assess potential whole beam self-focusing (WBSF) as we increased the gain in Amp1 for a fixed input energy. As the beam traversed the laser rod, the beam power was sufficiently high to induce WBSF during the second pass

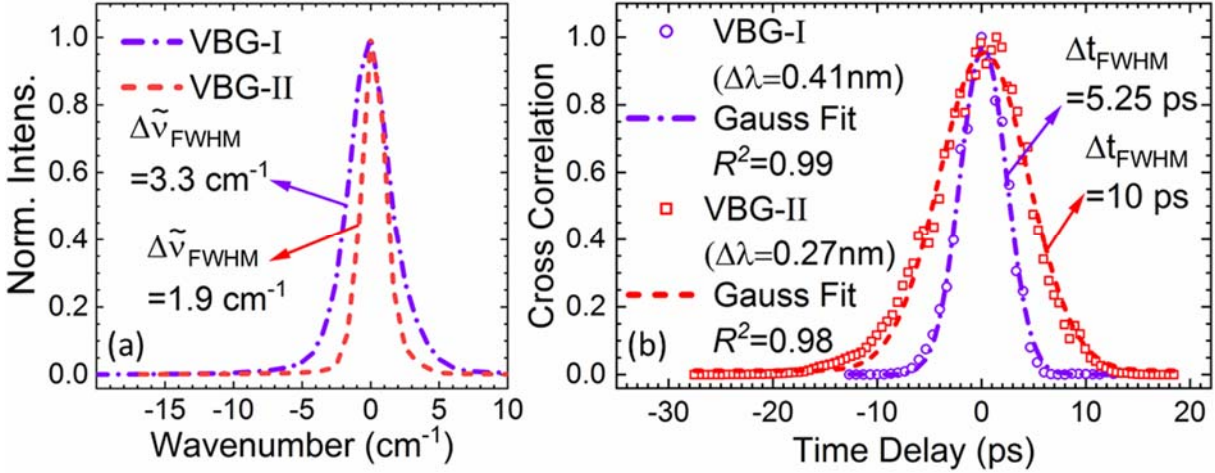


Figure 6.3 Frequency and time-domain characteristics of amplified beam after SHG. (a) Measured spectrum of 532.2 nm beam; $\Delta\tilde{\nu}$: bandwidth. (b) Time-domain cross-correlation of the same.

through Amp1. However, the length of the Nd:YAG rod was too short for any catastrophic collapse of the whole beam even at the maximum output of the system; rather, the gain medium acted as a nonlinear lens. At the maximum output energy of $\sim 1.3 \text{ mJ/pulse}$ (VBG-II), the gain medium in the return pass for Amp1 acted as a lens with an equivalent focal length of $\sim 450 \text{ mm}$, which is close to the theoretically calculated value of $\sim 430 \text{ mm}$ [177]. Moreover, at this combination of short length and ps-duration pulse, frequency broadening due to intensity dependence of the index of refraction is “too slow” to catch up and, therefore, can be neglected [178]. The overall effect of this nonlinearity can be viewed as an introduction of curvature in the wave-front. Hence, Lenses L2 and L3 (Figure 6.1b) were used after the PBS as an integral part of the system to recollimate and expand the slightly converging beam for frequency doubling. Systems at these conditions are more susceptible to small-scale self-focusing (SSSF), and a good measure of this effect is the so-called *B*-integral [177]. At the maximum output of 1.3 mJ/pulse for the 10-ps duration pulse, the calculated value of *B*-integral was ~ 1.5 which is lower than the proposed threshold value of 2 for any buildup of SSSF [179]. Increasing the gain in Amp1 more could yield more energy in the output pulse while staying in the small-signal regime, but above 1.8 mJ/pulse “hot spots” were observed in the amplifying beam, and further increase of the gain could result in SSSF and catastrophic damage to the laser rod. At this point, the calculated *B*-integral is ~ 2.1 . As such, it was safe to restrict the operation up to $\sim 1.3 \text{ mJ/pulse}$ to avoid damage in Amp1 and the PBS upstream, where the output beam gets rejected.

Although significant gain narrowing was evident for both VBGs, it was more dominant for VBG-II (from 2.4 cm^{-1} input to 1.9 cm^{-1}) as a result of the much higher gain. This could be viewed as a potential mechanism for controlling the linewidth of the output ps-pulse, thus eliminating the need for the VBG before the amplifier modules.

6.4 Two-beam rotational CARS at flame temperature

The two-beam RCARS scheme used here was reported in Ref. [84, 180]. The pump/Stokes photons were automatically overlapped spatially and temporally while the generated ps probe from the amplifier was time synchronized to the pump/Stokes pulses by its design. A delay stage in the pump/Stokes beam path provided the relative delay to match the arrival times of the fs and ps pulses at the RCARS probe volume. In all experiments, the pump/Stokes power was $\sim 100\text{ }\mu\text{J/pulse}$ or less to avoid nonlinear self-phase modulation. Two $f = 300\text{ mm}$ lenses were used to focus the pump/Stokes and probe beams in the probe volume with a crossing angle of $\sim 30^\circ$. The spatial resolution in the direction of probe beam propagation was measured to be $90\text{ }\mu\text{m}$, which was an order of magnitude better than a similar BOX-CARS arrangement [94]. Temperature measurements were carried out in a H_2/Air Hencken burner flame, which produces a nearly adiabatic flame for a wide range of equivalence ratios (Φ). As the CARS signal co-propagates with the probe, a polarization gating technique was employed to separate the signal beam from the probe beam. To minimize the residual probe that bleeds through the polarization gating and spectral wings of the probe, which is comparable to the flame temperature RCARS signal, a combination VBG notch filter (OptiGrate; BNF-532-OD3) with 0.3 nm bandwidth at 532 nm and a $515 \pm 15\text{ nm}$ bandpass filter (Semrock FF01-515/30) were used. The RCARS signal was then dispersed by a 500 mm , 1200 g/mm spectrograph (PI-Acton, 1.7 cm^{-1} measured resolution) onto a back-illuminated EMCCD (Andor). Processed experimental spectra were fit for temperature using a simple phenomenological N_2 -RCARS model. The details of the modeling are laid out in the previous literature [97, 99], and will not be presented here. The electric field of the probe pulse was included in the time-domain CARS model as a Gaussian shape with measured spectral and temporal characteristics, but the pump/Stokes field was not explicitly included in the model. Rather, it was assumed that the pulses were TL and delta functions in time [91]. The spectral response of the pump/Stokes pulses was imparted on the convolution of the probe and

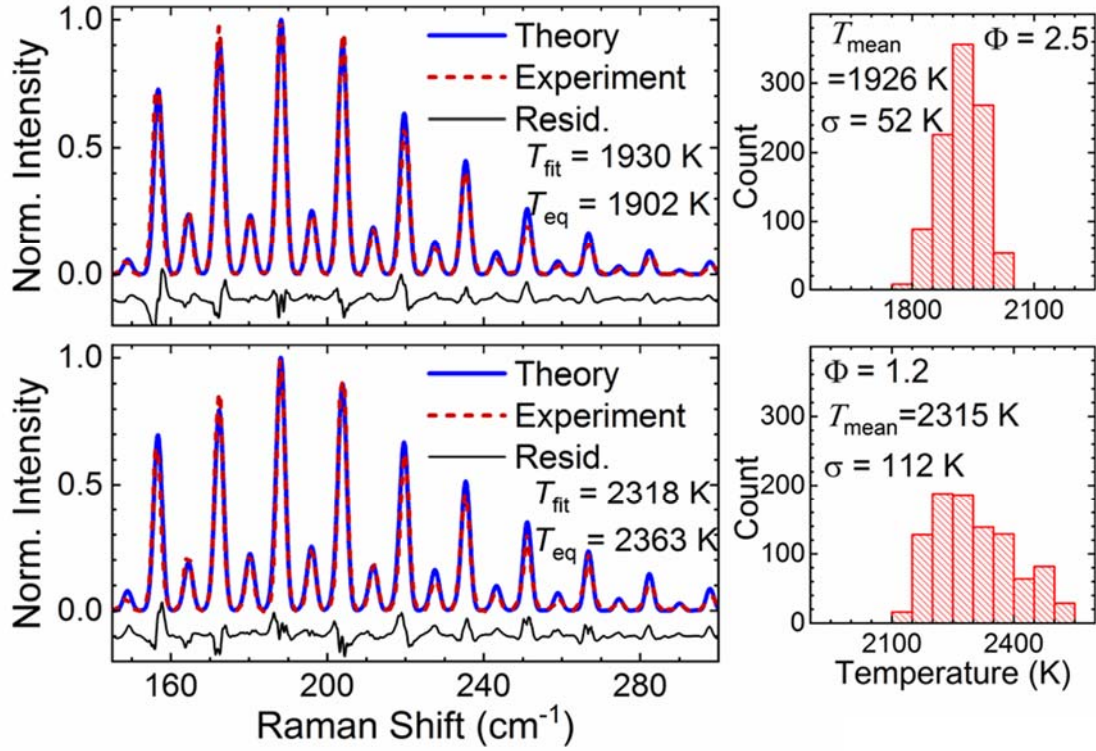


Figure 6.4 Measured RCARS spectra. 1000 shots averaged at $\Phi = 2.5$ and 1.2 (left column) and 1000 single-laser-shot temperature histograms (right column). 1.9 cm^{-1} ; 10-ps probe. Probe delay 19.5 ps.

molecular response via multiplication of the modeled molecular response with an experimentally obtained non-resonant signal in argon, measured with the same filters used to acquire the RCARS spectra. The nearly transform-limited Gaussian ps probe optimized the parameter space for the modeling and provided an excellent match with theoretical and experimental spectra up to ~ 2400 K. For the shot-averaged spectra at $\Phi = 2.5$ and 1.2 in Figure 6.4, fits yield temperatures were within 1.4% and 1.9% of the equilibrium calculation. Temperature precisions were derived from the single standard deviation of the 1000 single-laser-shot histograms and were 2.7% and 4.8% of the histogram means, respectively, for the same Φ . This slightly suboptimal precision can be attributed to low SNR in the high J -states, but can easily be improved by techniques described in literature [181]. Nonetheless, peak SNR in excess of 20 was achieved for a single-shot measurement at ~ 2400 K. Typical single-shot spectra at $\Phi = 2.5$ and 1.2 along with corresponding best-fit simulations at the denoted temperatures are shown in Figure 6.5.

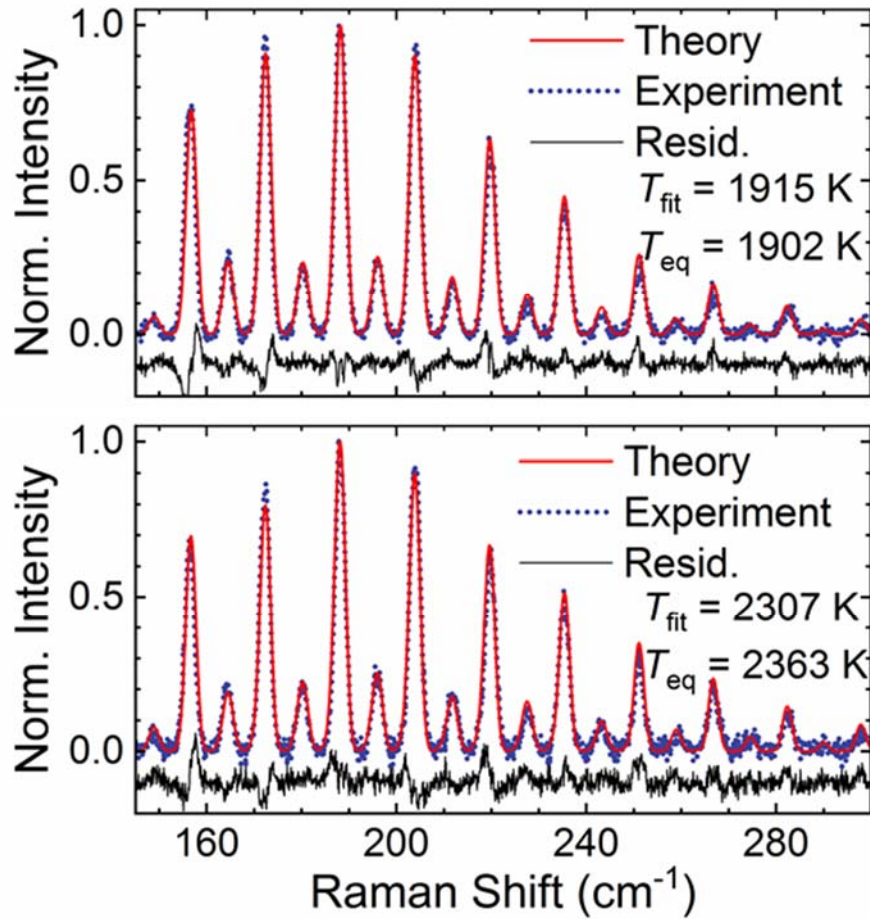


Figure 6.5 Example single-shot spectra at $\Phi = 2.5$ (top) and 1.2 (bottom) and the corresponding best-fit simulations at the noted temperatures.

6.5 Summary

In summary, we have demonstrated generation of single-mode, high-energy ps-probe pulses from initial fs radiation for kHz-rate hybrid fs/ps RCARS, providing versatility in both spectral resolution selectivity and energy throughput. Transform-limited pulses with 800 $\mu\text{J}/\text{pulse}$ and 1.9 cm^{-1} bandwidth were then utilized for two-beam RCARS thermometry in an H_2/air Hencken burner flame up to 2400 K. Excellent spatial, spectral, and temporal beam quality allowed for fitting the theoretical spectra with a simple Gaussian model for the probe pulse. From the current data on small signal gain, this versatile amplification system has the potential to produce even higher energies by using narrower probe pulses (e.g., 3 mJ/pulse at 532.2 nm with $\sim 0.5 \text{ cm}^{-1}$ bandwidth) or improve sensitivity for single-shot measurements at higher repetition rates.

7. CONCLUSIONS AND FUTURE WORK

The research presented in this dissertation are the first demonstrations of femtosecond two-photon laser-induced fluorescence and hybrid fs/ps coherent anti-Stokes Raman scattering in high-pressure reacting flows. The primary goal of this dissertation is to advance the nonlinear ultrafast laser-diagnostics techniques in situations relevant to advanced propulsion systems. The first logical step toward this objective is to validate these ultrafast laser-diagnostic techniques in high-pressure, properly calibrated, reacting flows to experimentally derive pressure scaling characteristics for temperature and key combustion relevant species while accounting for a multitude of signal interfering processes that can obfuscate the applicability of such nonlinear techniques, especially in optically accessible extreme environments.

7.1 Summary

Femtosecond TP-LIF was demonstrated for quantitative single-shot or kHz-rate measurements of the CO mole fraction at elevated pressures in a CH₄/air calibration burner. Careful attention to the potential sources of photolysis allowed a very good match between the theoretical CO equilibrium mole fraction predictions and the TP-LIF signal at different pressures and for varying equivalence ratios. Detailed investigation of CO fs TP-LIF emission spectra showed evidence of simultaneous excitation of diagonal bands [$B'\Sigma^+(v'=0,1) \leftarrow X'\Sigma^+(v''=0,1)$] at flame temperatures. This finding helped correct prior misinterpretations of carbon monoxide TP-LIF emission spectra and has the potential for temperature measurement using CO fs TP-LIF. Although quantitative measurement of CO concentration was made in a well-calibrated flame, feasibility to acquire single-shot images of CO fs TP-LIF to discern the single-shot structure of the CO concentration field in non-uniform or unsteady flames was demonstrated at pressures up to 12 atm. The relative merits of two different imaging systems were also addressed with a view towards future investigations in unsteady, non-uniform flames.

Although, pressure specific calibration of fs TP-LIF systems in a flame with known equilibrium products enabled quantitative CO concentration measurement at different pressures, other pressure dependent deexcitation or loss mechanisms were found to yield deviations in pressure scaling of TP-LIF signal from the theoretical predictions. As such, a second set of

experiments were conducted for fs CO TP-LIF measurements at pressures up to 20 atm in a well-characterized mixing chamber filled with different volume fractions of CO and different buffer gases—emulating different collisional environments and eliminating uncertainties associated with the non-uniform Hencken burner flame at high-pressure. It was found that nonlinearities in the pressure-strained windows could significantly change the spectral and temporal quality of the UV radiation and reduce the overall TP-LIF signal. Proper selection of window material and optimum beam size at the windows to avoid such multiphoton absorption and degradation of the input beam was reported. No significant contribution of collisional quenching and forward lasing was found on the CO fs TP-LIF signal at varying pressures for the laser irradiance up to $\sim 1.7 \times 10^{10}$ W/cm². Rather, the main deexcitation mechanisms were found to be the attenuation of source laser by the broadband absorption of multiple combustion relevant species and 2+1 photoionization process through the $X^2\Sigma^+ \leftarrow B^1\Sigma^+$ transition of excited state CO.

The overall effect of attenuation of the source laser was a pressure dependent irradiance availability in the probe volume. By measuring the attenuation using an unfocused beam, a correction factor was introduced to partially correct for this drop-in irradiance at the probe volume. This effect was exacerbated in flame due to the broadband absorption of UV radiation by flame species, such as CO₂ and H₂O. Secondly, the 2+1 photon absorption-based ionization process exacerbated the CO fs TP-LIF signal decay at elevated pressure. As the number density of probed species goes up with pressure, effects of photoionization that could be overlooked at atmospheric conditions can become significant at higher-pressures. Single-photon absorption features were observed by analyzing the spectrum of the transmitted UV-beam after the two-photon excitation process at various CO number densities and for varying laser irradiances. It is proposed that to avoid the contribution of 2+1 photoionization over the full range of experimental conditions, one should find the perturbation-free input laser irradiance by analyzing the transmitted excitation beam at the highest number density to be attained in a given experiment and using the same irradiance through the entire experiment. It is suggested that at a pressure of 20 atm, a temperature of 300 K, and with a CO mole fraction of 6%, the laser irradiance should not exceed $\sim 6 \times 10^9$ W/cm² at the probe volume to avoid significant contributions from multiphoton loss mechanisms. At flame temperatures, lower number densities may allow higher laser irradiance to avoid 2+1 photoionization while ensuring sufficient signals using standard detection schemes. An interesting observation can be inferred from the linearity of 2+1 photoionization process with the number

density of CO—quantitative CO fs TP-LIF measurement is possible even in the presence of photoionization by proper calibration of the experimentally acquired TP-LIF signal with a flame with known equilibrium concentrations, e.g. Hencken burner flame. Additionally, contribution from minor loss mechanisms, such as beam defocusing due to change in the refracting index of the gas media with increasing pressure and signal trapping at elevated pressures were also quantified. Finally, attenuation of source laser by the broadband absorption of different combustion relevant species, beam defocusing, and fluorescence signal trapping can be concluded to be the three limiting factors for high-pressure diagnostics of fs TP-LIF.

The measurement protocols established for carbon monoxide was then applied for measurements of atomic oxygen in a H₂/air Hencken burner flame for pressures up to 10 atm. Careful investigation of relevant photolytic precursors for atomic oxygen ensured excellent agreement with the theoretical atomic oxygen mole fraction for a range of equivalence ratios ($\phi = 0.65$ -1.15) and pressures (1-10 atm), enabling quantitative measurement of atomic oxygen in realistic combustion environments. It was suggested that the laser irradiance should not exceed $\sim 10^{11}$ W/cm² to avoid multiphoton de-excitation and photolytic interference. A maximum single-shot SNR of 11 was achieved, which can be improved and potentially applied to kHz-rate measurements using burst-mode laser excitation and a high-speed intensifier with higher quantum efficiency in the near-infrared region.

In addition to investigations of the fs TP-LIF technique for species concentration measurements at high pressure, hybrid fs/ps CARS thermometry was performed for interference-free temperature measurements in high-pressure flames. Vibrational CARS measurement of N₂ was reported for temperature measurements of 1300–2300 K in high-pressure, laminar H₂/air and CH₄/air diffusion flames up to 10 atm. Limits of collisional independence of the vibrational CARS thermometry was investigated using a time-asymmetric probe pulse at different time delays (τ_{23}), equivalence ratios, and pressures. Full rejection of nonresonant contribution to the CARS signal was achieved with the time-asymmetric probe pulse delayed at ~ 200 -300 fs, while the thermometry being also independent of collisions. However, at longer probe delays ($\tau_{23} > 30$ ps), particularly at reduced temperatures and high-pressure, where collisional dephasing is more dominant, pressure dependent behaviors were observed. A $\pm 2\%$ precision was achieved in measured single-laser-shot temperatures at elevated pressures. Temperature accuracies were also reported for the pressure range mentioned above for two different probe delays of 233 fs and 32.1 ps.

Finally, a novel chirp-free, flexible probe-pulse amplification technique was reported for kHz-rate hybrid fs/ps rotational CARS up to high temperatures. As increased pressure causes the mixing of individual rovibrational lines and eventual collapse of the individual Q-branch structures, which is difficult to model, pure rotational CARS with sparsely separated S-branch transitions has the potential to be an ideal candidate for high-pressure flame thermometry. However, flame temperature rotational CARS is challenging to implement as finite bandwidth of the fs-excitation pulse limits the ability to probe high J -transitions. Furthermore, low energy availability in the ps-probe pulse causes an overall drop-in signal-to-noise ratios. As such, an all diode pumped Nd:YAG narrowband spectral amplifier was designed and characterized to generate a time synchronized ps-probe for hybrid fs/ps rotational CARS. The 800 $\mu\text{J}/\text{pulse}$, 1.9 cm^{-1} , 10 ps and the 400 $\mu\text{J}/\text{pulse}$, 3.3 cm^{-1} , 5.3 ps nearly transform-limited pulses produced were each used as a probe pulse in a two-beam rotational CARS arrangement at temperatures up to $\sim 2400\text{K}$. Excellent spatial, spectral, and temporal beam quality allowed for fitting the theoretical spectra with a simple Gaussian model for the probe pulse with temperature accuracies of 1-2%. From characterization data of the designed amplifier, this flexible single-mode probe-pulse has the potential for high-resolution CARS measurements in low number density situations, high-pressure flame environments, or improving sensitivity for single-laser-shot measurements at higher repetition rates.

7.2 Directions for future work

This dissertation experimentally validates the application of ultrafast nonlinear techniques in high-pressure reacting flows. The experiments were primarily carried out in well-calibrated laminar flames with known flames at chemical equilibrium. The next logical step would be to apply these calibrated schemes in advanced propulsion systems including next generation gas turbine combustors, hypersonic vehicles, rotating detonating combustors (RDCs), scramjet engines, etc. A few specific research objectives are mentioned below:

1. Rotating detonation combustors (RDCs) in rotating detonation engines (RDEs):
 - a. Measurement of H- and O-atom concentrations in a rotating detonation combustor for evaluation of combustion kinetics in the detonation prefill zones and detonation wake zones.

- b. Measurement of CO concentration in a CH_4/O_2 RDC for evaluation of combustion efficiency.
 - c. The picosecond-probe pulse designed in this dissertation can be used for hybrid fs/ps rotational CARS to measure static temperature in air-breathing RDCs. This information is highly valuable for comparing the inlet temperature for the downstream components of the RDC and provide insight into how close one could get in achieving the benefits of pressure gain combustion in practical systems.
2. High-speed hybrid fs/ps rotational CARS thermometry in a post-detonation fireball to provide validation data for multiphase, turbulent combustion models.
 3. Find the feasibility of high-pressure fs TP-LIF by evaluating absorption of excitation UV beam, beam defocusing and fluorescence signal trapping at pressures exceeding 50 atm. From the observation of this dissertation at these pressures absorption of UV radiation is predicted to be the limiting factor for any quantitative measurement of fs TP-LIF.
 4. The observation of 2+1 photoionization process in high-pressure fs CO TP-LIF could be extended as an independent detection scheme for CO.
 5. Development of more accurate collisional and spectral line-mixing models for the application of hybrid fs/ps vibrational CARS at pressures relevant to practical propulsion systems.
 6. The picosecond probe pulse designed in this dissertation can be used for a multitude of applications, such as thermometry using rotational CARS in above 50 atm pressure flames to determine the limit of collision independence of rotational hybrid fs/ps CARS thermometry, and potentially single-shot line measurements.

APPENDIX A. MOLECULAR CONSTANTS AND FITTING PARAMETERS FOR N₂ CARS MODEL

Term	Value	Unit	Ref.
ω_e	2358.57	cm ⁻¹	[182, 183]
$\omega_e x_e$	14.324	cm ⁻¹	
$\omega_e y_e$	-5.92949×10 ⁻³	cm ⁻¹	
$\omega_e z_e$	-2.4×10 ⁻⁴	cm ⁻¹	
B_e	1.99824	cm ⁻¹	
α_e	1.7318×10 ⁻²	cm ⁻¹	
γ_e	-3.1536099×10 ⁻⁵	cm ⁻¹	
D_e	5.76×10 ⁻⁶	cm ⁻¹	
δ_e	0	cm ⁻¹	
β_e	1.55×10 ⁻⁸	cm ⁻¹	
a'	0.581	cm ³	[102]
γ'	0.6675	cm ³	[102]
a_1	-2.7	—	[102]
$(p_2/p_1)_{iso}$	0.31	—	[101]
$(p_2/p_1)_{aniso}$	0.57	—	[101]
$(p_1/p_0)_{aniso}$	3.1687	—	[184]
α	0.02	cm ⁻¹ atm ⁻¹	[45, 88]
β	1.67	—	[45, 185]
δ	1.21	—	[45, 185]
n	0.5	—	[186]
m	0.1487	—	[45, 185]
a	1.5	—	[60]

REFERENCES

- [1] J. A. Miller, M. J. Pilling, and J. Troe, "Unravelling combustion mechanisms through a quantitative understanding of elementary reactions," *Proc. Combust. Inst.* **30**, 43-88 (2005).
- [2] T. Poinso, S. Candel, and A. Trouvé, "Applications of direct numerical simulation to premixed turbulent combustion," *Prog. Energy Combust. Sci.* **21**, 531-576 (1995).
- [3] C. K. Law, "Propagation, structure, and limit phenomena of laminar flames at elevated pressures," *Combustion science and technology* **178**, 335-360 (2006).
- [4] S. R. Turns, *An introduction to combustion* (McGraw-hill New York, 1996), Vol. 499.
- [5] S. M. Correa, "A review of NO_x formation under gas-turbine combustion conditions," *Combustion science and technology* **87**, 329-362 (1993).
- [6] I. Glassman, R. A. Yetter, and N. G. Glumac, *Combustion* (Academic press, 2014).
- [7] A. C. Eckbreth, *Laser diagnostics for combustion temperature and species* (CRC Press, 1996), Vol. 3.
- [8] J. R. Gord, T. R. Meyer, and S. Roy, "Applications of ultrafast lasers for optical measurements in combusting flows," (2008).
- [9] S. Roy, J. R. Gord, and A. K. Patnaik, "Recent advances in coherent anti-Stokes Raman scattering spectroscopy: Fundamental developments and applications in reacting flows," *Prog. Energy Combust. Sci.* **36**, 280-306 (2010).
- [10] R. Trebino, *Frequency-resolved optical gating: the measurement of ultrashort laser pulses* (Springer Science & Business Media, 2012).
- [11] M. Pessot, P. Maine, and G. Mourou, "1000 times expansion/compression of optical pulses for chirped pulse amplification," *Opt. Commun.* **62**, 419-421 (1987).
- [12] P. Maine, D. Strickland, P. Bado, M. Pessot, and G. Mourou, "Generation of ultrahigh peak power pulses by chirped pulse amplification," *IEEE Journal of Quantum electronics* **24**, 398-403 (1988).
- [13] G. Vaillancourt, T. Norris, J. S. Coe, P. Bado, and G. Mourou, "Operation of a 1-kHz pulse-pumped Ti: sapphire regenerative amplifier," *Opt. Lett.* **15**, 317-319 (1990).
- [14] J. D. Kafka, M. L. Watts, and J.-W. Pieterse, "Picosecond and femtosecond pulse generation in a regeneratively mode-locked Ti: sapphire laser," *IEEE journal of quantum electronics* **28**, 2151-2162 (1992).

- [15] S. Backus, C. G. Durfee III, M. M. Murnane, and H. C. Kapteyn, "High power ultrafast lasers," *Review of scientific instruments* **69**, 1207-1223 (1998).
- [16] C. Rulliere, *Femtosecond laser pulses* (Springer, 2005).
- [17] A. Weiner, *Ultrafast optics* (John Wiley & Sons, 2011), Vol. 72.
- [18] X. Gu, S. Akturk, and R. Trebino, "Spatial chirp in ultrafast optics," *Opt. Commun.* **242**, 599-604 (2004).
- [19] J. W. Daily, "Laser induced fluorescence spectroscopy in flames," *Prog. Energy Combust. Sci.* **23**, 133-199 (1997).
- [20] W. G. Bessler, C. Schulz, T. Lee, J. B. Jeffries, and R. K. Hanson, "Strategies for laser-induced fluorescence detection of nitric oxide in high-pressure flames. I. A–Xexcitation," *Appl. Opt.* **41**, 3547-3557 (2002).
- [21] M. Versluis, N. Georgiev, L. Martinsson, M. Aldén, and S. Kröll, "2-D absolute OH concentration profiles in atmospheric flames using planar LIF in a bi-directional laser beam configuration," *Applied Physics B: Lasers and Optics* **65**, 411-417 (1997).
- [22] R. K. Hanson, "Combustion diagnostics: planar imaging techniques," in *Symposium (International) on Combustion*, (Elsevier, 1988), 1677-1691.
- [23] D. Zhang, Q. Gao, B. Li, J. Liu, and Z. Li, "Instantaneous one-dimensional ammonia measurements with femtosecond two-photon laser-induced fluorescence (fs-TPLIF)," *International Journal of Hydrogen Energy* **44**, 25740-25745 (2019).
- [24] M. S. Pindzola, "Two-photon excitation of atomic oxygen," *Phys. Rev. A* **17**, 1021-1027 (1978).
- [25] W. K. Bischel, B. E. Perry, and D. R. Crosley, "Two-photon laser-induced fluorescence in oxygen and nitrogen atoms," *Chem. Phys. Lett.* **82**, 85-88 (1981).
- [26] D. R. Crosley, "Collisional Effects On Laser-Induced Fluorescence Flame Measurements," *Opt. Eng.* **20**, 204511-204511- (1981).
- [27] R. P. Lucht, J. T. Salmon, G. B. King, D. W. Sweeney, and N. M. Laurendeau, "Two-photon-excited fluorescence measurement of hydrogen atoms in flames," *Opt. Lett.* **8**, 365-367 (1983).
- [28] J. E. M. Goldsmith and N. M. Laurendeau, "Two-photon-excited fluorescence measurements of OH concentration in a hydrogen–oxygen flame," *Appl. Opt.* **25**, 276-283 (1986).

- [29] J. Haumann, J. M. Seitzman, and R. K. Hanson, "Two-photon digital imaging of CO in combustion flows using planar laser-induced fluorescence," *Opt. Lett.* **11**, 776-778 (1986).
- [30] W. D. Kulatilaka, J. R. Gord, V. R. Katta, and S. Roy, "Photolytic-interference-free, femtosecond two-photon fluorescence imaging of atomic hydrogen," *Opt. Lett.* **37**, 3051-3053 (2012).
- [31] W. D. Kulatilaka, S. Roy, N. Jiang, and J. R. Gord, "Photolytic-interference-free, femtosecond, two-photon laser-induced fluorescence imaging of atomic oxygen in flames," *Appl. Phys. B* **122**, 26 (2016).
- [32] J. B. Schmidt, S. Roy, W. D. Kulatilaka, I. Shkurenkov, I. V. Adamovich, W. R. Lempert, and J. R. Gord, "Femtosecond, two-photon-absorption, laser-induced-fluorescence (fs-TALIF) imaging of atomic hydrogen and oxygen in non-equilibrium plasmas," *J. Phys. D: Appl. Phys.* **50**, 015204 (2016).
- [33] D. R. Richardson, S. Roy, and J. R. Gord, "Femtosecond, two-photon, planar laser-induced fluorescence of carbon monoxide in flames," *Opt. Lett.* **42**, 875-878 (2017).
- [34] S. F. Adams and T. A. Miller, "Two-photon absorption laser-induced fluorescence of atomic nitrogen by an alternative excitation scheme," *Chem. Phys. Lett.* **295**, 305-311 (1998).
- [35] H. U. Stauffer, W. D. Kulatilaka, J. R. Gord, and S. Roy, "Laser-induced fluorescence detection of hydroxyl (OH) radical by femtosecond excitation," *Opt. Lett.* **36**, 1776-1778 (2011).
- [36] J. D. Miller, M. Slipchenko, T. R. Meyer, N. Jiang, W. R. Lempert, and J. R. Gord, "Ultrahigh-frame-rate OH fluorescence imaging in turbulent flames using a burst-mode optical parametric oscillator," *Opt. Lett.* **34**, 1309-1311 (2009).
- [37] A. C. Eckbreth, "BOXCARS: Crossed-beam phase-matched CARS generation in gases," *Appl. Phys. Lett.* **32**, 421-423 (1978).
- [38] A. C. Eckbreth, "CARS thermometry in practical combustors," *Combust. Flame* **39**, 133-147 (1980).
- [39] S. Linow, A. Dreizler, J. Janicka, and E. P. Hassel, "Comparison of two-photon excitation schemes for CO detection in flames," *Appl. Phys. B* **71**, 689-696 (2000).
- [40] J. Rosell, J. Sjöholm, M. Richter, and M. Aldén, "Comparison of Three Schemes of Two-Photon Laser-Induced Fluorescence for CO Detection in Flames," *Appl. Spectrosc.* **67**, 314-320 (2013).

- [41] C. Dumitrache, A. Gallant, G.-D. Stancu, and C. O. Laux, "Femtosecond Two-Photon Absorption Laser Induced Fluorescence (fs-TALIF) Imaging of Atomic Nitrogen in Nanosecond Repetitive Discharges," in *AIAA Scitech 2019 Forum*, 2019), 1507.
- [42] G. Clark and R. L. Farrow, "The CARSFT code: user and programmer information," Sandia National Laboratories **26**(1990).
- [43] G. Alessandretti and P. Violino, "Thermometry by CARS in an automobile engine," J. Phys. D: Appl. Phys. **16**, 1583 (1983).
- [44] R. J. Hall, J. F. Verdick, and A. C. Eckbreth, "Pressure-induced narrowing of the CARS spectrum of N₂," Opt. Commun. **35**, 69-75 (1980).
- [45] L. Rahn and R. E. Palmer, "Studies of nitrogen self-broadening at high temperature with inverse Raman spectroscopy," J. Opt. Soc. Am. B **3**, 1164-1169 (1986).
- [46] J. Bonamy, L. Bonamy, D. Robert, M. L. Gonze, G. Millot, B. Lavorel, and H. Berger, "Rotational relaxation of nitrogen in ternary mixtures N₂ –CO₂ –H₂O: Consequences in coherent anti-Stokes Raman spectroscopy thermometry," J. Chem. Phys. **94**, 6584-6589 (1991).
- [47] L. Martinsson, P. E. Bengtsson, M. Aldén, S. Kröll, and J. Bonamy, "A test of different rotational Raman linewidth models: Accuracy of rotational coherent anti-Stokes Raman scattering thermometry in nitrogen from 295 to 1850 K," J. Chem. Phys. **99**, 2466-2477 (1993).
- [48] W. Stricker, M. Woyde, R. Lückcrath, and V. Bergmann, "Temperature measurements in high pressure combustion," Berichte der Bunsengesellschaft für physikalische Chemie **97**, 1608-1618 (1993).
- [49] A. C. Eckbreth and T. J. Anderson, "Dual broadband CARS for simultaneous, multiple species measurements," Appl. Opt. **24**, 2731-2736 (1985).
- [50] P.-E. Bengtsson, L. Martinsson, and M. Aldén, "Combined vibrational and rotational CARS for simultaneous measurements of temperature and concentrations of fuel, oxygen, and nitrogen," Appl. Spectrosc. **49**, 188-192 (1995).
- [51] R. P. Lucht, "Three-laser coherent anti-Stokes Raman scattering measurements of two species," Opt. Lett. **12**, 78-80 (1987).
- [52] G. Magnotti, A. D. Cutler, and P. M. Danehy, "Development of a dual-pump coherent anti-Stokes Raman spectroscopy system for measurements in supersonic combustion," Appl. Opt. **52**, 4779-4791 (2013).

- [53] S. O'Byrne, P. M. Danehy, A. D. Cutler, and S. Tedder, "Dual-pump coherent anti-Stokes Raman scattering measurements in a supersonic combustor," *AIAA journal* **45**, 922-933 (2007).
- [54] A. D. Cutler, G. Magnotti, L. Cantu, E. Gallo, R. Rockwell, and C. Goyne, "Dual-pump coherent anti-stokes raman spectroscopy measurements in a dual-mode scramjet," *Journal of Propulsion and Power* **30**, 539-549 (2014).
- [55] A. Satija and R. P. Lucht, "Development of a combined pure rotational and vibrational coherent anti-Stokes Raman scattering system," *Opt. Lett.* **38**, 1340-1342 (2013).
- [56] S. Roy, T. R. Meyer, M. S. Brown, V. N. Velur, R. P. Lucht, and J. R. Gord, "Triple-pump coherent anti-Stokes Raman scattering (CARS): temperature and multiple-species concentration measurements in reacting flows," *Opt. Commun.* **224**, 131-137 (2003).
- [57] S. A. Tedder, J. L. Wheeler, A. D. Cutler, and P. M. Danehy, "Width-increased dual-pump enhanced coherent anti-Stokes Raman spectroscopy," *Appl. Opt.* **49**, 1305-1313 (2010).
- [58] G. Magnotti, A. D. Cutler, G. Herring, S. A. Tedder, and P. M. Danehy, "Saturation and Stark broadening effects in dual-pump CARS of N₂, O₂, and H₂," *J. Raman Spectrosc.* **43**, 611-620 (2012).
- [59] A. D. Cutler, L. M. Cantu, E. C. Gallo, R. Baurle, P. M. Danehy, R. Rockwell, C. Goyne, and J. McDaniel, "Nonequilibrium supersonic freestream studied using coherent anti-Stokes Raman spectroscopy," *AIAA Journal* **53**, 2762-2770 (2015).
- [60] T. Seeger, F. Beyrau, A. Bräuer, and A. Leipertz, "High-pressure pure rotational CARS: comparison of temperature measurements with O₂, N₂ and synthetic air," *J. Raman Spectrosc.* **34**, 932-939 (2003).
- [61] A. C. Eckbreth and R. J. Hall, "CARS concentration sensitivity with and without nonresonant background suppression," (1981).
- [62] S. Roy, T. R. Meyer, and J. R. Gord, "Time-resolved dynamics of resonant and nonresonant broadband picosecond coherent anti-Stokes Raman scattering signals," *Appl. Phys. Lett.* **87**, 264103 (2005).
- [63] T. R. Meyer, S. Roy, and J. R. Gord, "Improving signal-to-interference ratio in rich hydrocarbon-air flames using picosecond coherent anti-Stokes Raman scattering," *Appl. Spectrosc.* **61**, 1135-1140 (2007).
- [64] S. Roy, P. S. Hsu, N. Jiang, M. N. Slipchenko, and J. R. Gord, "100-kHz-rate gas-phase thermometry using 100-ps pulses from a burst-mode laser," *Opt. Lett.* **40**, 5125-5128 (2015).

- [65] T. Seeger, J. Kiefer, A. Leipertz, B. D. Patterson, C. J. Kliewer, and T. B. Settersten, "Picosecond time-resolved pure-rotational coherent anti-Stokes Raman spectroscopy for N₂ thermometry," *Opt. Lett.* **34**, 3755-3757 (2009).
- [66] S. Roy, T. R. Meyer, and J. R. Gord, "Broadband coherent anti-Stokes Raman scattering spectroscopy of nitrogen using a picosecond modeless dye laser," *Opt. Lett.* **30**, 3222-3224 (2005).
- [67] T. Lang and M. Motzkus, "Single-shot femtosecond coherent anti-Stokes Raman-scattering thermometry," *J. Opt. Soc. Am. B* **19**, 340-344 (2002).
- [68] S. Roy, W. D. Kulatilaka, D. R. Richardson, R. P. Lucht, and J. R. Gord, "Gas-phase single-shot thermometry at 1 kHz using fs-CARS spectroscopy," *Opt. Lett.* **34**, 3857-3859 (2009).
- [69] M. Dantus, R. Bowman, and A. Zewail, "Femtosecond laser observations of molecular vibration and rotation," *Nature* **343**, 737 (1990).
- [70] R. P. Lucht, S. Roy, T. R. Meyer, and J. R. Gord, "Femtosecond coherent anti-Stokes Raman scattering measurement of gas temperatures from frequency-spread dephasing of the Raman coherence," *Appl. Phys. Lett.* **89**, 251112 (2006).
- [71] P. Beaud, H.-M. Frey, T. Lang, and M. Motzkus, "Flame thermometry by femtosecond CARS," *Chem. Phys. Lett.* **344**, 407-412 (2001).
- [72] B. Lavorel, H. Tran, E. Hertz, O. Faucher, P. Joubert, M. Motzkus, T. Buckup, T. Lang, H. Skenderovi, and G. Knopp, "Femtosecond Raman time-resolved molecular spectroscopy," *Comptes Rendus Physique* **5**, 215-229 (2004).
- [73] P. J. Wrzesinski, H. U. Stauffer, W. D. Kulatilaka, J. R. Gord, and S. Roy, "Time-resolved femtosecond CARS from 10 to 50 Bar: collisional sensitivity," *J. Raman Spectrosc.* **44**, 1344-1348 (2013).
- [74] D. R. Richardson, R. P. Lucht, W. D. Kulatilaka, S. Roy, and J. R. Gord, "Chirped-probe-pulse femtosecond coherent anti-Stokes Raman scattering concentration measurements," *J. Opt. Soc. Am. B* **30**, 188-196 (2013).
- [75] C. N. Dennis, A. Satija, and R. P. Lucht, "High dynamic range thermometry at 5 kHz in hydrogen-air diffusion flame using chirped-probe-pulse femtosecond coherent anti-stokes Raman scattering," *J. Raman Spectrosc.* **47**, 177-188 (2016).
- [76] D. Richardson, R. Lucht, W. Kulatilaka, S. Roy, and J. R. Gord, "Theoretical modeling of single-laser-shot, chirped-probe-pulse femtosecond coherent anti-Stokes Raman scattering thermometry," *Appl. Phys. B* **104**, 699 (2011).

- [77] D. R. Richardson, H. U. Stauffer, S. Roy, and J. R. Gord, "Comparison of chirped-probe-pulse and hybrid femtosecond/picosecond coherent anti-Stokes Raman scattering for combustion thermometry," *Appl. Opt.* **56**, E37-E49 (2017).
- [78] B. D. Prince, A. Chakraborty, B. M. Prince, and H. U. Stauffer, "Development of simultaneous frequency-and time-resolved coherent anti-Stokes Raman scattering for ultrafast detection of molecular Raman spectra," *J. Chem. Phys.* **125**, 044502 (2006).
- [79] D. Pestov, R. K. Murawski, G. O. Ariunbold, X. Wang, M. Zhi, A. V. Sokolov, V. A. Sautenkov, Y. V. Rostovtsev, A. Dogariu, and Y. Huang, "Optimizing the laser-pulse configuration for coherent Raman spectroscopy," *science* **316**, 265-268 (2007).
- [80] D. Pestov, X. Wang, D. Cristancho, K. R. Hall, A. V. Sokolov, and M. O. Scully, "Real-time sensing of gas phase mixtures via coherent Raman spectroscopy," in *2008 Conference on Lasers and Electro-Optics and 2008 Conference on Quantum Electronics and Laser Science*, (IEEE, 2008), 1-2.
- [81] H. U. Stauffer, J. D. Miller, S. Roy, J. R. Gord, and T. R. Meyer, "Communication: Hybrid femtosecond/picosecond rotational coherent anti-Stokes Raman scattering thermometry using a narrowband time-asymmetric probe pulse," *J. Chem. Phys.* **136**, 111101 (2012).
- [82] C. E. Dedic, J. B. Michael, J. D. Miller, and T. R. Meyer, "Evaluation of hybrid fs/ps coherent anti-Stokes Raman scattering temperature and pressure sensitivity at combustor relevant conditions," in *54th AIAA Aerospace Sciences Meeting*, (2016), 0284.
- [83] A. Bohlin and C. J. Kliewer, "Two-beam ultrabroadband coherent anti-Stokes Raman spectroscopy for high resolution gas-phase multiplex imaging," *Appl. Phys. Lett.* **104**, 031107 (2014).
- [84] A. Bohlin, B. D. Patterson, and C. J. Kliewer, "Communication: Simplified two-beam rotational CARS signal generation demonstrated in 1D," *J. Chem. Phys.* **138**, 081102 (2013).
- [85] A. Bohlin, M. Mann, B. D. Patterson, A. Dreizler, and C. J. Kliewer, "Development of two-beam femtosecond/picosecond one-dimensional rotational coherent anti-Stokes Raman spectroscopy: time-resolved probing of flame wall interactions," *Proc. Combust. Inst.* **35**, 3723-3730 (2015).
- [86] A. Bohlin and C. J. Kliewer, "Communication: Two-dimensional gas-phase coherent anti-Stokes Raman spectroscopy (2D-CARS): Simultaneous planar imaging and multiplex spectroscopy in a single laser shot," *J. Chem. Phys.* **138**, 221101 (2013).
- [87] J. D. Miller, M. N. Slipchenko, J. G. Mance, S. Roy, and J. R. Gord, "1-kHz two-dimensional coherent anti-Stokes Raman scattering (2D-CARS) for gas-phase thermometry," *Opt. Express* **24**, 24971-24979 (2016).

- [88] J. D. Miller, M. N. Slipchenko, T. R. Meyer, H. U. Stauffer, and J. R. Gord, "Hybrid femtosecond/picosecond coherent anti-Stokes Raman scattering for high-speed gas-phase thermometry," *Opt. Lett.* **35**, 2430-2432 (2010).
- [89] J. D. Miller, C. E. Dedic, and T. R. Meyer, "Vibrational femtosecond/picosecond coherent anti-Stokes Raman scattering with enhanced temperature sensitivity for flame thermometry from 300 to 2400 K," *J. Raman Spectrosc.* **46**, 702-707 (2015).
- [90] J. D. Miller, M. N. Slipchenko, and T. R. Meyer, "Probe-pulse optimization for nonresonant suppression in hybrid fs/ps coherent anti-Stokes Raman scattering at high temperature," *Opt. Express* **19**, 13326-13333 (2011).
- [91] S. P. Kearney, D. J. Scoglietti, and C. J. Kliewer, "Hybrid femtosecond/picosecond rotational coherent anti-Stokes Raman scattering temperature and concentration measurements using two different picosecond-duration probes," *Opt. Express* **21**, 12327-12339 (2013).
- [92] M. Scherman, M. Nafa, T. Schmid, A. Godard, A. Bresson, B. Attal-Tretout, and P. Joubert, "Rovibrational hybrid fs/ps CARS using a volume Bragg grating for N₂ thermometry," *Opt. Lett.* **41**, 488-491 (2016).
- [93] F. Raoult, A. Boscheron, D. Husson, C. Sauteret, A. Modena, V. Malka, F. Dorchies, and A. Migus, "Efficient generation of narrow-bandwidth picosecond pulses by frequency doubling of femtosecond chirped pulses," *Opt. Lett.* **23**, 1117-1119 (1998).
- [94] S. P. Kearney and D. J. Scoglietti, "Hybrid femtosecond/picosecond rotational coherent anti-Stokes Raman scattering at flame temperatures using a second-harmonic bandwidth-compressed probe," *Opt. Lett.* **38**, 833-835 (2013).
- [95] S. P. Kearney, "Hybrid fs/ps rotational CARS temperature and oxygen measurements in the product gases of canonical flat flames," *Combust. Flame* **162**, 1748-1758 (2015).
- [96] C. E. Dedic, T. R. Meyer, and J. B. Michael, "Single-shot ultrafast coherent anti-Stokes Raman scattering of vibrational/rotational nonequilibrium," *Optica* **4**, 563-570 (2017).
- [97] T. L. Courtney, N. T. Mecker, B. D. Patterson, M. Linne, and C. J. Kliewer, "Hybrid femtosecond/picosecond pure rotational anti-Stokes Raman spectroscopy of nitrogen at high pressures (1–70 atm) and temperatures (300–1000 K)," *Appl. Phys. Lett.* **114**, 101107 (2019).
- [98] S. Mukamel, *Principles of nonlinear optical spectroscopy* (Oxford university press New York, 1995), Vol. 29.

- [99] H. U. Stauffer, J. D. Miller, M. N. Slipchenko, T. R. Meyer, B. D. Prince, S. Roy, and J. R. Gord, "Time- and frequency-dependent model of time-resolved coherent anti-Stokes Raman scattering (CARS) with a picosecond-duration probe pulse," *J. Chem. Phys.* **140**, 024316 (2014).
- [100] N. M. Laurendeau, *Statistical thermodynamics: fundamentals and applications* (Cambridge University Press, 2005).
- [101] M. Marrocco, "Comparative analysis of Herman-Wallis factors for uses in coherent anti-Stokes Raman spectra of light molecules," *J. Raman Spectrosc.* **40**, 741-747 (2009).
- [102] M. A. Buldakov, V. N. Cherepanov, B. V. Korolev, and I. I. Matrosov, "Role of intramolecular interactions in Raman spectra of N₂ and O₂ molecules," *Journal of Molecular Spectroscopy* **217**, 1-8 (2003).
- [103] G. Placzek and E. Teller, "Die Rotationsstruktur der Ramanbanden mehratomiger Moleküle," *Zeitschrift für Physik* **81**, 209-258 (1933).
- [104] A. Bohlin, P. E. Bengtsson, and M. Marrocco, "On the sensitivity of rotational CARS N₂ thermometry to the Herman-Wallis factor," *J. Raman Spectrosc.* **42**, 1843-1847 (2011).
- [105] R. Tipping and J. Ogilvie, "Herman-wallis factors for Raman transitions of ¹Σ-state diatomic molecules," *J. Raman Spectrosc.* **15**, 38-40 (1984).
- [106] M. Koszykowski, L. Rahn, R. Palmer, and M. Coltrin, "Theoretical and experimental studies of high-resolution inverse Raman spectra of molecular nitrogen at 1-10 atm," *Journal of Physical Chemistry* **91**, 41-46 (1987).
- [107] C. Kliewer, A. Bohlin, E. Nordström, B. Patterson, P.-E. Bengtsson, and T. Settersten, "Time-domain measurements of S-branch N₂-N₂ Raman linewidths using picosecond pure rotational coherent anti-Stokes Raman spectroscopy," *Appl. Phys. B* **108**, 419-426 (2012).
- [108] L. A. Rahn, R. Farrow, and G. Rosasco, "Measurement of the self-broadening of the H₂ Q (0-5) Raman transitions from 295 to 1000 K," *Phys. Rev. A* **43**, 6075 (1991).
- [109] G. Millot, R. Saint-Loup, J. Santos, R. Chaux, H. Berger, and J. Bonamy, "Collisional effects in the stimulated Raman Q branch of O₂ and O₂-N₂," *J. Chem. Phys.* **96**, 961-971 (1992).
- [110] F. Beyrau, A. Datta, T. Seeger, and A. Leipertz, "Dual-pump CARS for the simultaneous detection of N₂, O₂ and CO in CH₄ flames," *J. Raman Spectrosc.* **33**, 919-924 (2002).
- [111] G. Knopp, P. Beaud, P. Radi, M. Tulej, B. Bougie, D. Cannavo, and T. Gerber, "Pressure-dependent N₂ Q-branch fs-CARS measurements," *J. Raman Spectrosc.* **33**, 861-865 (2002).

- [112] J. D. Miller, S. Roy, J. R. Gord, and T. R. Meyer, "Communication: Time-domain measurement of high-pressure N₂ and O₂ self-broadened linewidths using hybrid femtosecond/picosecond coherent anti-Stokes Raman scattering," *J. Chem. Phys.* **135**, 201104 (2011).
- [113] M. Woyde and W. Stricker, "The application of CARS for temperature measurements in high pressure combustion systems," *Appl. Phys. B* **50**, 519-525 (1990).
- [114] M. Afzeli, C. Brackmann, F. Vestin, and P.-E. Bengtsson, "Pure rotational coherent anti-Stokes Raman spectroscopy in mixtures of CO and N₂," *Appl. Opt.* **43**, 6664-6672 (2004).
- [115] S. Roy, D. Richardson, P. J. Kinnius, R. P. Lucht, and J. R. Gord, "Effects of N₂ – CO polarization beating on femtosecond coherent anti-Stokes Raman scattering spectroscopy of N₂," *Appl. Phys. Lett.* **94**(2009).
- [116] J. Wang, M. Maiorov, D. S. Baer, D. Z. Garbuzov, J. C. Connolly, and R. K. Hanson, "In situ combustion measurements of CO with diode-laser absorption near 2.3 μ m," *Appl. Opt.* **39**, 5579-5589 (2000).
- [117] J. Baker, J. Lemaire, S. Couris, A. Vient, D. Malmasson, and F. Rostas, "A 2+ 1 REMPI study of the *EX* transition in CO. Indirect predissociations in the *E'¹ Π* state," *Chemical physics* **178**, 569-579 (1993).
- [118] A. Masri, R. Dibble, and R. Barlow, "Raman-Rayleigh scattering measurements in reacting and non-reacting dilute two-phase flows," *J. Raman Spectrosc.* **24**, 83-89 (1993).
- [119] N. Georgiev, K. Nyholm, R. Fritzon, and M. Aldén, "Developments of the amplified stimulated emission technique for spatially resolved species detection in flames," *Opt. Commun.* **108**, 71-76 (1994).
- [120] U. Westblom, S. Agrup, M. Aldén, H. M. Hertz, and J. E. M. Goldsmith, "Properties of laser-induced stimulated emission for diagnostic purposes," *Appl. Phys. B* **50**, 487-497 (1990).
- [121] G. Hancock and H. Zacharias, "Laser-induced fluorescence from CO(*A'¹ Π*)," *Chem. Phys. Lett.* **82**, 402-404 (1981).
- [122] A. Mokhov, H. Levinsky, C. Van der Meij, and R. Jacobs, "Analysis of laser-induced-fluorescence carbon monoxide measurements in turbulent nonpremixed flames," *Appl. Opt.* **34**, 7074-7082 (1995).
- [123] M. Aldén, H. M. Hertz, S. Svanberg, and S. Wallin, "Imaging laser-induced fluorescence of oxygen atoms in a flame," *Appl. Opt.* **23**, 3255-3257 (1984).
- [124] K. Kohse-Höinghaus, "Laser techniques for the quantitative detection of reactive intermediates in combustion systems," *Prog. Energy Combust. Sci.* **20**, 203-279 (1994).

- [125] M. Aldén, H. Edner, P. Grafström, and S. Svanberg, "Two-photon excitation of atomic oxygen in a flame," *Opt. Commun.* **42**, 244-246 (1982).
- [126] J. M. Seitzman, J. Haumann, and R. K. Hanson, "Quantitative two-photon LIF imaging of carbon monoxide in combustion gases," *Appl. Opt.* **26**, 2892-2899 (1987).
- [127] T. B. Settersten, A. Dreizler, and R. L. Farrow, "Temperature- and species-dependent quenching of CO B probed by two-photon laser-induced fluorescence using a picosecond laser," *J. Chem. Phys.* **117**, 3173-3179 (2002).
- [128] M. Richter, Z. S. Li, and M. Aldén, "Application of two-photon laser-induced fluorescence for single-shot visualization of carbon monoxide in a spark ignited engine," *Appl. Spectrosc.* **61**, 1-5 (2007).
- [129] D. R. Richardson, N. Jiang, D. L. Blunck, J. R. Gord, and S. Roy, "Characterization of inverse diffusion flames in vitiated cross flows via two-photon planar laser-induced fluorescence of CO and 2-D thermometry," *Combust. Flame* **168**, 270-285 (2016).
- [130] M. D. Di Rosa and R. L. Farrow, "Temperature-dependent collisional broadening and shift of Q-branch transitions in the $B \leftarrow X(0, 0)$ band of CO perturbed by N₂, CO₂ and CO," *J. Spectrosc. Radiat. Transfer.* **68**, 363-375 (2001).
- [131] A. P. Nefedov, V. A. Sinel'shchikov, A. D. Usachev, and A. V. Zobnin, "Photochemical effect in two-photon laser-induced fluorescence detection of carbon monoxide in hydrocarbon flames," *Appl. Opt.* **37**, 7729-7736 (1998).
- [132] C. Brackmann, J. Sjöholm, J. Rosell, M. Richter, J. Bood, and M. Aldén, "Picosecond excitation for reduction of photolytic effects in two-photon laser-induced fluorescence of CO," *Proc. Combust. Inst.* **34**, 3541-3548 (2013).
- [133] B. Li, X. Li, D. Zhang, Q. Gao, M. Yao, and Z. Li, "Comprehensive CO detection in flames using femtosecond two-photon laser-induced fluorescence," *Opt. Express* **25**, 25809-25818 (2017).
- [134] M. D. Di Rosa and R. L. Farrow, "Two-photon excitation cross section of the $B \leftarrow X(0, 0)$ band of CO measured by direct absorption," *J. Opt. Soc. Am. B* **16**, 1988-1994 (1999).
- [135] M. Lino da Silva and M. Dudeck, "Arrays of radiative transition probabilities for CO₂-N₂ plasmas," *J. Spectrosc. Radiat. Transfer.* **102**, 348-386 (2006).
- [136] M. Di Rosa and R. Farrow, "Cross sections of photoionization and ac Stark shift measured from Doppler-free $B \leftarrow X(0, 0)$ excitation spectra of CO," *J. Opt. Soc. Am. B* **16**, 861-870 (1999).

- [137] R. D. Hancock, K. E. Bertagnolli, and R. P. Lucht, "Nitrogen and hydrogen CARS temperature measurements in a hydrogen/air flame using a near-adiabatic flat-flame burner," *Combust. Flame* **109**, 323-331 (1997).
- [138] T. Ombrello, C. Carter, and V. Katta, "Burner platform for sub-atmospheric pressure flame studies," *Combust. Flame* **159**, 2363-2373 (2012).
- [139] F. Kong, Q. Luo, H. Xu, M. Sharifi, D. Song, and S. L. Chin, "Explosive photodissociation of methane induced by ultrafast intense laser," *J. Chem. Phys.* **125**, 133320 (2006).
- [140] Y. Wang and W. D. Kulatilaka, "Spectroscopic investigation of high-pressure femtosecond two-photon laser-induced fluorescence of carbon monoxide up to 20 bar," *Appl. Opt.* **58**, C23-C29 (2019).
- [141] K. A. Rahman, K. S. Patel, M. N. Slipchenko, T. R. Meyer, Z. Zhang, Y. Wu, J. R. Gord, and S. Roy, "Femtosecond, two-photon, laser-induced fluorescence (TP-LIF) measurement of CO in high-pressure flames," *Appl. Opt.* **57**, 5666-5671 (2018).
- [142] P. Ding, M. Ruchkina, Y. Liu, M. Alden, and J. Bood, "Femtosecond two-photon-excited backward lasing of atomic hydrogen in a flame," *Opt. Lett.* **43**, 1183-1186 (2018).
- [143] K. A. Rahman, V. Athmanathan, M. N. Slipchenko, S. Roy, J. R. Gord, Z. Zhang, and T. R. Meyer, "Quantitative femtosecond, two-photon laser-induced fluorescence of atomic oxygen in high-pressure flames," *Appl. Opt.* **58**, 1984-1990 (2019).
- [144] C. Schulz, J. Jeffries, D. Davidson, J. Koch, J. Wolfrum, and R. Hanson, "Impact of UV absorption by CO₂ and H₂O on NO LIF in high-pressure combustion applications," *Proc. Combust. Inst.* **29**, 2735-2742 (2002).
- [145] F. Di Teodoro and R. Farrow, "CO⁺ B² Σ⁺(v= 0) emission induced by laser excitation of neutral CO at 230 nm," *J. Chem. Phys.* **114**, 3421-3428 (2001).
- [146] A. Sharma, M. N. Slipchenko, M. N. Shneider, X. Wang, K. A. Rahman, and A. Shashurin, "Counting the electrons in a multiphoton ionization by elastic scattering of microwaves," *Sci. Rep.* **8**, 2874 (2018).
- [147] A. Sharma, M. Slipchenko, K. A. Rahman, A. Shashurin, and M. N. Shneider, "Absolutely Calibrated REMPI for Diagnostics of Small Neutral Gaseous Components in Mixtures," in *AIAA Scitech 2019 Forum*, (American Institute of Aeronautics and Astronautics, 2019), 0471.
- [148] H. Bergström, H. Lundberg, and A. Persson, "Investigations of stimulated emission on B-A lines in CO," *Z. Phys. D* **21**, 323-327 (1991).
- [149] J. J. Tiee, C. R. Q. Jr., G. W. Loge, and F. B. Wampler, "Two-photon pumped CO B-A laser," *J. Appl. Phys.* **63**, 288-290 (1988).

- [150] A. G. Gaydon and H. G. Wolfard, *Flames – their structure, radiation and temperature* (Chapman and Hall, London 1979).
- [151] G. Stancu, F. Kaddouri, D. Lacoste, and C. Laux, "Atmospheric pressure plasma diagnostics by OES, CRDS and TALIF," *J. Phys. D: Appl. Phys.* **43**, 124002 (2010).
- [152] P. Glarborg, "Hidden interactions—Trace species governing combustion and emissions," *Proc. Combust. Inst.* **31**, 77-98 (2007).
- [153] R. Barlow, G. Fiechtner, and J.-Y. Chen, "Oxygen atom concentrations and NO production rates in a turbulent H₂/N₂ jet flame," in *Symp. (Int.) Combust.*, (Elsevier, 1996), 2199-2205.
- [154] D. Schröder, H. Bahre, N. Knake, J. Winter, T. De Los Arcos, and V. Schulz-Von Der Gathen, "Influence of target surfaces on the atomic oxygen distribution in the effluent of a micro-scaled atmospheric pressure plasma jet," *Plasma Sources Sci. Technol.* **21**, 024007 (2012).
- [155] M. Uddi, N. Jiang, E. Mintusov, I. V. Adamovich, and W. R. Lempert, "Atomic oxygen measurements in air and air/fuel nanosecond pulse discharges by two photon laser induced fluorescence," *Proc. Combust. Inst.* **32**, 929-936 (2009).
- [156] C. J. Dasch and J. H. Bechtel, "Spontaneous Raman scattering by ground-state oxygen atoms," *Opt. Lett.* **6**, 36-38 (1981).
- [157] R. E. Teets and J. H. Bechtel, "Coherent anti-Stokes Raman spectra of oxygen atoms in flames," *Opt. Lett.* **6**, 458-460 (1981).
- [158] T. L. Chng and R. Miles, "Absolute concentration measurements of atomic oxygen in a flame using radar REMPI," in *52nd Aerospace Sciences Meeting*, (2014), 1360.
- [159] H. Döbele, T. Mosbach, K. Niemi, and V. Schulz-Von Der Gathen, "Laser-induced fluorescence measurements of absolute atomic densities: concepts and limitations," *Plasma Sources Sci. Technol.* **14**, S31 (2005).
- [160] A. van Gessel, S. van Grootel, and P. Bruggeman, "Atomic oxygen TALIF measurements in an atmospheric-pressure microwave plasma jet with in situ xenon calibration," *Plasma Sources Sci. Technol.* **22**, 055010 (2013).
- [161] J. E. Goldsmith, "Photochemical effects in two-photon-excited fluorescence detection of atomic oxygen in flames," *Appl. Opt.* **26**, 3566-3572 (1987).
- [162] J. Goldsmith and R. Anderson, "Laser-induced fluorescence spectroscopy and imaging of molecular oxygen in flames," *Opt. Lett.* **11**, 67-69 (1986).

- [163] M. Aldén, U. Westblom, and J. E. Goldsmith, "Two-photon-excited stimulated emission from atomic oxygen in flames and cold gases," *Opt. Lett.* **14**, 305 (1989).
- [164] D. J. Bamford, L. E. Jusinski, and W. K. Bischel, "Absolute two-photon absorption and three-photon ionization cross sections for atomic oxygen," *Phys. Rev. A* **34**, 185 (1986).
- [165] L. Gasnot, P. Desgroux, J. Pauwels, and L. Sochet, "Improvement of two-photon laser induced fluorescence measurements of H-and O-atoms in premixed methane/air flames," *Appl. Phys. B* **65**, 639-646 (1997).
- [166] J. Bittner, K. Kohse-Höinghaus, U. Meier, and T. Just, "Quenching of two-photon-excited H (3s, 3d) and O ($3p^3P_{2,1,0}$) atoms by rare gases and small molecules," *Chem. Phys. Lett.* **143**, 571-576 (1988).
- [167] J. H. Frank and T. B. Settersten, "Two-photon LIF imaging of atomic oxygen in flames with picosecond excitation," *Proc. Combust. Inst.* **30**, 1527-1534 (2005).
- [168] S. Zhang, A. Van Gessel, S. Van Grootel, and P. Bruggeman, "The effect of collisional quenching of the O $3p^3P_j$ state on the determination of the spatial distribution of the atomic oxygen density in an APPJ operating in ambient air by TALIF," *Plasma Sources Sci. Technol.* **23**, 025012 (2014).
- [169] D. Marinov, C. Drag, C. Blondel, O. Guaitella, J. Golda, B. Klarenaar, R. Engeln, V. Schulz-von der Gathen, and J.-P. Booth, "Pressure broadening of atomic oxygen two-photon absorption laser induced fluorescence," *Plasma Sources Sci. Technol.* **25**, 06LT03 (2016).
- [170] M. Tomoyuki, N. Kari, G. Timo, O. C. Deborah, and G. G. William, "Chemical kinetics and reactive species in atmospheric pressure helium–oxygen plasmas with humid-air impurities," *Plasma Sources Sci. Technol.* **22**, 015003 (2013).
- [171] B. McBride and S. Gordon, "Computer program for calculation of complex chemical equilibrium compositions and applications," NASA reference publication 1311 (1996).
- [172] F. Ossler, J. Larsson, and M. Aldén, "Measurements of the effective lifetime of O atoms in atmospheric premixed flames," *Chem. Phys. Lett.* **250**, 287-292 (1996).
- [173] G. Knopp, P. Radi, M. Tulej, T. Gerber, and P. Beaud, "Collision induced rotational energy transfer probed by time-resolved coherent anti-Stokes Raman scattering," *J. Chem. Phys.* **118**, 8223-8233 (2003).
- [174] P. J. Wrzesinski, H. U. Stauffer, J. B. Schmidt, S. Roy, and J. R. Gord, "Single-shot thermometry and OH detection via femtosecond fully resonant electronically enhanced CARS (FREE-CARS)," *Opt. Lett.* **41**, 2021-2024 (2016).

- [175] T. R. Meyer, S. Roy, T. N. Anderson, J. D. Miller, V. R. Katta, R. P. Lucht, and J. R. Gord, "Measurements of OH mole fraction and temperature up to 20 kHz by using a diode-laser-based UV absorption sensor," *Appl. Opt.* **44**, 6729-6740 (2005).
- [176] S. V. Chekalin and V. P. Kandidov, "From self-focusing light beams to femtosecond laser pulse filamentation," *Phys.-Uspekhi* **56**, 123 (2013).
- [177] W. Koechner, *Solid-state laser engineering* (Springer, 2013), Vol. 1.
- [178] J. Soures, S. Kumpan, and J. Hoose, "High power Nd:glass laser for fusion applications," *Appl. Opt.* **13**, 2081-2094 (1974).
- [179] J. Hunt, K. Manes, and P. Renard, "Hot images from obscurations," *Appl. Opt.* **32**, 5973-5982 (1993).
- [180] M. N. Slipchenko, B. D. Prince, S. C. Ducatman, and H. U. Stauffer, "Development of a Simultaneously Frequency- and Time-Resolved Raman-Induced Kerr Effect Probe," *J. Phys. Chem. A* **113**, 135-140 (2009).
- [181] S. P. Kearney, "Bandwidth optimization of femtosecond pure-rotational coherent anti-Stokes Raman scattering by pump/Stokes spectral focusing," *Appl. Opt.* **53**, 6579-6585 (2014).
- [182] R. Palmer, "The carsft computer code calculating coherent anti-stokes raman spectra: User and programmer information," (Sandia National Labs., Livermore, CA (USA), 1989).
- [183] K. Huber, G. Herzberg, P. Linstrom, and W. Mallard, *NIST Chemistry WebBook, NIST Standard Reference Database Number 69 Constants of Diatomic Molecules* (2012).
- [184] A. Bohlin and P.-E. Bengtsson, "Rotational CARS thermometry in diffusion flames: On the influence of nitrogen spectral line-broadening by CH₄ and H₂," *Proc. Combust. Inst.* **33**, 823-830 (2011).
- [185] R. L. Farrow, R. Trebino, and R. E. Palmer, "High-resolution CARS measurements of temperature profiles and pressure in a tungsten lamp," *Appl. Opt.* **26**, 331-335 (1987).
- [186] T. Dreier, G. Schiff, and A. Suvernev, "Collisional effects in Q branch coherent anti-Stokes Raman spectra of N₂ and O₂ at high pressure and high temperature," *J. Chem. Phys.* **100**, 6275-6289 (1994).

PUBLICATIONS

- [1] **K. A. Rahman**, V. Athmanathan, M. N. Slipchenko, T. R. Meyer, and S. Roy, "Pressure-scaling characteristics of femtosecond two-photon laser-induced fluorescence of carbon monoxide," *Appl. Opt.* 58, 7458-7465 (2019).
- [2] A. Sharma, M. N. Slipchenko, **K. A. Rahman**, M. N. Shneider, and A. Shashurin, "Direct measurement of electron numbers created at near-infrared laser-induced ionization of various gases," *J. Appl. Phys.* 125, 193301 (2019).
- [3] **K. A. Rahman**, V. Athmanathan, M. N. Slipchenko, S. Roy, J. R. Gord, Z. Zhang, and T. R. Meyer, "Quantitative femtosecond, two-photon laser-induced fluorescence of atomic oxygen in high-pressure flames," *Appl. Opt.* 58, 1984-1990 (2019).
- [4] M. E. Smyser, **K. A. Rahman**, M. N. Slipchenko, S. Roy, and T. R. Meyer, "Compact burst-mode Nd:YAG laser for kHz-MHz bandwidth velocity and species measurements," *Opt. Lett.* 43, 735-738 (2018).
- [5] H. U. Stauffer, **K. A. Rahman**, M. N. Slipchenko, S. Roy, J. R. Gord, and T. R. Meyer, "Interference-free hybrid fs/ps vibrational CARS thermometry in high-pressure flames," *Opt. Lett.* 43, 4911-4914 (2018).
- [6] **K. A. Rahman**, K. S. Patel, M. N. Slipchenko, T. R. Meyer, Z. Zhang, Y. Wu, J. R. Gord, and S. Roy, "Femtosecond, two-photon, laser-induced fluorescence (TP-LIF) measurement of CO in high-pressure flames," *Appl. Opt.* 57, 5666-5671 (2018).
- [7] A. Sharma, M. N. Slipchenko, M. N. Shneider, X. Wang, **K. A. Rahman**, and A. Shashurin, "Counting the electrons in a multiphoton ionization by elastic scattering of microwaves," *Sci. Rep.* 8, 2874 (2018).
- [8] **K. A. Rahman**, E. L. Braun, M. N. Slipchenko, Suresh Roy, and T. R. Meyer, "Flexible chirp-free probe pulse amplification for kHz fs-ps rotational coherent anti-stokes Raman scattering," (*Manuscript accepted with minor revisions*).
- [9] A. Sharma, **K. A. Rahman**, M. N. Slipchenko, A. Shashurin, and M. N. Shneider, "Absolutely Calibrated REMPI for diagnostics of carbon monoxide in high-pressure," (*Manuscript in preparation*).
- [10] D. K. Lauriola, **K. A. Rahman**, H. U. Stauffer, M. N. Slipchenko, T. R. Meyer, and S. Roy, "Detection of Formaldehyde as a minor species using electronic resonance enhanced coherent anti-Stokes Raman spectroscopy," (*Manuscript in preparation*).